BIOMATERIAL SCAFFOLDS AS A PLATFORM FOR FOCAL THERAPY AGAINST DISSEMINATED CANCER CELLS

A DISSERTATION
SUBMITTED TO THE FACULTY OF THE
UNIVERSITY OF MINNESOTA
BY

FRANCISCO PELAEZ

IN PARTIAL FULFILLMENT OF THE REQUIREMENTS
FOR THE DEGREE OF
DOCTOR OF PHILOSOPHY

ADVISOR
SAMIRA M. AZARIN

AUGUST 2018

Acknowledgements

Immense gratitude and thanks to my Ph.D. advisor, Dr. Samira M. Azarin, for her leadership, kindness, and steady motivation throughout my time as her student. I came into the group eager to learn and she fostered the opportunity for me to pursue exciting and challenging projects that led to interesting findings that I was proud to share with others, allowing me to develop as a research scientist. Thank you Samira.

I want to thank Garrett, Brett, Rachel, Maroof, and especially Carolyn for being wonderful role models at the beginning of my Ph.D. journey. Many thanks to the growing Azarin group, Jen, Hannah, Jenny, Pedram, Ray, Harish, Tiffany, Kristen, Paulina, and Quige for creating a fun, social, and respectable lab environment. Extra round of gratitude to Hannah, Tiffany, and Kristen for taking time out of lab for their comments and suggestions while putting together this thesis and to my friend Ryn for highlighting my best grammar mistakes. I also received wonderful guidance from my collaborators, Dr. Bischof and Dr. Shimizu, which from the very beginning helped shaped the trajectory of my studies. Innumerable thanks must also go to their lab members, Navid, Qi, Priyatanu, and Pegah (Bischof) and Brandon and Buck (Shimizu), for their generous and professional help. Additional thanks to Ben, Frankie, Lucy, Rachel, and Whitney for making the journey to WMBB more welcoming. Special thanks to the mice that contributed to my work that helped continue the advancement of improving human healthcare.

Thanks to Dr. Racila for your patience explaining basic histology with me and to Colleen for giving me the sharp tools in order to produce the histological samples. I also want to thank Bill for training me in the machine shop, which was surprisingly helpful at multiple times throughout my projects. A great big thank you to the CEMS department for their support, including Danny for handling so many of my orders and to Julie and Teresa for being the surrogate mothers to me and to all of the graduate students in the department, of whom I want to share appreciation to, including those before me for the strong sense of community both inside and outside of work. Particularly grateful to be part of the CEMS incoming class of 2012, who are on track to earn 50 Ph.D. degrees to further improve society around the world. Shout out to Brittany, Boo, Dayne, Koustav, Mark, Sadie, and Scott for the well-needed crazy times. Thank you to The University of Texas at Austin for their competitive chemical engineering B.S. program and particularly to Professor Baldea for persuading me to come to Minnesota, and you were right, the winters were not *that* bad.

Lifelong thank you to my family, both to the ones in the Dominican Republic and those that immigrated to the United States, for their unwavering and supernatural faith in me throughout this long journey. I am proud to have wonderful parents for laying out the path of support that ultimately allowed me to succeed and to my little sister for believing in me. Lastly, I want to thank my lovely wife Sarah for being my foundation of daily support and for showing me how beautiful life can be.

Dedicación

Para mis Abuelos, mis Abuelas, Papi, Mami, Hermana, y mis primos

Abstract

The primary cause of death for cancer patients stems not from the primary tumor, but from the spread of the disease to distal sites. Once the cancer has become detectable past the point of origin, tumor burden in vital organs is typically too high, limiting the efficacy of current treatment options. Development of novel therapies to target disseminated cancer cells prior to the onset of extensive metastatic burden could improve patient outcomes. Focal therapy, or energy-based ablation, has been successfully used to treat solid tumors, but has yet to be effectively applied toward disseminated cells. Microporous polymer scaffolds have previously been developed to capture metastatic breast cancer cells *in vivo*, and have been shown to reduce tumor burden in vital organs and improve survival. The purpose of this dissertation is to further improve the therapeutic potential of these biomaterials by destroying recruited cancer cells. Chapter 1 discusses in further detail how these scaffolds recruit metastatic cancer cells and how different types of focal therapy have been used to treat solid tumors in the clinic. To demonstrate that focal therapy could be used to kill cells within the scaffold, metal disks were integrated into polymer scaffolds to serve as a heat source through induction heating for focal hyperthermia. It was shown in Chapter 2 that these modified scaffolds could be applied successfully to kill infiltrating cells *in vivo*. The release of cancer-specific antigens following ablation of metastatic cells could be utilized to induce an anti-cancer systemic immune response. Utilizing melanocytes because of their well-defined tumorigenic antigens, collaborative work demonstrated that lysates generated from ablation via irreversible electroporation (IRE) resulted in the greatest amount of T cell activation *in vitro* in comparison to focal hyperthermia or cryogenic ablation. Thus, for potential future

combinatorial applications with immunotherapy, Chapter 3 investigated methods to introduce IRE to polymer scaffolds to treat disseminated cells. To accomplish this, metal mesh electrodes were integrated on either side of polymer scaffolds to create a near-uniform electric field distribution. These modified scaffolds were shown to be capable of complete ablation of infiltrating cells upon IRE *in vivo* in some mice, although further refinement is required to eliminate the variability in the response. The amount of antigen release from the treatment of recruited cells may be insufficient to induce a robust immune response following IRE treatment, and the local delivery of adjuvants may be required. Chapter 4 explored how polymer scaffolds could be coupled with inducible release of small molecules after electroporation. Scaffolds were modified to facilitate conjugation of inducible drug carriers and properties affecting IRE-mediated release were investigated to identify optimal conditions. In Chapter 5, polymer scaffolds were evaluated for recruitment of melanoma cells in both experimental and spontaneous metastasis models such that future studies of the application of combined focal and immunotherapy to disseminating tumor cells via biomaterial scaffolds could be performed in mouse models in which defined antigens could be used to track the efficacy of treatment. Finally, recommendations for future studies were discussed in Chapter 6. Altogether, the results of these studies represent an advance in the development of treatments that can target metastatic cancer, for which there are currently few effective therapeutic options.

Table of contents

List of tables..... ix

List of figures.....x

Chapter 1: Introduction..... 1

1.1 The ongoing battle against breast cancer 1

1.2 Mechanisms of metastasis.....3

1.3 *In vivo* models to study metastasis.....6

1.4 *In vivo* recruitment of cancer cells using biomaterials.....9

1.5 Focal therapies and immunotherapies.....14

1.6 Scope and organization of thesis 19

Chapter 2: Development of polymer-metal composite scaffolds for focal hyperthermia.....20

2.1 Introduction.....20

2.2 Materials and methods..... 21

2.3 Results and discussion..... 27

2.3.1 Characterizing heat generation from metal disks through electromagnetic induction.....27

2.3.2 Composite scaffold fabrication and biocompatibility.....29

2.3.3 *Ex vivo* radiofrequency treatment of tissue-laden scaffolds results in cellular destruction..... 35

2.3.4 Non-invasive, induced focal hyperthermia ablates tissue-laden composite scaffolds in vivo..... 37

2.4 Conclusions.....39

Chapter 3: Engineered polymer scaffolds with integrated electrodes for near-uniform electric field distribution during IRE treatment..... 41

3.1 Introduction..... 41

3.2 Materials and methods..... 42

3.3 Results and discussion..... 49

3.3.1 *In vivo* application of focal therapy to tissue-laden scaffolds..... 49

3.3.2 Determining IRE field parameters necessary to kill melanoma cells..... 52

3.3.3 Modeling electric field distribution with different electrode geometries..... 54

3.3.4 Fabricating IRE composite scaffolds..... 60

3.3.5 Use of PCL-IRE composite scaffolds to kill melanoma cells *in vitro*..... 62

3.3.6 Application of IRE to tissue-laden composite PCL-IRE scaffolds in vivo..... 63

3.4 Conclusions..... 64

Chapter 4: Utilizing liposomes for inducible release upon irreversible electroporation..... 66

4.1 Introduction..... 66

4.2 Materials and methods..... 67

4.3 Results and discussion..... 70

4.3.1 Chemical modification of polymer scaffolds for protein conjugation..... 70

4.3.2 Drug-loadable carriers for IRE-inducible release..... 75

4.4 Conclusions..... 82

Chapter 5: Integration of tumor cell-capturing polymer scaffolds into mouse models of melanoma..... 84

5.1 Introduction..... 84

5.2 Methods and materials..... 85

5.3 Results and discussion..... 90

5.3.1 Evaluation of PCL scaffolds in B16-F10 experimental metastasis model..... 90

5.3.2 Spontaneous metastasis model for recruitment of B16 cells to PCL scaffolds..... 94

5.3.3 Direct seeding of B16-F10 cells in polymer scaffolds prior to implantation..... 99

5.4 Conclusions..... 104

Chapter 6: Conclusions and future directions..... 105

6.1 General conclusions..... 105

6.2 Future directions..... 107

6.2.1 Sublethal hyperthermia for inducible release within PCL-IRE scaffolds..... 107

6.2.2 Investigating primary route of metastasis to PCL scaffolds..... 110

6.2.3 Downstream immune response following IRE of B16 cells in PLG scaffolds..... 111

Bibliography 112

List of tables

Table 2-1. Primer sequences for qRT-PCR analysis..... 26

Table 2-2. Skin depth of aluminum and copper at a frequency of 360 kHz..... 29

Table 2-3. Pathologist scoring of tissue-laden composite scaffolds..... 33

Table 5-1. Primer sequences for qRT-PCR analysis..... 88

List of figures

Figure 1-1. Five-year patient survival rates..... 2

Figure 1-2. Overview of the metastatic cascade..... 4

Figure 2-1. Metal disks show tunable heating response under alternating magnetic field..... 28

Figure 2-2. Stability of biocompatible PCL coating on Al disks.....30

Figure 2-3. Fabrication of PCL-Al composite scaffolds.....32

Figure 2-4. Histological analysis of implanted composite PCL-Al scaffolds..... 32

Figure 2-5. *In vivo* capture of metastatic cancer cells to composite scaffolds.....34

Figure 2-6. *Ex vivo* radiofrequency treatment ablates tissue-laden composite scaffolds.....36

Figure 2-7. *In vitro* ablation of 4T1 cancer cells by induction heating.....37

Figure 2-8. Induced focal hyperthermia ablates composite scaffolds *in vivo*.....39

Figure 3-1. *In vivo* focal therapy applied to tissue-laden scaffolds causes loss of cellular viability.....50

Figure 3-2. *In vivo* histological analysis of cell death in treated tissue-laden scaffolds..... 51

Figure 3-3. Characterizing IRE parameters necessary to ablate melanoma cells using parallel plate geometry *in vitro*..... 54

Figure 3-4. Analysis of resistivity of Matrigel-loaded and tissue-laden PCL scaffolds.... 56

Figure 3-5. Predicted electric field distribution from parallel plate, two-probe, and metal mesh electrode geometries..... 58

Figure 3-6. Evaluating spatial electric field distribution across different electrode geometries..... 60
Figure 3-7. Characterization of PCL-coated mesh..... 61
Figure 3-8. Histological analysis of implanted PCL-IRE scaffolds..... 62
Figure 3-9. *In vitro* B16 viability following treatment in PCL-IRE composite scaffolds.....63
Figure 3-10. IRE treatment of implanted PCL-IRE scaffolds *in vivo*.....64
Figure 4-1. Schematic for attaching drug-loaded particles onto microporous polymer scaffolds.....71
Figure 4-2. Aminolysis method to introduce primary amines to biodegradable polyesters.....73
Figure 4-3. Evaluation of surface primary amines on PCL scaffolds though fluorescamine treatment.....74
Figure 4-4. Schematic of biotinylated liposome preparation.....77
Figure 4-5. Liposome size distribution.....80
Figure 4-6. Inducible release from liposomes following electroporation.....81
Figure 5-1. Fluorescence signature of TFP-labeled B16-F10 cells..... 91
Figure 5-2. Flow cytometry to quantify number of B16-F10-TFP cells recruited to implanted PCL scaffolds.....92
Figure 5-3. Recruitment of B16-F10-TFP cells to PCL scaffolds following intravenous injection.....93
Figure 5-4. qRT-PCR assay to identify the presence of B16-F10 cells.....95

Figure 5-5. Detection of melanoma-specific gene expression in lungs from spontaneous metastasis model using qRT-PCR.....96

Figure 5-6. Evaluation of melanoma cell recruitment in a spontaneous orthotopic metastasis models.....98

Figure 5-7. H&E staining of B16-F10-Luc primary tumor.....100

Figure 5-8. Matrigel-only and B16-F10-Luc melanoma cell loaded polymer scaffolds post implantation *in vivo*.....101

Figure 5-9. Tracking growth of B16-F10-Luc cells in polymer scaffolds *in vivo*.....103

Chapter 1: Introduction

1.1 The ongoing battle against breast cancer

Breast cancer is a leading cause of death for women worldwide. In the U.S., 1 out of every 8 women will be diagnosed with breast cancer within her lifetime, with an estimated 250,000 new cases each year [1]. Treatment options for many types of cancer, including breast cancer, depend greatly on whether the disease is confined to the tissue of origin at the time of diagnosis, or if it has already invaded neighboring or distant tissues. If the cancer is confined to the breast, the preferred treatment is surgical resection of the tumor. To minimize recurrence from cancer cells that may have been left behind after surgical resection, many patients also receive local radiation and/or systemic therapies, such as chemotherapy. However, if the cancer has metastasized and is detected in distant organs or lymph nodes, surgical resection is no longer a feasible option for most patients. The most common treatment at this stage is the use of radiation and/or systemic therapies [1].

Metastasis has a drastic effect on long-term survival, not only for breast cancer, but for many other types as well (Fig. 1-1). About 90% of cancer mortalities occur when the cancer spreads to multiple organs, not from the primary tumor alone [2]. Once the cancer has spread, there is often a high tumor burden in vital organs like the brain and lungs, making the disease more difficult to treat. Additionally, there are drawbacks to conventional systemic therapies that limit their efficacy. Conventional systemic therapies for disseminated cancer fall under two main categories: chemotherapy and targeted therapy. Chemotherapeutic drugs are designed to kill rapidly dividing cells throughout

the body, such as the cancer cells contributing to a growing tumor. In some cases, however, the treatment becomes futile as either the growing cancer exhibits resistance to

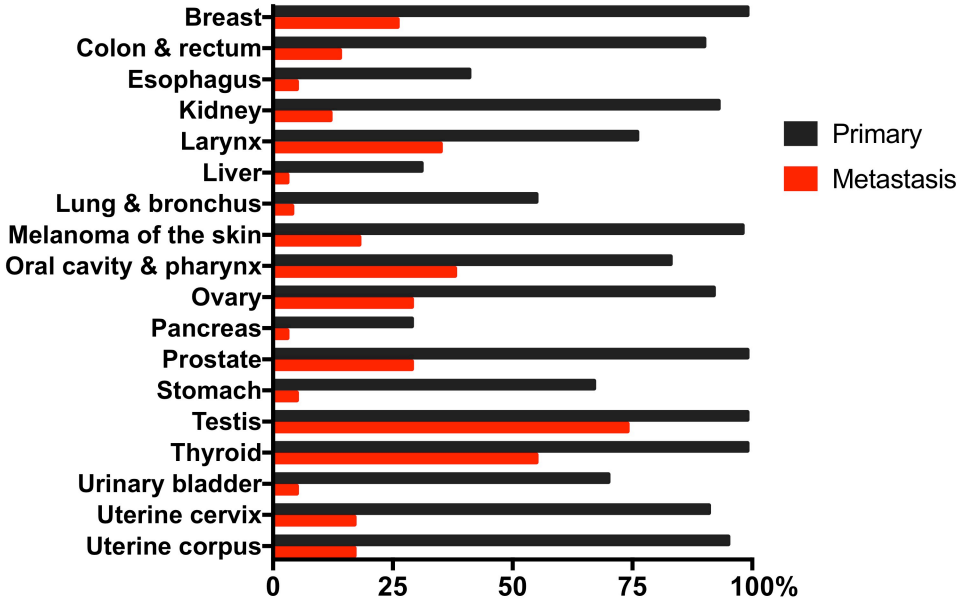

Figure 1-1. Five-year patient survival rates. Chart of five-year survival rates for a variety different types of cancer. Bars in black represent patients for whom the cancer has remained local, whereas bars in red are patients for whom the cancer has spread. Adapted from [3].

the drug, and/or the cancer cells spreading throughout the body are in a dormant, non-proliferating state and therefore not susceptible to chemotherapy. Targeted therapies target certain cell receptors specific to, or upregulated on, cancer cells in order to limit tumor growth and/or decrease the chance of recurrence. For example, in patients with hormone receptor (estrogen and/or progesterone) positive breast cancer, endogenous estrogen can promote tumor growth. Drugs such as Tamoxifen are effective at blocking estrogen receptors and limiting tumor growth and recurrence. Similar outcomes have been achieved for women with human epidermal growth factor receptor 2 (HER2) positive tumors using an antibody drug, Trastuzumab, which specifically targets HER2.

Unfortunately, breast tumors can be comprised of a heterogeneous population of cancer cells, with up to 21 distinct histological subtypes and at least four different molecular subtypes [1]. This biological diversity limits the potential of targeted therapies, as the treatment may only affect a certain subset of cancer cells throughout the body.

Due to these limitations in conventional therapies, patients diagnosed with advanced metastasis suffer from a high tumor burden in their vital organs, and are more likely to experience recurrence due to the presence of dormant and/or heterogeneous cancer cells. Thus, novel therapeutic strategies that target the metastatic cascade would allow for intervention at an earlier stage when the disease burden is still low.

1.2 Mechanisms of metastasis

An overview of the metastatic cascade is illustrated in Fig. 1-2. Metastasis starts when cancer cells from the primary tumor enter circulation through either the lymphatic system or the blood vessels by a process called intravasation. Tumor cells entering the lymphatic system first accumulate in the draining lymph node of the tumor; detection of such accumulation at the draining lymph node is routinely used as a prognostic tool for patient survival and for determining the best course of therapy [4]. The majority of tumor cells, however, enter the circulatory system through blood vessels, but both forms of entry are facilitated by expression of vascular endothelial growth factor (VEGF) [5]. Many of these circulating tumor cells (CTCs) do not survive [6], but a small fraction may persist for an extended period of time, as long as 22 years in some breast cancer patients [7].

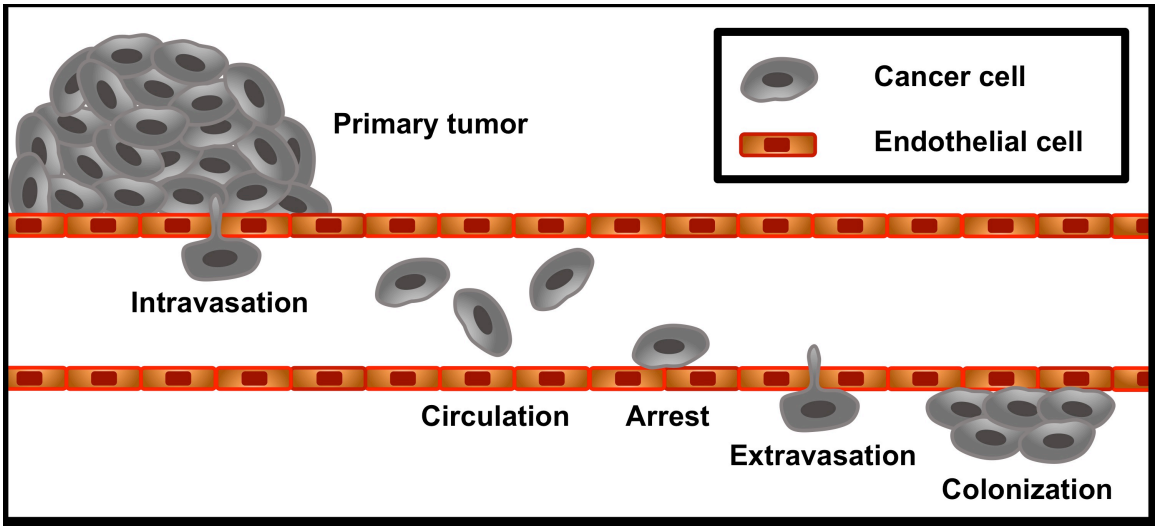

Figure 1-2. Overview of the metastatic cascade. Migrating cancer cells intravasate into adjacent blood vessels, upon which they can circulate throughout the body. These cells then reattach to the wall of the blood vessel and extravasate to colonize a new location.

Although CTCs are rare, and therefore difficult to isolate, a great deal of effort has been made to address this technological challenge. The ability to isolate CTCs from the blood of cancer patients could aid in early diagnosis, disease progression, and patient-specific cancer cell characterization. To date, many methods have been designed to enrich or sort for CTCs, such as flow cytometry [8], microfluidic devices [9], fiber optic array scanning [10], high-throughput optical-imaging systems [11], and immunomagnetic-bead purification [12]. One of these strategies, immunomagnetic-bead purification, has led to an FDA-approved CTC enumeration technology called CellSearch [13]. This technology could be used to predict the response to treatment and overall survival in breast cancer patients following treatment, as both progression-free and overall survival were significantly shorter for patients with high levels of CTCs versus patients with low CTCs levels [14]. While the isolation of CTCs has proven to be useful as a diagnostic tool, it cannot be used as direct treatment against cancer.

The mere presence of CTCs in the blood does not indicate that the cancer has successfully metastasized, as the downstream steps in the metastatic pathway are what lead to the fatality associated with metastasis. Upon intravasation, CTCs may arrest within the blood vessels, and then extravasate and colonize the tissue at a distant site from the primary tumor. At the early stages of colonization, the metastatic lesion is only composed of a few cells and is virtually undetectable. Currently, modern imaging technologies lack the resolution necessary to detect micrometastases (< 2 mm) [15]. These micrometastases may remain in a dormant state, undergo apoptosis, or proliferate to generate a secondary tumor [16]. Once the secondary tumor has grown large enough to detect, the tumor burden in that organ, and potentially others throughout the body, is typically high. In these cases, treatment is much more challenging.

The idea that CTCs do not randomly land at sites to colonize is a concept that was pioneered by Dr. Stephen Paget in 1889 with his seed-and-soil hypothesis. After studying the tumor distribution in patients who died of breast cancer, Paget recognized the propensity of certain organs to be “predisposed” for secondary tumors [17]. More recent findings have shown that the primary tumor plays a significant role in establishing conducive microenvironments, or pre-metastatic niches, prior to colonization. Systemic secretion of VEGF from the primary tumor facilitates trafficking of VEGF receptor 1-positive hematopoietic bone marrow progenitors to establish pre-metastatic niches by expressing proteinases, such as matrix metallopeptidase 9 (MMP9), to degrade basement

proteins to aid in extravasation and stromal derived factor 1 (SDF-1) to promote attachment, survival, and growth of disseminated cells [18].

The primary tumor also employs immune cells to facilitate recruitment and protection of disseminated cancer cells at the pre-metastatic niche. Elevated numbers of macrophage antigen 1-positive myeloid cells at the pre-metastatic niche correlate with increased metastasis, as these cells secrete tumor migration-stimulation factors, such as tumor necrosis factor α, macrophage inflammatory protein 2, and transforming growth factor β [19]. Another class of immune cells, $Gr1^{hi}CD11b^{+}$ myeloid derived suppressor cells (MDSCs), are seen at higher levels at the niche prior to tumor cell arrival, and help induce expression of MMP9 and SDF-1. In addition, $Gr1^{hi}CD11b^{+}$ MDSCs inhibit interferon (IFN) γ production, a cytokine associated with antitumor cytotoxicity, while also increasing expression interleukin (IL)-4, IL-5, IL-9, and IL-10, to stimulate immune suppressing T helper 2 (Th2) cells. The combination of decreased IFN γ and Th2 cytokines protects infiltrating tumor cells from immune surveillance [20].The existence of pre-metastatic niches orchestrated by the primary tumor suggests that artificial sites could be engineered to mimic these niches. An innovation of this nature could be used as a potential therapy to target metastatic disease and ultimately overcome the limitations of conventional therapies.

1.3 In vivo models to study metastasis

For studies focused on engineering biologically complex sites that mimic pre-metastatic, selection of the most appropriate animal model is critical. One of the most facile ways to

study tumor progression and metastasis is through the transplantation of tumor cells into the animal. Immunocompetent animal models have an intact immune system consisting of both a full innate and adaptive immune system. The innate immune system, which includes macrophages, neutrophils, and natural killer cells, is a first line of defense for detecting and eliminating commonly encountered pathogens, such as bacteria, viruses, fungi, and parasites. If an unrecognized pathogen overwhelms the innate immune system, the adaptive immune system is activated, which uses B and T cells to specifically recognize and destroy the foreign pathogen [21]. Conversely, immunocompromised models have genetic mutations to knock out T cell, or both T and B cell function, inhibiting their adaptive immune system. Immunocompetent models are used for syngeneic models, where the tumor and host tissue are of the same species. This is particularly advantageous in studying metastasis, since the interaction between the tumor and the host incorporates the entire immune system. Immunocompromised models, however, are useful in studying metastasis of human cancer through xenograft models, as the lack of adaptive immunity means that foreign cancer cells will not be rejected [22].

Furthermore, injected tumor cell models that result in either spontaneous or experimental metastasis have been employed to study metastasis to engineered materials. Spontaneous metastasis involves establishing a primary tumor at an orthotopic (in organ or tissue of origin) or ectopic (outside of origin) site and allowing it grow and spread. It is preferable to model metastasis from an orthotopic site, such as breast cancer inoculated into the mammary gland, because it more closely mimics the spread of cancer in a clinical setting;

however, only a few cancer lines are capable of metastasizing through this route. Common cancer lines for spontaneous metastasis upon orthotopic injection include human MDA-MB-231 and murine 4T1 breast cancer lines. The human MDA-MB-231 cell line is a hormone receptor negative (estrogen and progesterone) and HER2 negative cancer line isolated from metastatic cells found in excess fluid in the lungs of a patient with breast cancer [23]. The 4T1 line is isolated from a spontaneously arising murine mammary tumor [24]. Both the 4T1 and MDA-MB-231 lines metastasize from an orthotopic site to vital organs, such as the liver and lung, as observed clinically [24, 25].

Experimental metastasis circumvents the primary tumor growth process and intravasation and instead introduces cancer cells directly into circulation system through either an intraperitoneal, intravenous, or intracardiac injection. Since there is no primary tumor in this method, experimental metastasis models may not reflect the systemic inflammatory effects caused by the primary tumor, including those at the pre-metastatic niche. Experimental metastasis is still widely utilized because it requires a shorter time frame to detect metastasis. Additionally, the disease can be targeted to a specific site of interest with a larger variety of cancer lines [25]. A common cell line for experimental metastasis used in research is the murine B16-F10 cell line, isolated from spontaneous melanoma found on the ear [26]. This cell line reproducibly colonizes the lung following a tail vein injection. While this cell line has can also spontaneously metastasize to the lungs from an orthotopic injection, it does so much less efficiently than a more aggressive variant, B16-BL6 [27]. A better understanding of how artificial metastatic sites attract cancer cells can

be attained using both spontaneous and experimental models. Nevertheless, the shortcomings of each method lead to difficulties in understanding the complete picture of metastasis in a clinical setting.

1.4 In vivo recruitment of cancer cells using biomaterials

The first efforts to generate an engineered pre-metastatic niche using animal models focused on mimicking the skeletal microenvironment, due to the high propensity for many types of cancer, including breast cancer, to metastasize to the bone. To study human breast cancer metastasis to bone, researchers extracted bone cores from human femurs and implanted them subcutaneously in the flanks of immunocompromised mice. Histological analysis of harvested bone implants demonstrated their ability to recruit HER2 positive human breast cancer cells (SUM1315) [28]. Reproducibility, however, was an issue due to the inherent variability of bone implants from different patients.

Efforts then shifted to creating artificial sites that could mimic the skeletal microenvironment, which was first accomplished by seeding human bone marrow cells into porous scaffolds made from lyophilized silk fibroin coupled with bone morphogenetic protein-2. The artificial bone-mimicking materials were able to recruit human breast cancer cells in a similar manner as the human bone implants [29]. These materials have also been used to recruit MDA-MB-231 human breast cancer cells from an orthotopic inoculation in immunocompromised mouse models, as well as murine B16-F10 melanoma cells inoculated directly into the bloodstream using immune competent mice [30]. Other bone-mimicking scaffolds made from synthetic polymers have been

used to recruit disseminated cells. Polyacrylamide scaffolds seeded with human bone marrow cells have been shown to recruit the PC-3 human prostate cancer cells following an orthotopic inoculation [31]. Electrospun polycaprolactone (PCL) scaffolds loaded with bone morphogenetic protein-7 and seeded with human osteoblasts have been shown to capture human breast (MDA-MB-231) [32] and prostate (PC-3) cancer cells [33] after intracardiac injection. However, the need to mimic an organ-specific microenvironment, limits the potential of the artificial metastatic site because it attracts the population of cancer cells seeking that certain site. A system that uses a broader approach to recruiting metastatic cells could have a greater impact as a therapeutic tool.

In one example of a system that is not organ-specific, a network of human blood vessels was generated from a basement membrane-like matrix seeded with both human endothelial and mesenchymal cells. In immunocompromised mice, human breast cancer cells (MDA-MB-231) metastasized from the primary tumor and extravasated through this human blood vessel network [34]. Another system used polymer scaffolds to replicate the microenvironment found in the peritoneal cavity in patients with ovarian cancer. Unlike most other types of cancer that metastasize through the vascular system, ovarian cancer can spread to other organs throughout the peritoneum. As the primary tumor grows, cancer cells disseminate as single cells or multicellular spheroids from the tumor and metastasize in the ascites fluid throughout the peritoneal cavity [35]. To mimic this microenvironment, polymer scaffolds made out of PCL or polystyrene have been modified with exosomes isolated from human ascites fluid from ovarian cancer patients.

These exosomes have been shown to act as signaling vesicles, thus mediating homing of disseminated cancer cells.

The exosome-loaded scaffolds altered the metastatic profile of SKOV3 human ovarian cancer cells in the intraperitoneal cavity by attracting these cancer cells to the engineered scaffold implanted in mice. This method lowered the tumor burden of nearby key organs, such as the pancreas, and led to a 100-day improvement in survival. The therapeutic benefit of the scaffold was further enhanced by explanting it to remove recruited ovarian cancer cells, which resulted in 75% of the mice surviving past the endpoint of the study. This study showed that engineered scaffolds could be used as a therapeutic tool against cancer by capturing disseminated cells, resulting in lower tumor burden in vital organs and increasing overall survival [36].

Another approach has been to use acute inflammatory responses to recruit metastatic cancer cells. Inflammatory cells play important roles in tumor progression, including facilitating metastasis [37]. In one study, a solution of microparticles was injected into the dorsal subcutaneous space of immunocompetent mice. Murine melanoma (B16-F10) cells were then inoculated into the intraperitoneal cavity, and these cells were found to have quickly metastasized to the microparticle injection site. Regardless of the composition of microparticles used, which included polylactic acid, aluminum hydroxide, and glass, a positive correlation was observed between the number of melanoma cells recruited and the number of inflammatory cells at the injection area. This broader approach was also found to be efficacious in recruiting human breast (MDA-MB-231)

and prostate (PC-3) cancer, as well as murine lung cancer (Lewis lung carcinoma). Interestingly, there was also a positive correlation between the number of recruited melanoma cells and survival. This approach, however, only worked well under acute inflammatory conditions. The amount of recruited melanoma cells decreased sharply with the length of time the microparticles were implanted, severely limiting the system's therapeutic potential for any long-term use [38]. More importantly, this study only utilized an experimental metastasis model. Thus, the study does not reflect the clinical progression of metastasis, nor does it take into account the systemic inflammatory changes resulting from an established primary tumor.

Another approach by Azarin et al. utilized microporous polymer scaffolds to act as a pre-metastatic niche by emulating the immune cell populations found in metastatic organs [39]. Upon implantation in mice with orthotopic breast tumors, the immune cell populations found in the scaffolds were similar to those in the lung, a common site of breast cancer metastasis. Consequently, human MDA-MB-231BR (a highly metastatic variant of the MDA-MB-231 cell line [40]) and mouse 4T1 breast cancer cells metastasized to the scaffolds when they were implanted in the intraperitoneal cavity or the subcutaneous space, even when the scaffolds were not functionalized with cells, extracellular matrix proteins, or soluble factors prior to implantation. Recruitment was associated with an increase in the prevalence of $Gr1^{hi}CD11b^{+}$ MDSCs in the scaffolds. As such, increasing the number of $Gr1^{hi}CD11b^{+}$ cells, either by localized expression of CCL22 or by seeding these cells directly into the scaffold prior to implantation, resulted in increased recruitment of breast cancer cells to the scaffold [39]. The notion that

MDSCs are involved in recruitment is not surprising, given the various roles they play in promoting metastasis, as described above. Furthermore, depletion of this immune population through systemic delivery of an anti-Gr1 antibody increased the survival of mice with breast cancer [41]. Further studies evaluating the mechanism of MDSC-based recruitment to the scaffold identified that MDSCs secrete soluble factors that induce tumor cell migration, including haptoglobin, which interacts with the CCR2 receptor [42], a receptor that is upregulated in breast cancer cells and tissues [43]. Incorporation of recombinant haptoglobin into polymer scaffolds caused a significant increase in MDA-MB-231BR recruitment, demonstrating a potential mechanism through which $Gr1^{hi}CD11b^{+}$ cells may mediate metastasis to the scaffold [42]. This scaffold technology could have broad therapeutic applicability since the recruitment of tumor cells is mediated by the local metastatic immune environment, which is not organ-specific, and immune cells have been shown to regulate metastasis in multiple types of cancer [19, 44-50].

Further demonstrating the robustness of the approach, the presence of scaffolds composed of either PCL or poly(lactide-*co*-glycolide) (PLG) also decreased the tumor burden in vital organs such as the lung, liver, and brain, in both human and murine breast cancer models [39, 41]. The decrease in metastatic tumor burden led to an increase in survival in a more clinically relevant primary tumor resection model, which was designed to evaluate the long-term survival from disseminated cancer cells. Approximately 40% of mice with scaffolds survived until the end point of the study (200 days), whereas none of the mice without scaffolds survived past 40 days [41]. In addition to the therapeutic

potential of the system, cancer cells can be detected in the scaffold prior to detection in typical metastatic sites, such as the lung, liver, and brain [39, 41].

While the polymeric scaffolds alone did show some therapeutic benefit, a growing body of research has demonstrated that disseminated tumor cells are not bound to remain in one location. Both reseeding of the primary tumor site [51] and direct spreading from one metastatic site to another [52] have been observed. This observation suggests that the recruitment of cancer cells to an artificial site might only delay the eventual reseeding of vital organs. Thus, developing strategies to kill these recruited cells could potentially increase the therapeutic potential of polymeric tumor-capturing scaffolds. In addition, since these scaffolds capture metastatic cells early in disease progression, they offer the potential to treat metastasis before the disease burden is too high. **The goal of this thesis is to modify polymeric tumor-capturing scaffolds so they can be combined with focal ablation therapies in order to develop novel treatments for metastatic disease that will be applicable across multiple types of cancer.**

1.5 Focal therapies and immunotherapies

As mentioned previously, a common strategy for killing tumor cells is the use of chemotherapeutic drugs. These drugs have been utilized in polymeric scaffolds as a method of drug delivery, a concept that has been studied in great detail [53]. The long release timescales of chemotherapeutic drugs required to kill recruited cancer cells, however, would not be practical in a polymeric scaffold designed to capture disseminated cancer cells. Additionally, the development of chemoresistance would remain a challenge

[54]. Focal therapies, such as thermal ablation [55], cryoablation [56], and irreversible electroporation (IRE) [57], have been successfully used to treat cancer by killing cells locally at the primary tumor site. These focal therapies have proved to be particularly effective for non-resectable tumors. By treating locally, focal therapy avoids some of the drawbacks of chemotherapy, which as a systemic approach, leads to toxic side effects in healthy tissue. Focal therapy has thus far only been successfully used against solid tumors, but the ability to capture disseminated cancer cells could allow for the use of focal therapy to target metastasis as well.

Thermal ablation, also known as focal hyperthermia, has been used to treat cancerous tissues throughout human history, with written records going as far back as the Egyptian times in 3000 BC [58]. More recently, thermal ablation has been used clinically for bone, liver, breast, kidney, lung, and prostate cancer [59-61]. Focal hyperthermia uses prolonged exposure to elevated temperatures, 42 - 46 °C, to denature intracellular proteins, resulting in an exponential decrease in cell survival with thermal exposure [62]. However, this temperature range requires treatment for many hours, which can lead to the acquisition of thermotolerance [63]. Recently, localized heating to over 50 °C for minutes or even seconds has been shown to effectively kill cells while mitigating the risk of thermotolerance [64, 65]. Traditional focal hyperthermia techniques have used invasive thermal probes to target solid tumors, but less invasive methods have recently been developed through electromagnetic induction of thermal seeds using an oscillating magnetic field within a radiofrequency coil [66, 67].

Cryoablation works instead by using freezing temperatures to kill cells. Iced saline solutions were first used as an anesthetic for patients with advanced breast and uterine cancer, but detrimental effects of cold temperatures on cancer cell viability were first noted in the 1840s. With advancements in technology, modern cryoablation utilizes hollow probes and adiabatic cooling to reach temperatures as low as –190 ºC [68]. These cryogenic temperatures cause an iceball to form, subjecting the tumorous tissue to lethally cold temperatures of –20 ºC to –40 ºC. At these temperatures, freezing the extracellular space causes an increase in extracellular solute concentration. This increase then leads to cellular dehydration and eventual ice formation within the cell, which can cause damage to the organelles and cell membrane. Further cellular damage occurs upon thaw. The intracellular space becomes hypertonic, causing a strong influx of water into the cell, and leading it to burst [55]. This powerful tool has been used clinically for kidney, liver, prostate, breast, and musculoskeletal cancer [69].

IRE is an emerging soft tissue ablation technology that was first commercialized in 2009. This technique uses the principles of electroporation, which is the use of electric fields delivered in periodic pulses to induce pores in the cell membrane and significantly increase transmembrane permeability [70]. At modest field strengths and pulse durations, the opening of the cell membrane is reversible, having little to no effect on cellular viability [71]. Reversible electroporation is now a common technique that has been applied to deliver nonpermeable molecules into cells, such as DNA for gene delivery [72]. However, at strong enough electric field strengths, the pore formation is irreversible and leads to a loss in cellular viability [57]. Although a relatively new treatment method,

IRE has shown effectiveness for patients with liver, kidney, pancreas, and prostate cancer [73].

Although focal therapy has been shown to be an effective alternative to surgical resection, intervention may fail to treat the entire tumor and/or the cancer cells may have already metastasized elsewhere, which may lead to recurrence. To improve the efficacy of focal therapy, combinatorial strategies involving systemic immunotherapy have been investigated. Due to the mutations associated with cancer, immunotherapy employs the host's immune system to target tumor-specific antigens to recognize and attack cancer cells throughout the body [74]. Achieving anti-cancer immunity remains a grand challenge, but several novel strategies have garnered clinical relevance over the past 30 years. To stimulate natural killer cell induction, early strategies administered high doses of cytokine IL-2 [75], which received FDA approval for patients with metastatic kidney and melanoma in 1992 and 1998, respectively [76]. Recent approaches have utilized immune checkpoint blockade inhibitors, such as antibody drugs against CTLA-4 and PD-1, to target cancer by blocking inhibitory pathways naturally found in the immune system. Three immune checkpoint blockade inhibitors have been approved by the FDA within the past decade for a variety of advanced cancer types: melanoma, lung, kidney, bladder, lymphoma, and gastric cancer [77]. Most recently, the FDA approved the use of an adoptive cell therapy that utilizes chimeric antigen receptor (CAR) T cells to treat leukemia. CAR T cell therapy involves genetically engineering a patient's endogenous T cells to eliminate malignant cells by inducing expression of a T cell receptor specific for a desired surface antigen [78]. Despite the immense progress made in immunotherapy

strategies towards treating disseminated cancer, the drawbacks from current immunotherapy options, mainly immune checkpoint blockade inhibitors and CAR T cell therapy, limit their efficacy. Immune checkpoint inhibitors exhibit low response rates, with 1 in 2 melanoma patients resisting treatment and enduring disease progression [79]. The long and expensive wait times required to harvest and genetically engineer a patient's T cells for CAR T cell therapy also restricts its widespread application [80]. In addition, neither option has been successful in treating solid tumors, which have strong immunotolerance capabilities.

Combinatorial strategies involving focal and immunotherapy options have shown promise at treating solid tumors while also killing disseminated cells. In one study, immunocompetent mice with melanoma tumors were treated with either thermal or cryoablation with or without immune checkpoint inhibitors. Following treatment, the mice were given a secondary tumor challenge. Regardless of focal therapy, mice that received immune checkpoint inhibitors exhibited enhanced overall survival compared those that received focal therapy alone. Interestingly, some mice that received only focal therapy developed tumor immunity without the need for immune checkpoint inhibitors, and had greater overall survival under cryoablation versus thermal ablation [81]. Thus, ablation of cancer cells from a primary tumor releases tumor-specific antigens that can serve as a vaccine against cancer, and the effectiveness of the vaccine can be dependent on the focal therapy conditions. The use of tumor lysates as a vaccine has also been demonstrated with microporous polymer scaffolds. Scaffolds loaded with tumor lysate from *ex vivo* cryoablation of murine melanoma tumors were implanted subcutaneously in

the left flank. Mice with growing melanoma tumors that received these loaded scaffolds experienced a decrease in tumor growth and an improvement in overall survival [82]. As a consequence, lysing tumor cells within the patient could lead to anti-tumor immunity, which may be possible even if the cancer is disseminated with no primary tumor present. While many advances have been made in the clinical use of focal therapies, they have yet to be used to target disseminated cancer cells. The ability to target disseminated cancer cells could lead to earlier intervention and possible immunity for patients with metastatic disease.

1.6 Scope and organization of thesis

The scope of this thesis is to improve the therapeutic potential of tumor cell-recruiting polymer scaffolds by integrating focal therapy strategies to kill recruited tumor cells *in vivo* in a manner that can promote an immune response against remaining tumor cells throughout the body. Chapters 2 and 3 will focus on modifying the PCL scaffold to kill cells through focal hyperthermia and IRE, respectively. In Chapter 4, drug carriers will be incorporated into PCL scaffolds for controlled release upon focal therapy in order to modulate the local environment for enhanced anti-tumor immune reaction. In Chapter 5, PCL scaffolds will be analyzed for the ability to recruit melanoma cells to study potential immunotherapy strategies, as unlike breast cancer cells, melanoma cells have defined antigens that can be tracked for proof-of-principle immunotherapy studies. Future directions that warrant exploration will be discussed in Chapter 6.

Chapter 2: Development of polymer-metal composite scaffolds for focal hyperthermia

2.1 Introduction

As discussed in section 1.5, applying a focal ablation therapy such as hyperthermia with biomaterial scaffolds that recruit metastatic cells could provide novel options for treating disseminating cancer. Biomaterial scaffolds have been modified for focal hyperthermia for various applications [83-86]. Focal hyperthermia initiated by near-infrared light has been shown in polydopamine-coated 3D-printed bioceramic scaffolds [83] and gold nanoparticle-containing gelatin biomaterials [84]. PCL scaffolds have also shown potential for hyperthermia with embedded magnetic nanoparticles for induced heating in oscillating magnetic fields [85, 86]. However, none of these biomaterials have been shown to recruit metastatic cancer cells.

Rapid heating through an oscillating magnetic field can be achieved by inducing large eddy currents in a conducting material [87]. Thus, we hypothesized that incorporation of metal disks into microporous polymeric scaffolds that have previously been shown to

capture metastasizing cells *in vivo* would enable non-invasive application of focal hyperthermia to infiltrating cells. The work described in this chapter sought to characterize the heat generation and tissue ablation of these polymer-metal composite scaffolds.

2.2 Materials and methods

Metal disk fabrication and coating

Metal disks were made using four different-sized custom punches on a 0.1 mm thick Puratronic aluminum foil (Alfa Aesar) or 0.1 mm thick Puratronic copper foil (Alfa Aesar) to generate disks with varying diameter. Following fabrication, disk size was measured by image analysis using ImageJ. To coat metal disks with a polymer film, 1.70 mm Al disks were dipped once into a 10% (w/w) solution of PCL (DURECT; inherent viscosity = 0.65-0.85 $dL \cdot g^{-1}$) in dichloromethane (Sigma). Coated disks were dried overnight. To characterize the polymer coating thickness, partial removal of the coating was performed using a razor blade, and step height across the interface of the coated and uncoated regions was measured using a Tencor P10 profilometer.

Composite scaffold fabrication

To fabricate composite scaffolds, PCL microspheres were first prepared as previously described [41]. Briefly, a 6% (w/w) solution of PCL (DURECT; inherent viscosity = 0.65-0.85 $dL \cdot g^{-1}$) in dichloromethane was emulsified in a 10% (w/w) poly(vinyl alcohol) solution and homogenized at 10,000 rpm for 1 minute. Microspheres were lyophilized for 48 hours. PCL microspheres and sieved sodium chloride particles (250-425 μm) were

mixed in a 1:30 (w/w) ratio. PCL-coated metal disks were layered between two PCL microsphere/sodium chloride mixtures in a 5 mm steel die (Specac), and the contents were pressed to 3,300 lbs. for 45 seconds. The pressed disks were heated at 60 ºC for 5 minutes on each side followed by foaming at 800 psig for ~24 hours, after which the gas was released at 17.5 CFH. Salt particles were removed by immersing disks in water for 90 minutes on a rocking platform. Composite scaffolds were sterilized by soaking in 70% ethanol, followed by rinsing with sterile water and drying on a sterile gauze pad. Scaffolds were then stored at -80 ºC until further use.

Scaffold implantation

Animal studies were performed in accordance with institutional guidelines and protocols approved by the University of Minnesota Institutional Animal Care and Use Committee (IACUC). BALB/c mice were purchased from The Jackson Laboratory, and mice were 8-31 weeks of age at the time of surgery. Two scaffolds were implanted into the subcutaneous space of the upper dorsal region per mouse. Experiments on tissue-laden scaffolds were performed 3-10 weeks following implantation.

Tissue sectioning and histological analysis

Tissue-laden scaffolds for histology were removed whole from the subcutaneous space at 3-4 weeks post-implantation. The tissues were fixed in 10% buffered formalin, embedded in paraffin, and sectioned at 4 μm using an HM 315 microtome (Microm). Slides were stained with hematoxylin and eosin (H&E) for histological analysis. Slides were imaged using an EVOS FL Auto Microscope (Thermo Fisher Scientific).

Inductive heating studies

A 1 kW inductive heating system with a 2.75 turn, water-cooled, 1.75 cm inner diameter, copper coil (Ameritherm Inc.) was used to generate an alternating magnetic field for inductive heating experiments. The coil current was adjusted to achieve different magnetic field strengths as previously described [67]. Briefly, COMSOL version 5.2a (COMSOL, Inc.) was used to calculate the volume-averaged value of the field strength across the sample. The resonant frequency used for all studies was 360 kHz. For heating studies with bare metal disks, the disks were placed at the bottom of a 2 mL microcentrifuge tube with 1 mL of distilled water. A type T thermocouple (OMEGA Engineering), model 5TC-TT-T-40-36, was placed on the metal disk to measure the surface temperature. This assembly was placed in the center of the copper coil and an oscillating magnetic field was applied for 15 minutes. For *in vitro* heating studies of 4T1 breast cancer cells (ATCC CRL-2539), one million 4T1 cells were encapsulated in 30 μL of 5 $mg \cdot mL^{-1}$ Matrigel (Corning) surrounding a 1.70 mm Al disk. Samples to be treated were placed in the induction coil set to 15 $kA \cdot m^{-1}$ at 360 kHz for 10 min. For experimental temperature profiles to measure temperature elevation near the edge, composite scaffolds were placed in a 1.5 mL microcentrifuge tube with 1 mL of ultrasound gel. A type T thermocouple was placed 1.85 mm (close to the far edge of the scaffold) from the center of the scaffold to record the temperature rise within the tissue-laden composite scaffold, which was treated for 4 minutes at 15 $kA \cdot m^{-1}$. For *ex vivo* tissue-laden scaffold heating studies, harvested scaffolds were used for measuring temperature profiles and cell viability. For *ex vivo* viability studies, tissue-laden scaffolds

were placed in 1 mL of phosphate-buffered saline (PBS) and treated for 10 minutes at 15 $kA \cdot m^{-1}$. To account for the self-heating of the thermocouple in the oscillating magnetic field, the average dynamic temperature rise of thermocouple-only samples at each respective magnetic field strength, were subtracted from dynamic temperature rise profiles.

For *in vivo* tissue-laden scaffold heating studies, due to size limitations of the animal body and coil dimensions, the implanted PCL-Al scaffold could not be placed in the center of the radiofrequency coil. To ensure a field strength of 15 $kA \cdot m^{-1}$ at the scaffold location, the center of the radiofrequency coil was set to 20 $kA \cdot m^{-1}$ and placed 9.25 mm above the implant site. FLIR E30 and FLIR A300 IR-cameras (FLIR Systems Inc.) were used to capture infrared (IR) images before and during 10-minute treatment. An *in vivo* heating profile was generated by analyzing the average temperature values in a ~5 mm diameter circular region encompassing the implanted scaffold in the IR video during treatment using ThermaCAM Researcher Professional 2.10 software (FLIR Systems Inc.). To evaluate the acute effect of treatment, scaffolds were harvested immediately after treatment to assess cellular viability. For chronic effects of thermal injury, mice were allowed to recover for three days, after which scaffolds were harvested and placed in formalin for histological analysis. Day three was chosen for this analysis in accordance with previous literature demonstrating that chronic effects of thermal therapy can be detected as early as three days after treatment [88, 89].

Viability assay

The viability of cells in tissue-laden scaffolds was determined by treating the cells with cell viability reagent WST-1 (Takara Bio). Scaffolds were transferred to 500 μL of fresh media (DMEM containing 10% fetal bovine serum, 1% L-glutamine, and 1% penicillin-streptomycin; Thermo Fisher Scientific). Microscissors were used to mince the scaffolds into small pieces. 50 μL of WST-1 reagent was added to each sample and incubated at 37 ºC for 2 hours. Media samples were used as a negative control for background measurement, and 70% ethanol treatment of tissue-laden scaffolds was performed as a control for total cell death. For ethanol treatment, tissue-laden scaffolds were minced in 500 μL of 70% ethanol and incubated on ice for 1 hour. Following ethanol incubation, the samples were centrifuged at 14,000 x *g* for 5 minutes, and the supernatant was replaced with 500 μL of fresh media prior to addition of the WST-1 reagent. After WST-1 treatment, all samples were vortexed and centrifuged at 14,000 x *g* for 5 minutes. 400 μL of sample was filtered through a 70 μm filter. Triplicates of 100 μL per sample were transferred to a 96-well plate. The absorbance of each well was measured at a wavelength of 440 nm with a Synergy H1 microplate reader (BioTek Instruments).

qRT-PCR analysis of tissue-laden scaffolds from tumor-bearing mice

Female 15-week-old BALB/c mice were inoculated with two million 4T1 breast cancer cells (ATCC CRL-2539) in a volume of 50 μL PBS in the number four right mammary fat pad. For tumor-free controls, mice received an injection of 50 μL PBS. One week post-inoculation, two scaffolds of the same type (PCL or PCL-Al) were implanted in the subcutaneous space. Tumors and scaffolds were harvested four weeks post-inoculation

and immediately snap frozen in liquid nitrogen and stored at -80 ºC for further RNA extraction. For RNA extraction, samples were placed in RLT buffer (Qiagen) with 1% β-mercaptoethanol (Sigma-Aldrich) and homogenized at 10,000 rpm for 20 seconds on ice. To minimize the risk of cross-contamination between samples, after homogenization of each sample the homogenizer was washed with 3 rounds of Type 1 water, 2 rounds of 70% ethanol, and 2 rounds of 100% ethanol, followed by a wash with ELIMINase (Thermo Fisher Scientific) and then 4 rounds of Type 1 water washes before running the next sample. Total RNA extraction was then performed using the RNeasy Mini Kit (Qiagen) following the manufacturer's instructions. cDNA synthesis was performed with 1 μg of total RNA for each sample using the Omniscript RT Kit (Qiagen), and qRT-PCR reactions were performed with 1 μL of cDNA, iTaq Universal SYBR Green Supermix (BioRad), and the gene-specific forward primer (250 nM) and reverse primer (250 nM). The qRT-PCR was performed using a CFX Connect Real-Time PCR Detection System (BioRad). Primers for *GAPDH* were obtained from the literature [90] and the remaining were obtained from PrimerBank (https://pga.mgh.harvard.edu/primerbank/). The primers used in these studies are summarized in Table 2-1.

Table 2-1. Primer sequences used for qRT-PCR analysis.

Gene	**Forward (5'-3')**	**Reverse (5'-3')**
GAPDH	CAATGTGTCCGTCGTGGA	GATGCCTGCTTCACCACC
FTH1	CAAGTGCGCCAGAACTACCA	GCCACATCATCTCGGTCAAAA
SPP1	AGCAAGAAACTCTTCCAAGCAA	GTGAGATTCGTCAGATTCATCCG
LYZ2	ATGGAATGGCTGGCTACTATGG	ACCAGTATCGGCTATTGATCTGA
PABPC1	CAAGCCAGTACGCATCATGTG	TGCTTCCTGTGTTTCAAAGTGT
EPCAM	GCGGCTCAGAGAGACTGTG	CCAAGCATTTAGACGCCAGTTT
LCN2	TGGCCCTGAGTGTCATGTG	CTCTTGTAGCTCATAGATGGTGC
APOE	CTGACAGGATGCCTAGCCG	CGCAGGTAATCCCAGAAGC
MT2	GCCTGCAAATGCAAACAATGC	AGCTGCACTTGTCGGAAGC

Statistical analysis

Data are presented as the mean ± standard deviation (SD), and p-values were determined using an unpaired Student's t-test. For qRT-PCR studies, p-values were determined using a two-way analysis of variance (ANOVA) with a Tukey post hoc test.

2.3 Results and discussion

2.3.1 Characterizing heat generation from metal disks through electromagnetic induction

Aluminum was chosen as the conducting material for the thermal seed as its low density and high malleability made it a versatile material for proof of principle studies. To evaluate the ability of 100 μm-thick aluminum disks to heat in response to the presence of an oscillating magnetic field, aluminum disks of various diameters (Fig. 2-1A) were submerged in water and placed in a radiofrequency coil, and an oscillating magnetic field at 15 $kA \cdot m^{-1}$ at 360 kHz was applied. As the disk diameter increased from 1.13 ± 0.05 mm to 1.90 ± 0.04 mm, the temperature elevation achieved from the surface of the disk increased from 19 ± 2 ºC to 58 ± 4 ºC, indicating a positive correlation between disk diameter and temperature elevation (Fig. 2-1B). With the disk diameter fixed at 1.70 ± 0.04 mm, the temperature elevation could also be modulated at a fixed frequency of 360 kHz by increasing the magnetic field strength, resulting in temperature elevations from 5 ± 1 ºC at 5 $kA \cdot m^{-1}$ to 56 ± 4 ºC at 20 $kA \cdot m^{-1}$ (Fig. 2-1C). The type of metal used also affected its response to the magnetic field, with 1.68 ± 0.07 mm diameter copper disks generating a temperature elevation of 43 ± 3 ºC, in comparison to 47 ± 3 ºC for 1.70 ± 0.04 mm diameter aluminum disks (Fig. 2-1D). These results are consistent with previous

work by Stauffer et al. [87] that shows power absorption of a conducting disk is based on radius, conductivity, and magnetic field strength.

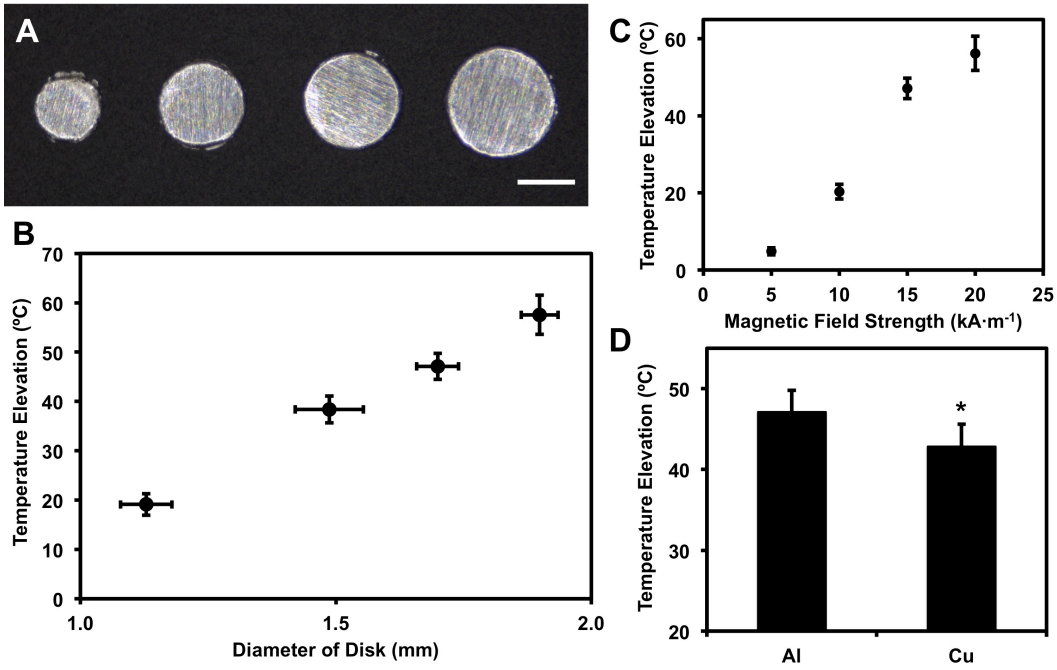

Figure 2-1. Metal disks show tunable heating response under alternating magnetic field. (A) 100 μm thick, Al disks of varying diameters from left to right: 1.13 mm, 1.49 mm, 1.70 mm, and 1.90 mm. Scale bar indicates 1 mm. (B-D) Temperature elevation of metal disks following 15 minute exposure to magnetic field at 360 kHz for Al disks of varying sizes at 15 kA·m^{-1} (B), for 1.7 mm Al disks at increasing magnetic field strengths (C), and for 1.7 mm disks with different metal composition at 15 kA·m^{-1} (D). (*) $P < 0.01$ compared to Al. Temperature data is mean ± SD, n = 8; disk diameter data is mean ± SD, n = 10.

Heat generation is also directly related to skin depth (μm), δ, of the thermal seed [87]:

$$\delta = \sqrt{\frac{1}{\pi\mu\sigma f}} \tag{2-1}$$

where μ, σ, and f are relative permeability (dimensionless), electrical conductivity ($\Omega^{-1}\cdot m^{-1}$), and coil frequency (MHz), respectively. Skin depth is an important design parameter as the current does not flow homogeneously through a conductor, but is confined near the surface. The skin depth is the distance from the surface which contains ~64% of the

current and 80% of the power, and thus 99% of the current flows within a layer four times the skin depth from the surface. Therefore, given our field orientation, to achieve the maximal heating potential the radius of the disk must be at least 4 times the skin depth. Based on the skin depths of aluminum and copper (Table 2-2), the disk radii should be at least 548 μm and 436 μm for aluminum and copper, respectively, for an alternating field resonating at 360 kHz. Thus, the 1.70 ± 0.04 mm aluminum disks were chosen for the remaining proof of concept studies, as they meet the thermal seed skin depth design requirements and are able to generate sufficient temperature elevations for rapid high-temperature thermal ablation.

Table 2-2. Skin depth of aluminum and copper at a frequency of 360 kHz.

Material	Relative Permeability (μ)	Conductivity (σ)	Skin Depth (δ)
Aluminum	1.00	$3.766 \cdot 10^7$ S·m^{-1}	137 μm
Copper	1.00	$5.959 \cdot 10^7$ S·m^{-1}	109 μm

2.3.2 Composite scaffold fabrication and biocompatibility

Microporous polymer scaffolds composed of PCL, a slow-degrading biocompatible material, have previously been shown to recruit metastatic cancer cells *in vivo* [41]. In order to enable non-invasive application of focal hyperthermia to metastatic cells potentially captured by the scaffolds, 1.70 ± 0.04 mm aluminum disks were incorporated into the center of the polymer scaffolds. While induction heating in an alternating magnetic field is also possible with biocompatible metals, such as titanium or stainless steel, these metals are less malleable and more difficult to process. However, these options could be explored for clinical applications. Since aluminum is not biocompatible, the disks were first coated with a PCL film (Fig. 2-2A). To measure the thickness of the

film, it was partially delaminated (Fig. 2-2B). Profilometer measurements across the center of the polymer film-aluminum interface demonstrated a film thickness of 18.6 ± 12.4 μm (Fig. 2-2C, D). The stability of the films was evaluated by submerging coated disks in PBS at 37 ºC for 31 days, at which point the measured film thickness, 17.4 ± 10.9 μm, was not statistically different than the thickness of the Day 0 control (Fig. 2-2D). Film thickness on the Al disk was also not affected by heating at 15 $kA \cdot m^{-1}$ and 360 kHz for 10 min, as the resulting post-heating film thickness of 21.6 ± 7.1 μm was not statistically different from the non-treated control (Fig. 2-2D).

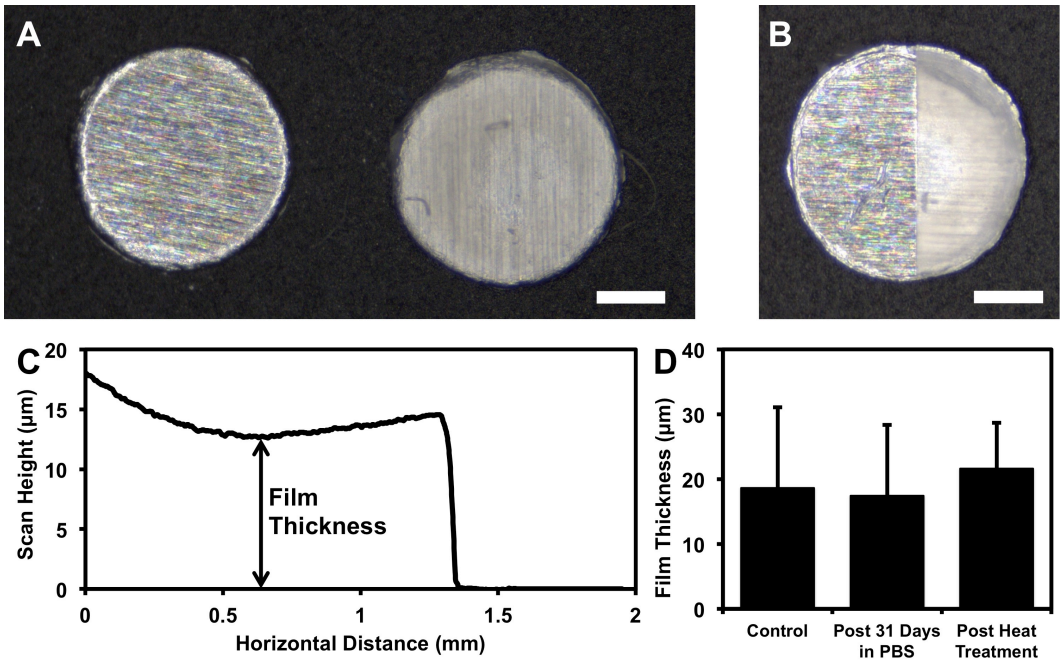

Figure 2-2. Stability of biocompatible PCL coating on Al disks. (A) Image of uncoated Al disk (left) and PCL coated Al disk (right). Scale bar indicates 500 μm. (B) Image of PCL coated Al after being partially delaminated for film thickness measurements. Scale bar indicates 500 μm. (C) Representative profilometer scan across middle of partially delaminated disk showing step change from polymer coating to exposed metal. Arrow represents the value used to quantify polymer film thickness. (D) Film thickness of untreated coating (control), after treatment in PBS at 37 ºC for 31 days, and after heat treatment at 15 $kA \cdot m^{-1}$ and 360 kHz, for 10 min. No statistically significant differences were observed. Film thickness data is mean ± SD, $n \geq 8$.

Previous reports have shown that polymer coatings on metal objects have improved biocompatibility in stents and dental implants [91, 92]. In one particular study, SaOS-2 (human osteosarcoma) cell proliferation was vastly improved on magnesium disks containing PCL coatings ranging from 300 nm to 1 μm in thickness [93]. Another study showed no inhibition of L929 fibroblast growth after direct contact with nickel-titanium stents coated with a 400 nm thick coating of poly(2-chloroparaxylylene) [94]. Given these findings, the PCL film thickness achieved on our aluminum disks should render them biocompatible. A simple dip coating method was used to coat the aluminum disks with PCL, similar to other reports on polymer coating of metal stents [95, 96]. More sophisticated techniques have used chemical vapor deposition polymerization to grow polymer films with greater control of thickness and consistency [94], but for our purposes, dip coating accomplished the goal of completely coating the aluminum disk quickly with sufficient thickness to ensure biocompatibility.

To incorporate the PCL-coated aluminum disks into microporous scaffolds, each disk was layered between two mixtures of PCL microparticles and 250-425 μm salt particles and pressed in a 5 mm die. The pressed composite material was then gas foamed and leached with water, resulting in a porous composite PCL-Al scaffold (Fig. 2-3). PCL-Al scaffolds were implanted subcutaneously in BALB/c mice and harvested 3-4 weeks later to evaluate scaffold biocompatibility by histology. H&E stained sections showed no signs of cytotoxicity in PCL-Al scaffolds as compared to PCL scaffolds, with PCL (Fig. 2-4A) and PCL-Al (Fig. 2-4B) tissue-laden scaffolds showing no statistical difference in the density of multinucleated cells, fibroblasts, new blood vessel formation, and

inflammatory infiltrates by pathological scoring (Table 2-3). These data demonstrate that the PCL-Al composite scaffolds are as biocompatible as unmodified PCL scaffolds *in vivo*.

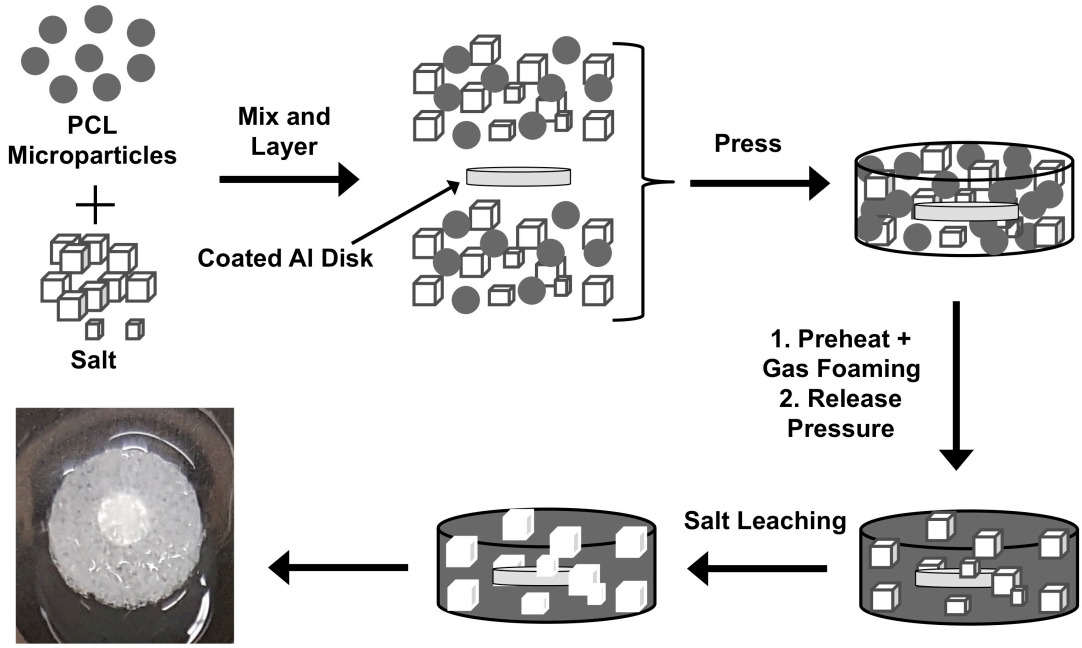

Figure 2-3. Fabrication of PCL-Al composite scaffolds. A PCL coated, 1.70 mm aluminum disk is layered in between two mixtures of PCL microparticles and sieved salt particles within a steel die and pressed. The pressed composite is then gas foamed to fuse polymer microparticles, after which the salt particles are leached out in water.

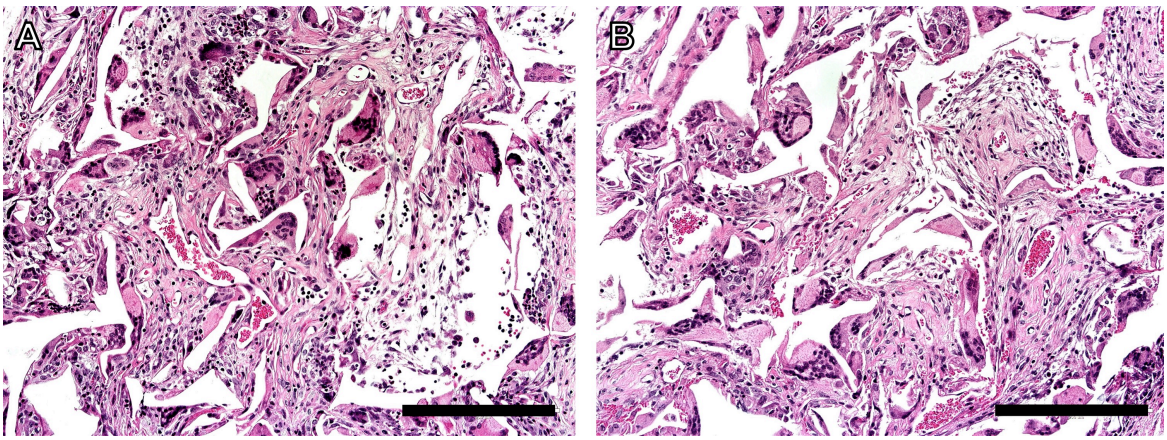

Figure 2-4. Histological analysis of implanted composite PCL-Al scaffolds. Tissue-laden scaffolds harvested 3-4 weeks post-implantation from the subcutaneous space. Hematoxylin and eosin stained sections of PCL (A) and PCL-Al (B) scaffolds. Scale bar indicates 200 μm.

Table 2-3. Pathologist scoring of tissue-laden composite scaffolds. Density of multinucleated cells, fibroblasts, new blood vessel formation, and inflammatory infiltrate were analyzed in a blind study (n = 3).

Density of	Scaffold Type	Average Scoring (0-3)	Standard Deviation
Multinucleated Cell	PCL	2.3	0.6
	PCL-Al	1.7	0.9
Fibroblast	PCL	2.4	0.5
	PCL-Al	1.8	1.1
New Blood Vessel Formation	PCL	2.3	0.3
	PCL-Al	1.9	1.0
Inflammatory Infiltrate	PCL	2.6	0.2
	PCL-Al	1.9	0.5

Composite PCL-Al scaffolds were also evaluated to verify that the ability to recruit metastatic breast cancer cells was not affected by the presence of the metal disk. To evaluate cancer cell recruitment to the scaffolds, a qRT-PCR approach developed for identifying melanoma cells [97] was modified to identify and evaluate genes highly expressed in 4T1 breast tumors. Eight genes (*FTH1*, *SPP1*, *LYZ2*, *PABPC1*, *EPCAM*, *LCN2*, *APOE*, and *MT2*) were selected as potentially highly expressed based on previously published microarray data (GSE64193) of harvested 4T1 tumors [98]. Further qRT-PCR analysis revealed that of these genes, *FTH1*, *APOE*, and *MT2,* were consistently highly expressed, as evidenced by low relative expression to the *GAPDH* reference gene, in two 4T1 primary tumors from our mouse model (Fig. 2-5A). *MT2* was selected to evaluate the presence of metastatic cells within the implanted scaffolds, as of the three genes highly expressed in 4T1 tumors, *MT2* exhibited the lowest expression in subcutaneous scaffolds from tumor-free mice (Fig. 2-5B). Both PCL and PCL-Al scaffolds exhibited statistically higher expression of *MT2* compared to their respective control scaffolds from tumor-free mice, which indicates the presence of metastatic cells (Fig. 2-5C). Additionally, there was no significant difference in *MT2* expression between

PCL and PCL-Al scaffolds in tumor-bearing mice (Fig. 2-5C). These results demonstrate that the ability of PCL scaffolds to recruit 4T1 tumor cells is unaffected by the addition of a metal disk to form the composite PCL-Al scaffold.

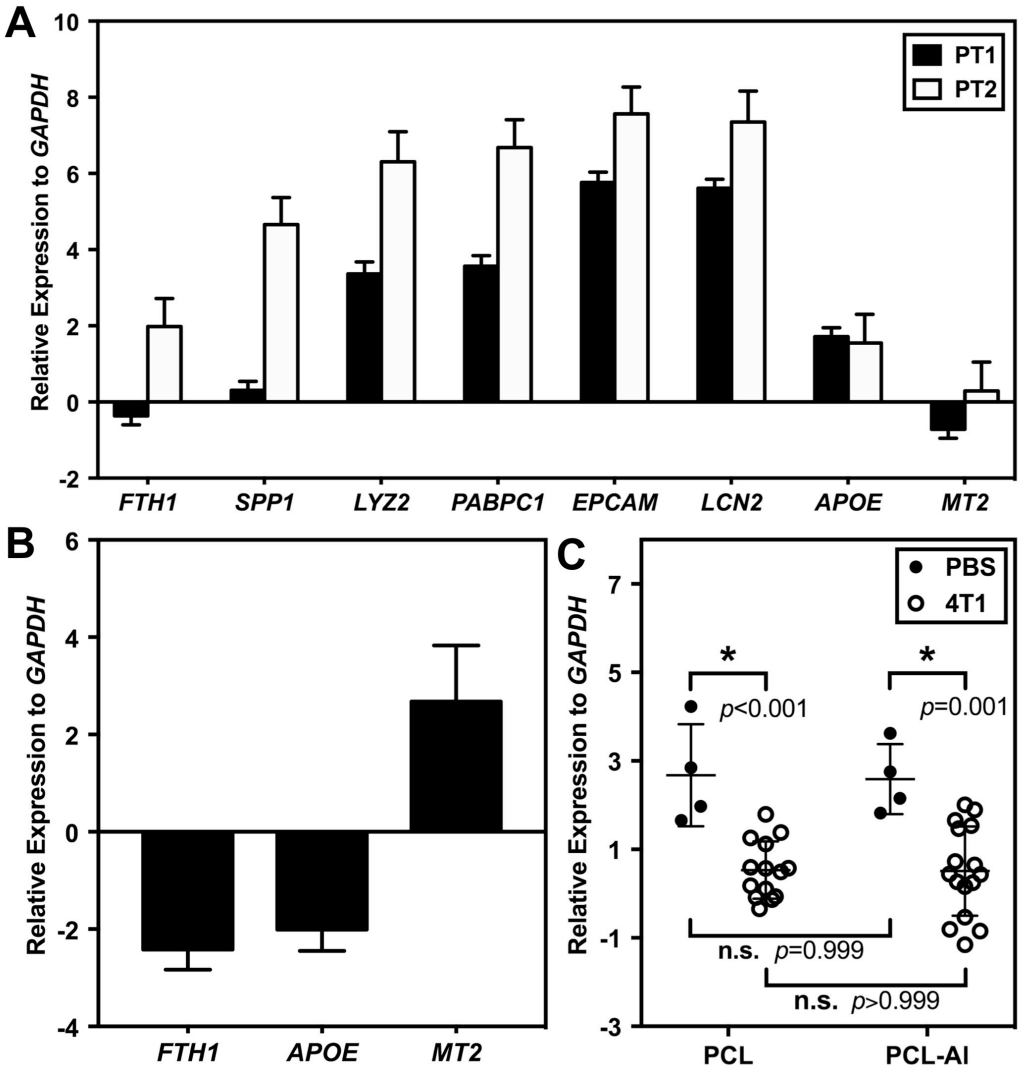

Figure 2-5: ***In vivo*** **capture of metastatic cancer cells to composite scaffolds.** (A) qRT-PCR analysis of 4T1 primary tumors, PT1 and PT2, to isolate high expressed genes. (B) Relative expression ($Ct_{GENE} - Ct_{GAPDH}$) is mean SD. Gene expression analysis of PCL scaffolds from tumor-free mice. Relative expression ($Ct_{GENE} - Ct_{GAPDH}$) is mean ± SD, n = 4. (C) Comparison of *MT2* relative expression in PCL and PCL-Al scaffolds from mice with either PBS only or 4T1 inoculations. Relative expression ($Ct_{GENE} - Ct_{GAPDH}$) is mean ± SD.

2.3.3 Ex vivo radiofrequency treatment of tissue-laden scaffolds results in cellular destruction

Since the goal was destroy cells infiltrating the scaffold through thermal ablation, the capability of the embedded disk to deliver a sufficient temperature rise for ablation in tissue-laden scaffolds was tested. PCL-Al composite scaffolds were implanted in the subcutaneous space and harvested a few weeks later. These tissue-laden composite scaffolds were treated for 4 minutes at 15 $kA \cdot m^{-1}$ and 360 kHz, and the temperature elevation at the far edge of the scaffold, where the lowest amount of heating is expected as this position is furthest away from the thermal seed, was 26 ± 4 ºC (Fig. 2-6A), which is sufficient for thermal ablation. For evaluation of cell death, treatment time was increased to 10 minutes. To evaluate the degree of cell damage within the scaffolds, tissue-laden PLC and PCL-Al scaffolds were treated for 10 minutes at 15 $kA \cdot m^{-1}$ and 360 kHz, and cellular viability within the scaffold was measured using a WST-1 assay (Fig. 2-6B). As expected, untreated PCL scaffolds, treated PCL scaffolds and untreated PCL-Al scaffolds displayed significantly higher cellular viability than control scaffolds that were submerged in 70% ethanol to kill the cells (negative control), since the thermal injury requires both electromagnetic induction and the thermal seed. Consequently, treated PCL-Al scaffold viability was substantially lower than that of untreated PCL or PCL-Al scaffolds or treated PCL scaffolds and showed no statistical difference with the 70% ethanol control. Resulting tissue damage following treatment of PCL (Fig. 2-6C) and PCL-Al (Fig. 2-6D) scaffolds was also evaluated by histology. H&E stained sections of treated PCL scaffolds showed no negative effects from the oscillating magnetic field (Fig. 2-6C). Conversely, in treated tissue-laden PCL-Al scaffolds, cells exhibited central

bleeding from the induced thermal ablation (Fig. 2-6D). For verification that the chosen treatment conditions could kill breast cancer cells, 4T1 cells were encapsulated in Matrigel surrounding a 1.70 mm Al disk. Using the same magnetic field strength, frequency, and duration as in the treatment of tissue-laden PCL-Al scaffolds, 4T1 cancer cells were successfully ablated, as evidenced by a substantial decrease in viability (Fig. 2-7). Taken together, these findings show that induced focal thermal ablation can effectively kill cells in the scaffold *ex vivo* and these parameters can also be applied to kill breast cancer cells *in vitro*.

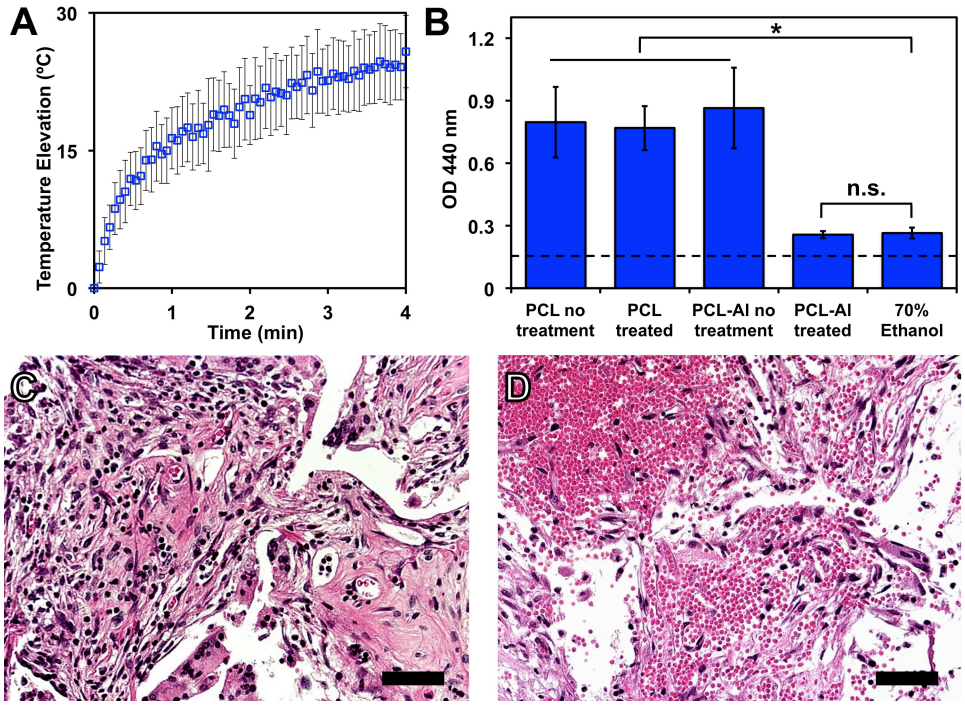

Figure 2-6. *Ex vivo* radiofrequency treatment ablates tissue-laden composite scaffolds. (A) Experimental temperature measurements at 1.85 mm radially from the center of the disk, near the edge of the scaffold, at 15 $kA \cdot m^{-1}$ and 360 kHz. Temperature data is mean ± SD, n = 4. (B) Viability assay (WST-1) of cells in tissue-laden scaffolds with and without *ex vivo* treatment for 10 min at 15 $kA \cdot m^{-1}$ and 360 kHz. Black dashed line indicates background signal from no scaffold control. (*) $P < 0.05$ compared to 70% ethanol. Viability data is mean ± SD, $n \geq 4$. (C, D) H&E stained sections of tissue-laden PCL (C) and PCL-Al (D) scaffolds following *ex vivo* treatment. Scale bar indicates 50 µm.

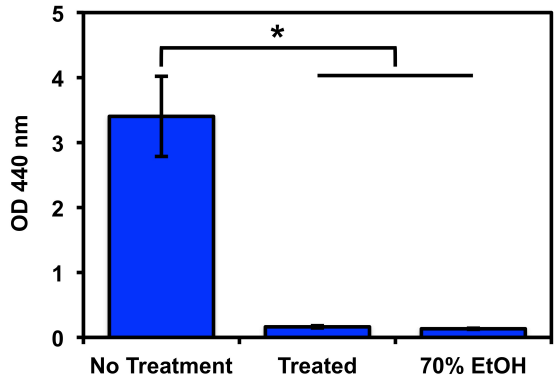

Figure 2-7. *In vitro* ablation of 4T1 cancer cells by induction heating. WST-1 viability assay performed on 4T1 cells encapsulated in Matrigel surrounding a 1.70 mm Al disk before and after treatment with an oscillating magnetic field at 15 kA·m^{-1} at 360 kHz for 10 min. As a positive control for cell death, samples treated with 70% ethanol were evaluated. (*) $P < 0.001$ compared to no treatment. Viability data is mean ± SD, n = 3.

2.3.4 Non-invasive, induced focal hyperthermia ablates tissue-laden composite scaffolds in vivo

In order to test the clinical relevance of our system by including the effects of blood perfusion, we applied our system to an *in vivo* model. One PCL-Al and one PCL scaffold were implanted in the subcutaneous space of a BALB/c mouse. After at least 3 weeks to allow for host integration of the scaffolds, the radiofrequency coil was placed over the implanted PCL-Al scaffold. Due to physical constraints of the coil diameter and the size of the mouse, the implanted PCL-Al scaffold was outside the center of the coil where the magnetic field is homogeneous, as magnetic field strength drops with axial distance away from the center. Thus, to achieve the desired 15 kA·m^{-1} field strength at the location of the scaffold, the field strength in the center of the coil was increased to 20 kA·m^{-1} and the implanted scaffold was arranged 9.25 mm below the center of the coil. IR images before (Fig. 2-8A) and during (Fig. 2-8B) treatment showed distinct localized heating of the composite scaffold upon treatment. Analysis of IR video revealed that the temperature

elevation achieved during treatment of implanted PCL-Al scaffolds, 26 ± 6 ºC (Fig. 2-8C), matched that of previous *ex vivo* results near the edge of the scaffold, 26 ± 4 ºC (Fig. 2-6A), validating that positioning of the implanted scaffold 9.25 mm below the coil set to 20 $kA \cdot m^{-1}$ achieves same heating profile as in the center of the coil at 15 $kA \cdot m^{-1}$. Acute effects of treatment resulted in a significant drop in 440 nm absorbance in treated PCL-Al scaffolds in comparison to the internal PCL controls using a WST-1 viability assay (Fig. 2-8D), indicating significant cell death in the treated PCL-Al scaffolds. To study chronic effects from the thermal ablation treatment, scaffolds were harvested three days following treatment for histological analysis. Nearby PCL scaffolds did not show any sign of cellular damage (Fig. 2-8E), whereas treated PCL-Al scaffold showed areas of tissue necrosis (Fig. 2-8F) by H&E. Previous studies report similar chronic effects after focal treatment, observing tissue necrosis as early as three days post-treatment in rat livers treated with a laser [89] and in LNCaP tumors treated with cryosurgery [88]. These findings indicate that these composite scaffolds can be used to kill cells within the scaffold through non-invasive, focal hyperthermia *in vivo*.

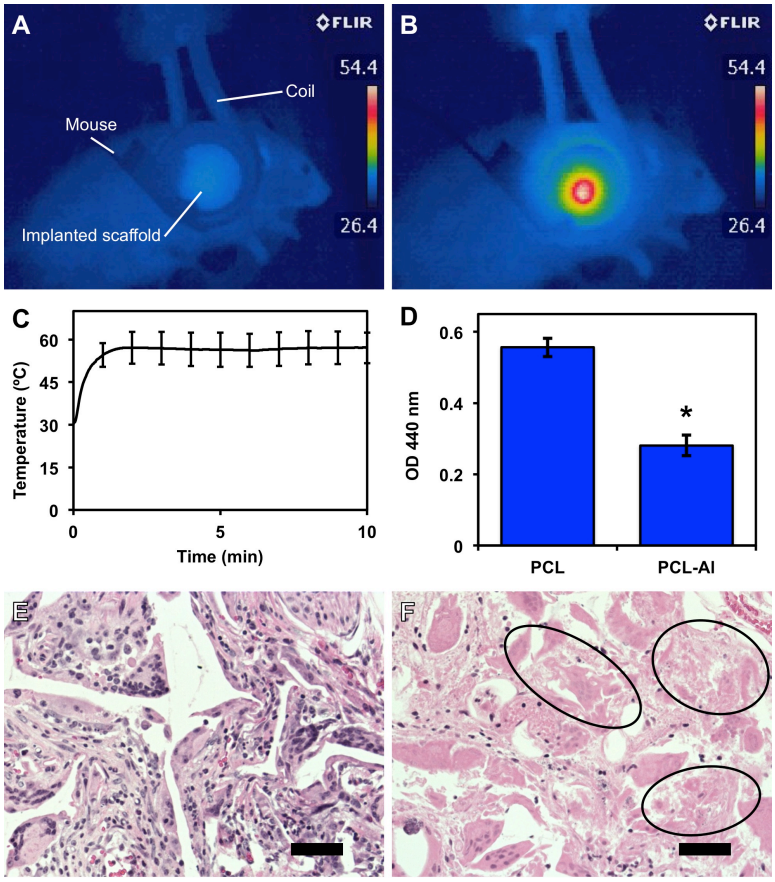

Figure 2-8. Induced focal hyperthermia ablates composite scaffolds *in vivo*. (A,B) IR camera images before (A) and during (B) treatment show localized heating of the composite scaffold. (C) Temperature of PCL-Al scaffold as a function of time during *in vivo* treatment, obtained from IR video analysis. Temperature data is mean ± SD, n = 3. (D) Viability assay (WST-1) of treated PCL-Al and PCL internal control immediately after treatment. (*) $P < 0.001$ compared to PCL. Viability data is mean ± SD, n = 3. (E, F) H&E and stained sections of tissue-laden PCL (E) composite PCL-Al (F) scaffolds three days post-treatment. Examples of necrotic areas are outlined by black circles. Scale bar indicates 50 μm.

2.4 Conclusions

The purpose of this study was to adapt a microporous polymer scaffold, which has previously been shown to recruit metastatic cells, for application of non-invasive focal hyperthermia. This was accomplished by using a conductive aluminum disk as a thermal seed. The heat generation of the disk could be tuned by changing disk diameter, magnetic field strength, and type of metal. Microporous composite PCL scaffolds with a centrally

located aluminum disk integrated successfully with host tissue after subcutaneous implantation. Experimental induction heating studies confirmed that tissue-laden composite scaffolds were capable of reaching the necessary temperatures for high-temperature hyperthermia. This resulted in the low cellular viability following treatment of *ex vivo* tissue-laden composite scaffolds under electromagnetic induction. Additionally, the *in vivo*, non-invasive, induction heating of subcutaneously implanted composite scaffolds proved to be localized and effective at ablating the desired tissue. These results demonstrate the ability of composite PCL-Al scaffolds to non-invasively eliminate infiltrating cells *in vivo*.

Chapter 3: Engineered polymer scaffolds with integrated electrodes for near-uniform electric field distribution during IRE treatment

3.1 Introduction

Focal therapies, such as cryoablation (Cryo) [56], thermal ablation (Heat) [55], and irreversible electroporation (IRE) [57], have been successful alternatives to surgical resection for treating solid tumors [99]. As with surgical resections, however, focal therapies may lead to recurrence at the treatment site as the therapy may fail to destroy the tumor entirely [100, 101]. Nevertheless, Cryo [81, 102-104], Heat [81, 105-107], or IRE [108] focal therapies offer an immunological advantage over surgical resections due to the tumor-specific antigens that are released from cancer cells into the local environment during treatment. These exposed antigens could be used as to trigger a systemic immune response against the cancer cells that are left behind from treatment and those that are disseminated throughout the body. Although such immune responses have been shown with focal therapy treatment alone [81], immunologic adjuvants, such as intradermal dendritic cell injection [104, 107] or anti-CTLA-4 immune checkpoint inhibitors [81, 103] are often used to stimulate a more robust anti-tumor response. The use of focal therapy, however, has yet to be applied to disseminated cancer cells.

The use of tumor lysates as a vaccine has also been demonstrated with microporous polymer scaffolds. In one study, lysates generated from harvested melanoma tumors treated with Cryo were incorporated into polymer scaffolds and implanted in mice with an established melanoma primary tumor. Following implantation, the lysate-loaded scaffolds induced an anti-tumor response that caused a decrease in primary tumor growth

and an improvement in overall survival in comparison to mice receiving blank scaffolds [82]. This suggests that anti-tumor immunity could be achieved by using focal therapy *in vivo* to expose tumorigenic antigens found in cancer cells recruited to a polymeric scaffold. In addition, the scaffold could be further engineered to enhance local immunomodulation in combination with the focal ablation. In this chapter, Heat, Cryo and IRE were applied to scaffolds *in vivo* to demonstrate their ability to ablate tissue in this context. Since the quality of the antigen produced will likely differ based on the method of ablation, and IRE has shown promise in eliciting higher levels T cell activation at lower tumor cell numbers [109], the ability to modify scaffolds for more homogeneous application of IRE was investigated.

3.2 Materials and methods

PCL scaffold fabrication and implantation

PCL microspheres were first prepared as previously described [41]. Briefly, a 6% (w/w) solution of PCL (DURECT; inherent viscosity = 0.65-0.85 $dL \cdot g^{-1}$) in dichloromethane was emulsified in a 10% (w/w) poly(vinyl alcohol) solution and homogenized at 10,000 rpm for 1 minute. Microspheres were lyophilized for 48 hours. PCL microspheres and sieved sodium chloride particles (250-425 μm) were mixed in a 1:30 (w/w) ratio and the contents were pressed to 3,300 lb (~15 kN) for 45 seconds in a 5 mm steel die (Specac). The pressed disks were heated at 60 ºC for 5 minutes on each side followed by foaming at 800 psig for ~24 hours, after which the gas was released at 17.5 CFH. After foaming, salt particles were removed by immersing the scaffolds in water for 90 minutes on a rocking platform. Scaffolds were sterilized by soaking in 70% ethanol, followed by rinsing with

sterile water and drying on a sterile gauze pad. Scaffolds were then stored at -80 ºC until further use.

Animal studies were performed in accordance with institutional guidelines and protocols approved by the University of Minnesota Institutional Animal Care and Use Committee (IACUC). Female C57BL/6 mice were purchased from The Jackson Laboratory, and mice were 6-8 weeks of age at the time of surgery. Two scaffolds were implanted into the subcutaneous space of the upper dorsal region in each mouse. Focal therapy experiments on tissue-laden scaffolds were performed 3-4 weeks following implantation.

In vivo focal ablation of PCL scaffolds

In vivo Cryo [110, 111], Heat [110], and IRE [112, 113] procedures previously described were applied to implanted tissue-laden scaffolds. Cryo treatment was performed using a 17-gauge IceSeed cryoablation needle (Galil Medical Inc.). A small incision was first made in the center of the implanted scaffold with an 18-gauge needle to allow insertion of the probe tip through the skin and scaffold. Probe tip temperature was set to –150 ºC, and freezing was performed conservatively under infrared thermographic guidance until the –40 °C isotherm reached the edge of the scaffold. The probe was then removed, and the scaffold was then passively thawed to body temperature. For Heat treatment, a 1 mm diameter brass extension tip was fitted to a temperature-controlled soldering iron tip (RadioShack) set to 150 ºC. A small incision was first made in the center of the implanted scaffold with a 25-gauge needle to allow insertion of the probe tip through the skin and scaffold. The scaffold was heated conservatively under monitoring with an infrared

camera (FLIR Systems Inc.) until the 50 °C isotherm reached the visible edge of the scaffold. The tip was then removed, and the scaffold was passively cooled to body temperature. A pair of customized two-probe electrodes connected to an electrical pulse generator (BTX ECM 830, Harvard Apparatus) was utilized for IRE treatment. The probe comprises two needle-type electrodes, each with a conductive tip (i.e. exposed without insulation). The needle electrodes (OD = 0.7 mm) were fixed with a center-to-center distance of 4 mm. Each needle electrode was coated with an insulating layer of heat shrink tubing, leaving a 3 mm tip for treatment. For treating implanted scaffolds, a ~1 cm skin incision was made beside the scaffold for greater exposure. The needle electrodes were inserted directly to the scaffold such that the electrodes were diametrically opposed. The electrical pulse generator was set to 99 pulses at 1000 V with 100 μs pulse durations at 1 Hz. All scaffolds were harvested either immediately or 24 hours following treatment for WST-1 cell viability or histological analysis, respectively.

Metal mesh fabrication and coating

Sheet of 304 stainless steel #50 woven wire mesh (The Mesh Company Ltd.), 0.348 mm aperture with 0.16 mm wire diameter, were punched with a 3/16 inch die and flattened gently with a press to make ~5 mm-diameter metal mesh disks. A copper loop (~2-3 mm diameter) was connected to the edge of each mesh to facilitate connection to an electrical pulse generator. To coat the metal disks with a polymer film, disks were dipped once into either a 10%, 5%, or 2.5% (w/w) solution of PCL (DURECT; inherent viscosity = 0.65-0.85 $dL \cdot g^{-1}$) in dichloromethane (Sigma). Coated disks were dried overnight at room temperature and ambient pressure.

Coating characterization

To characterize the polymer coating thickness, coated disks were first cut in half and later embedded in epoxy. The cut plane was then polished using successive finer grades of silicon carbide paper on a metallographic polisher. A final polish was done with 1 μm diamond paste on a Buehler Minimet Polisher (Illinois Tool Works Inc.). Samples were then sputtered with 50 Å of carbon and visualized with a JOEL 6500 scanning electron microscope (JEOL USA Inc.). Coating thickness was then measured from acquired images using ImageJ. Images were taken of 5 independent disks, with 4 different locations imaged per disk. 3 measurements were taken along the film in each image.

Composite scaffold fabrication

To fabricate composite "PCL-IRE" scaffolds for more uniform IRE application than probe-based methods, the pressed polymer/salt disk generated using the method described above for PCL scaffold fabrication was placed in between two PCL-coated metal mesh disks prior to foaming. After foaming, salt particles were removed by 90-minute incubation of the scaffolds in water on a rocking platform. PCL-IRE scaffolds were sterilized in 70% ethanol, rinsed with sterile water, dried on a sterile gauze pad, and stored at -80 ºC until further use.

Resistivity measurements

PCL scaffolds of varying thicknesses were fabricated for resistivity studies. For *in vitro* measurements, scaffolds loaded with 20 μL of 5 $mg \cdot mL^{-1}$ Matrigel (Corning) and for *ex vivo* measurements, tissue-laden scaffolds were harvested 4 weeks post-implantation.

Scaffolds were placed between two parallel plate electrodes connected to a PSM3750 frequency response analyzer with the IAI2 impedance analysis attachment (Newtons4th Ltd.) for impedance measurements. Impedance of loaded scaffolds was measured at frequencies of 1 MHz to 10 Hz at 1 V alternating current. Total resistance of the scaffold/electrode system was taken from the real part of impedance at high frequency (~1 MHz). This model assumes the scaffold/electrode system responds linearly with the total resistance and applied voltage at very short time scales (i.e. at high frequency), as is standard for materials containing electrolytes [114, 115]. Total measured resistance, R_T, is then expressed by the following formula:

$$R_T = R_S + R_R \tag{3-1}$$

where R_S is bulk resistance of scaffold (Ω) and R_R is residual resistance (Ω) from contact resistance with scaffold and electrode and resistances from electrodes and impedance analyzer. A linear regression fit was performed on the plot of total resistance as a function of thickness for Matrigel-loaded scaffolds. Bulk resistivity of scaffold, ρ (Ω·cm), was calculated by the following expression:

$$\rho = \frac{R_S A}{l} \cdot \frac{1\ cm}{10\ mm} \tag{3-2}$$

where R_S is bulk resistance of scaffold (Ω), A is cross-sectional area of scaffold (mm^2), and l is thickness of scaffold (mm). The bulk resistivity for Matrigel-loaded scaffolds was then calculated by multiplying the slope of the linear regression fit by the cross-sectional area of the scaffold. Due to the variability in diameter of harvested tissue-laden scaffolds, total resistance was plotted as a function of thickness divided by cross-sectional area, and bulk resistivity was then equal to the slope of the linear regression fit.

Modeling of electric field distribution from different electrode configurations

The IRE electric field distributions in the scaffolds were modeled using COMSOL Multiphysics version 5.3a (COMSOL Inc.) for parallel plate, two-probe, and metal mesh geometries.

Utilizing PCL-IRE scaffolds for ablation

B16-F10 melanoma cancer cells (ATCC CRL-6475) were loaded onto polymer scaffolds for *in vitro* IRE treatment studies. B16-F10 cells were suspended in 5 $mg \cdot mL^{-1}$ Matrigel (Corning) at 50E6 $cells \cdot mL^{-1}$. PCL or composite PCL-IRE scaffolds were submerged in 70% ethanol followed by two washes with culture media. Scaffolds were then partially dried on gauze pads for 5 minutes each side, and 20 µL of the Matrigel-B16-F10 was loaded into each scaffold followed by a 5-minute incubation at 37 ºC prior to IRE treatment. B16-F10 loaded PCL scaffolds were placed between two parallel plate electrodes connected to an electrical pulse generator (BTX ECM 830, Harvard Apparatus). For B16-F10 loaded composite PCL-IRE scaffolds, spring-loaded metal hooks (Minigrabber, Pomona Electronics) were attached to the copper loops on the metal meshes to connect PCL-IRE scaffolds to the electrical pulse generator. For *in vivo* treatment of tissue-laden scaffolds, a dorsal skin incision was made 3-4 weeks following implantation to expose copper loops for attachment through spring-loaded metal hooks. All cell-laden scaffolds were then treated at specified, calculated electric fields with 99 pulses with 100 µs pulse duration at 1 Hz. Specified electric fields were calculated by dividing applied voltage by the thickness of the loaded scaffold. Following treatment, scaffolds were tested for cellular viability using the WST-1 assay.

WST-1 viability assay

The viability of cells in tissue-laden or B16-F10 loaded scaffolds was determined by treating the cells with cell viability reagent WST-1 (Takara Bio). Harvested scaffolds were transferred to 500 μL of fresh media (DMEM containing 10% fetal bovine serum, 1% L-glutamine, and 1% penicillin-streptomycin; Thermo Fisher Scientific). Microscissors were used to mince the scaffolds into small pieces. 50 μL of WST-1 reagent was added to each sample and incubated at 37 ºC for 2 hours for tissue-laden and B16-F10 loaded PCL and PCL-IRE scaffolds. For the study involving tissue-laden composite PCL-IRE scaffolds, a 3.5-hour incubation was performed due to timing restrictions. A media sample was used as a negative control for background measurement. As negative controls for viable cells, tissue-laden scaffolds were treated with 70% ethanol and acellular, Matrigel-only scaffolds were used for *in vivo* focal therapy and *in vitro* IRE treatment, respectively. For ethanol treatment, tissue-laden scaffolds were minced in 500 μL of 70% ethanol and incubated on ice for 1 hour. Following ethanol incubation, the samples were centrifuged at 14,000 x *g* for 5 minutes, and the supernatant was replaced with 500 μL of fresh media prior to addition of 50 μL of WST-1 reagent. After WST-1 incubation, all samples were vortexed and centrifuged at 14,000 x *g* for 5 minutes. 400 μL of supernatant was filtered through a 70 μm filter. Triplicates of 100 μL per sample were transferred to a 96-well plate. The absorbance of each well was measured at a wavelength of 440 nm with a Synergy H1 microplate reader (BioTek Instruments).

Tissue sectioning and histological analysis

For histological analysis of ablation effects, tissue-laden PCL scaffolds were removed whole from the subcutaneous space 24 hours following Cryo, Heat, and IRE treatment. For histological analysis of the biocompatibility of PCL-IRE scaffolds, PCL or PCL-IRE scaffolds were removed from the subcutaneous space 3-4 weeks after implantation. The tissue-laden scaffolds were fixed in 10% buffered formalin, embedded in paraffin, and sectioned at 4 μm using an HM 315 microtome (Microm). For PCL-IRE scaffolds, metal mesh electrodes were removed from composite scaffolds prior fixation. Slides were stained with hematoxylin and eosin (H&E) or terminal dUTP nick-end labeling (TUNEL) for histological analysis. TUNEL staining was done using the ApopTag Peroxidase In Situ Apoptosis Detection Kit (MilliporeSigma) following the manufacturer's instructions. Slides were imaged using an EVOS FL Auto Microscope (Thermo Fisher Scientific).

Statistical analysis

Data are presented as the mean ± standard deviation (SD), and *p*-values were determined using an unpaired Student's *t*-test.

3.3 Results and discussion

3.3.1 In vivo application of focal therapy to tissue-laden scaffolds

As a proof-of-principle that different modalities of focal therapy can be applied to kill cells within the scaffolds *in vivo*, PCL scaffolds were implanted into the dorsal, subcutaneous space of C57BL/6 mice. After 3-4 weeks to allow for tissue infiltration, scaffolds were then exposed to Cryo, Heat, or IRE treatment. Each focal therapy was

applied with an external applicator: a 1.5 mm wide cryoablation needle for Cryo, a 1 mm brass probe attached to an electric heater for Heat, and a two-probe electrode applicator with 4 mm spacing for IRE. The immediate effects on cellular viability within the scaffolds following these treatments were measured using a WST-1 assay (Fig. 3-1). Viability of cells within the scaffolds dropped by 98%, 89%, and 89% following Cryo, Heat, and IRE, respectively. Treatment with 70% ethanol was utilized as a control for complete killing of all cells within the tissue-laden scaffold.

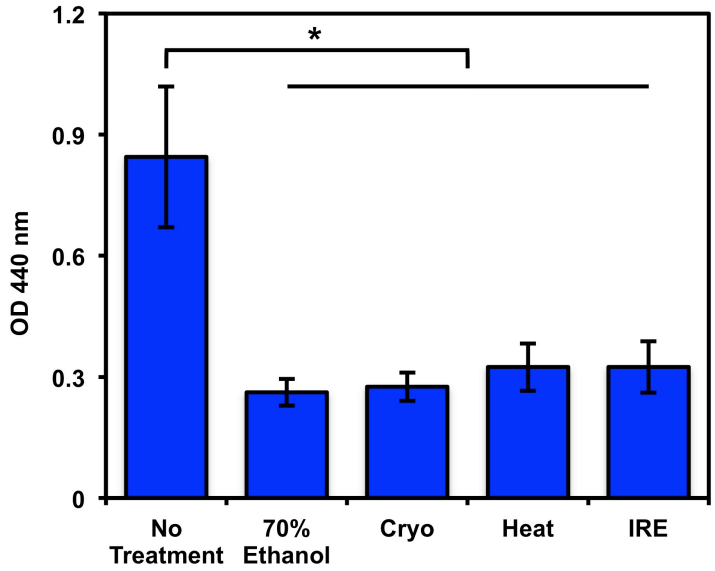

Figure 3-1. *In vivo* focal therapy applied to tissue-laden scaffolds causes loss of cellular viability. Viability assay (WST-1) of cells in tissue-laden PCL scaffolds harvested immediately following Heat, Cryo, and IRE treatment. (*) $P < 0.001$ compared to untreated samples. Viability data is mean ± SD, $n \geq 11$.

Cell death was further analyzed by TUNEL staining on histological sections of PCL scaffolds treated with focal therapy. TUNEL staining can be used to examine cell death by labeling cleaved DNA strands, as nuclear DNA fragmentation is a hallmark of cell death [116, 117]. To allow enough time for enzymatic degradation of nuclear DNA [116],

scaffolds were harvested 24 hours following treatment. Fig. 3-2 shows sequential sections from scaffolds treated with Cryo, Heat, and IRE stained with H&E and TUNEL. All three treatments show elevated numbers of TUNEL-positive cells in comparison to the untreated scaffold. Taken together, these results show that various types of focal therapy can be applied to successfully ablate cells within tissue-laden scaffolds *in vivo*.

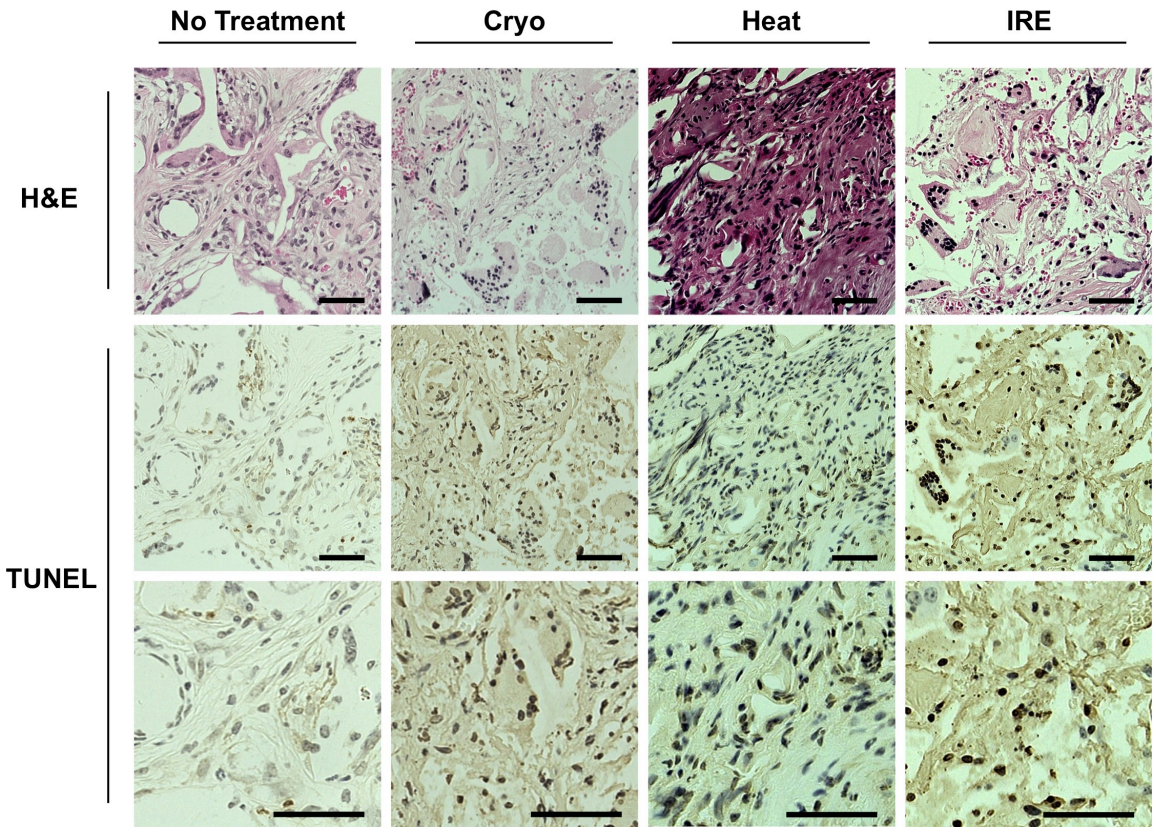

Figure 3-2. *In vivo* histological analysis of cell death in treated tissue-laden scaffolds. Images of H&E (top row) and TUNEL (center and bottom row) staining of untreated tissue-laden PCL scaffolds (first column) or 24 hours after *in vivo* application of Cryo (second column), Heat (third column), and IRE (fourth column) treatment. Higher magnification of images of TUNEL images (bottom row). Scale bar indicates 50 μm.

Although these results show that Cryo, Heat, and IRE focal therapies can kill cells recruited to polymer scaffolds *in vivo*, downstream immune activation can vary

depending on the type of focal therapy [81]. Differences might be attributed to how the therapy affects antigen release and structure. Collaborative work with the Shimizu and Bischof groups at the University of Minnesota has used B16-F10 murine melanoma as a cancer model to investigate how the release of tyrosinase-related protein-2, a melanoma specific antigen [118], from different focal therapy conditions affects T cell activation *in vitro*. Recent results have shown that B16-F10 cell lysates from IRE treatment produce the strongest T cell activation when compared to thermal and cryoablation [109]. Local application of IRE has also been demonstrated to induce systemic effects *in vivo*; IRE treatment of a subcutaneous kidney primary tumor led to a reduction or suppression of growth following a secondary tumor challenge [108]. Thus, we hypothesized that IRE could be used to ablate cancer cells in the scaffold to release tumor specific antigens and elicit a cancer specific immune response. For this study, B16-F10 cells were used to investigate necessary IRE parameters to ablate melanoma cells within PCL scaffolds.

3.3.2 Determining IRE field parameters necessary to kill melanoma cells

Since several parameters, such as electric field strength, number of pulses, pulse duration, and frequency, affect treatment efficacy of IRE, we evaluated the necessary conditions to kill B16-F10 murine melanoma cells in polymer scaffolds *in vitro*. Melanoma cells were suspended in Matrigel and loaded into PCL scaffolds, and these cell-laden scaffolds were then placed in between two parallel plate electrodes connected to a pulse generator (Fig. 3-3A). This geometry was utilized so that application of a voltage drop across the plates would create a homogeneous electric field distribution throughout the scaffold and the strength of the electric field could be taken to be the applied voltage potential divided by

the gap between the plates [119]. The number of pulses and pulse duration were kept constant at 99 and 100 μs, respectively, because these parameters have been shown to be effective at killing LNCaP prostate cancer cells in suspension at low electric field strengths [120]. In order to determine the necessary electric field strength to kill B16-F10 cells, B16-F10 loaded scaffolds were treated with electric field strengths ranging from 0 $V \cdot cm^{-1}$ to 2000 $V \cdot cm^{-1}$, and viability was measured using the WST-1 assay (Fig. 3-3B). Compared to cells in untreated scaffolds, viability of cells in treated scaffolds dropped by 33% and 94% at 500 and 1500 $V \cdot cm^{-1}$, respectively. Samples treated at 2000 $V \cdot cm^{-1}$ showed no statistical difference compared to acellular control scaffolds. These results show similar trends as treated LNCaP prostate cancer cells in suspension: relatively high cellular viability at 500 $V \cdot cm^{-1}$ or below and near complete cell death at 1500 $V \cdot cm^{-1}$ or higher. These electric field parameter values have also been effective for soft tissue ablation *in vivo*, as 1000 – 2500 $V \cdot cm^{-1}$ has commonly been used [120]. The results suggest that electric fields of at least 1500 $V \cdot cm^{-1}$ would be sufficient to treat melanoma cells that have metastasized to the scaffold. Although parallel plate electrodes create a homogeneous electric field distribution throughout the scaffold, this electrode geometry may not be directly integrated with the scaffold as solid plates would render the scaffold pores inaccessible for the majority of the scaffold surface, which could inhibit cell infiltration and proper integration and vascularization to the scaffolds, therefore impeding cancer cell recruitment. Other electrode geometries will therefore be investigated to apply lethal IRE parameters throughout the scaffold.

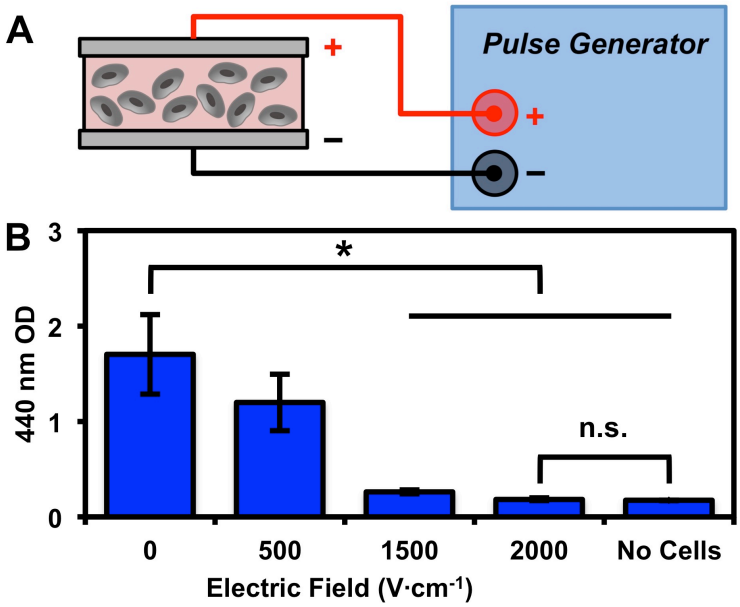

Figure 3-3. Characterizing IRE parameters necessary to ablate melanoma cells using parallel plate geometry *in vitro*. (A) Schematic of *in vitro* set up: B16 melanoma cells are suspended in Matrigel and loaded into a PCL scaffold; the scaffold is then placed in between parallel plate electrodes, which are connected to a pulse generator. (B) Viability as determined by WST-1 assay of B16 cells from cell-laden scaffolds at varying electric field strengths after 99 pulses with 100 µs pulse duration at 1 Hz. (*) $P < 0.01$ compared to untreated samples. Viability data is mean ± SD, n = 3.

3.3.3 Modeling electric field distribution with different electrode geometries

Modern applications of IRE involve the use of two or four cylindrical probes to deliver treatment to the tumor. These probes are designed to be minimally invasive, but unlike parallel plate electrodes, cylindrical probe electrodes deliver a heterogeneous electric field, with the strength of the field decreasing with an r^{-1} dependence, where r is the distance from the probe [121]. Achieving a more uniform electric field within the area of treatment would allow for better control over the quality of the tumor-specific antigen released, impacting the downstream immune response. In the context of the scaffold, metal meshes could be utilized in place of solid plates to allow for cell infiltration while potentially delivering a more homogeneous electric field than is achievable by cylindrical

probes. To determine whether this alternative electrode design could be a substitute for the parallel plate electrodes, we modeled the spatial electric field distribution for three different electrode geometries: parallel plate, two-probe, and metal mesh electrodes.

In order to correctly model the expected electric field distribution, the resistivity of the *in vitro* Matrigel-loaded scaffold was evaluated. Due to the low concentration of B16-F10 cells loaded within the scaffold, the resistivity of Matrigel-only scaffolds were used a model to represent the *in vitro* system. Resistivity was evaluated by measuring the overall resistance of Matrigel-loaded scaffolds of varying thicknesses. By plotting the overall resistance as a function of scaffold thickness, the resistivity of the Matrigel-loaded scaffold, 228 Ω·cm, was calculated from the slope of the linear regression fit across the data, in which the slope represents the resistance normalized by the scaffold thickness (Fig. 3-4A). To determine the resistivity of PCL scaffolds with a microenvironment resembling what would be *in vivo*, PCL scaffolds were implanted in the dorsal subcutaneous space in mice and harvested 3-4 weeks later to allow for host cell infiltration into the scaffold. Due to the variable diameter of harvested scaffolds, overall resistance was plotted as a function of scaffold thickness normalized to cross-sectional area, where the slope of the linear regression fit was then equal to the resistivity of tissue-laden scaffolds, 312 Ω·cm (Fig. 3-4B). For both Matrigel-loaded and harvested tissue-laden scaffolds, calculated resistivity values were within the range of measured values in other soft tissues, such as the kidney, muscle, and thyroid [122]. For proof-of-concept, resistivity of Matrigel-loaded scaffolds was then utilized to determine the effect of electrode configuration on expected electric field distribution. Calculated resistivity value

for tissue-laden scaffolds could be used in the future to further refine model expectations in complex animal studies.

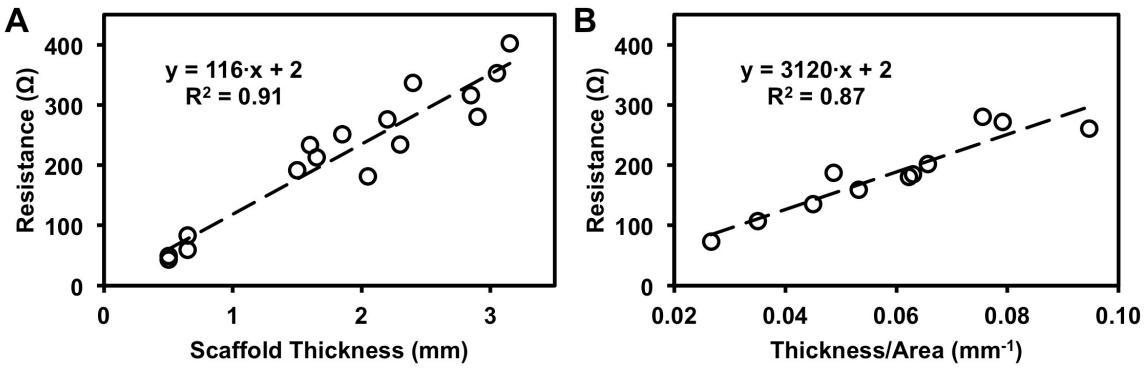

Figure 3-4. Analysis of resistivity of Matrigel-loaded and tissue-laden PCL scaffolds. (A) Overall resistance of Matrigel-loaded scaffold measured in parallel plate configuration as a function of scaffold thickness. (B) Overall resistance of tissue-laden PCL scaffold measured in parallel plate configuration as a function thickness divided by cross-sectional area. Each scaffold is represented as an open circle from an average of 3 technical replicates per scaffold. Four different scaffold heights were evaluated, with four scaffolds per height tested for Matrigel-loaded scaffolds and three scaffolds per height for tissue-laden scaffolds.

In collaboration with the Bischof group, the calculated resistivity for Matrigel-loaded scaffolds was then implemented into a COMSOL model to generate predicted electric field distributions for parallel plate, two-probe, and metal mesh electrode geometries. Electric field distribution throughout the scaffold for all geometries was graphed as a rectangular cross-section across the diameter and as a circular cross-section averaged across the thickness of the scaffold. As expected for parallel plate electrodes (Fig. 3-5A), the electric field distribution is uniform throughout the scaffold (Fig. 3-5D, G). However, the modeled distribution for the two-probe electrode geometry demonstrates that the electric field decays radially away from the electrodes (Fig. 3-5E, H). Since the scaffold thickness is much smaller than the length of the needle electrodes, the electric field

distribution does not vary along the height of the scaffold (Fig. 3-5E). The model was then applied to PCL scaffolds with a metal mesh electrode geometry (Fig. 3-5C). The rectangular cross-section (Fig. 3-5F) reveals that the electric field varies the most near the top and bottom of the scaffold, in proximity to the metal mesh, but the electric field is otherwise nearly uniform throughout most of the scaffold. The circular cross-section averaged throughout the thickness of the scaffold shows the relatively small impact of the metal mesh electrodes on the heterogeneity of the expected electric field distribution throughout the scaffold, as the distribution is nearly uniform (Fig 3-5I) and resembles that of a parallel plate geometry (Fig. 3-5G).

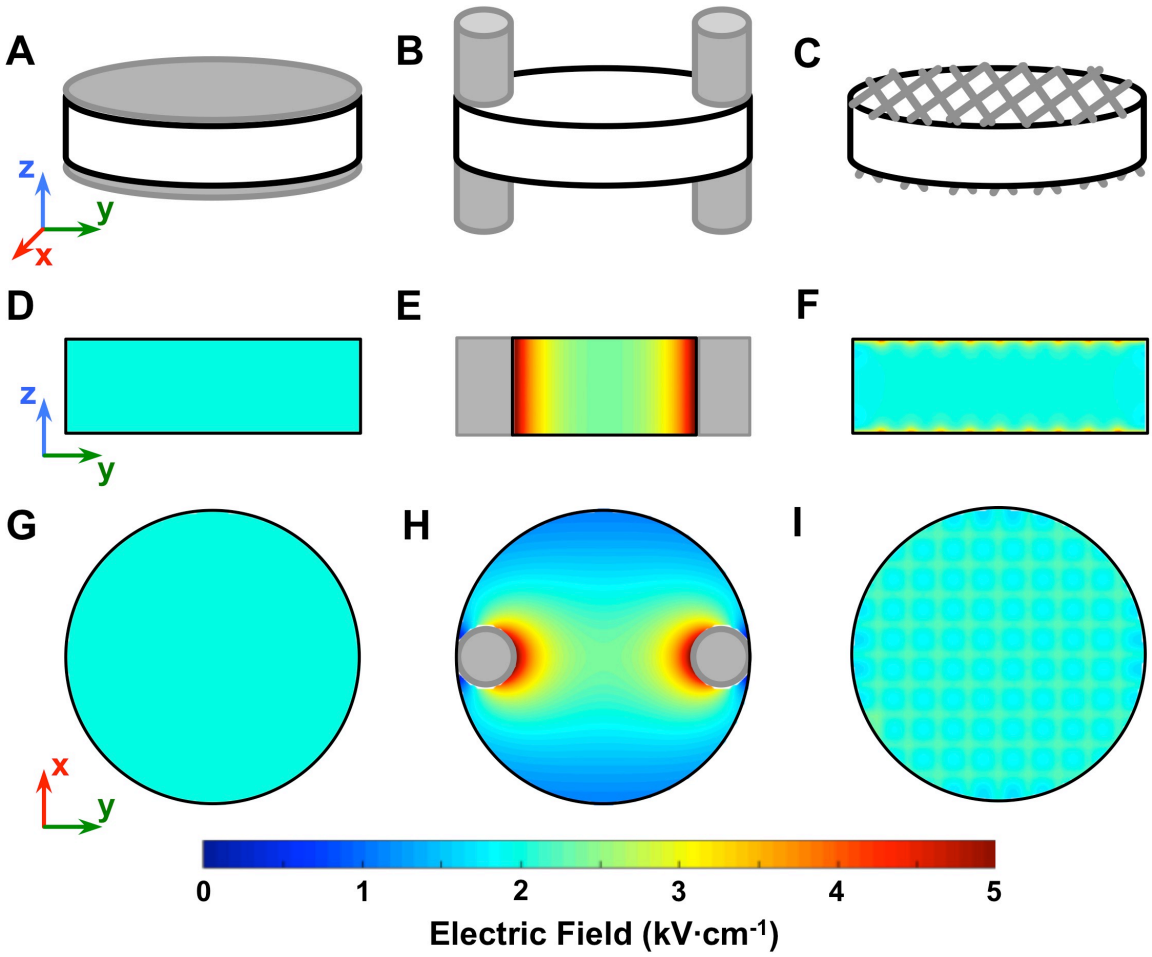

Figure 3-5. Predicted electric field distribution from parallel plate, two-probe, and metal mesh electrode geometries. (A-C) Schematics of parallel plate (A), two-probe electrode (B), and metal mesh (C) configurations with polymer scaffolds. (D-F) Rectangular cross-section of electric field distribution along diameter of scaffold using parallel plate (D), two-probe (E), and metal mesh (F) electrode geometries. (G-I) Circular cross-section of electric field distribution averaged across thickness of scaffold using parallel plate (G), two-probe (H), and metal mesh (I) electrode geometries.

To further compare the electric field distribution between the three electrode geometries, the field strength field distribution across the scaffold volume was evaluated for each configuration. For quantitative comparison of electric field heterogeneity in each geometry, the simulation was constrained such that the average electric field strength across the scaffold for each electrode geometry was 2000 $V \cdot cm^{-1}$. When the simulation results for electric field strength were averaged across the scaffold geometry, as expected

the average was 2000 $V \cdot cm^{-1}$ for each geometry, but the two-probe electrode geometry had a larger standard deviation of 710 $V \cdot cm^{-1}$ compared to the metal mesh electrode, 310 $V \cdot cm^{-1}$. The heterogeneity in electric field values were further analyzed by plotting the frequency distribution of field strength values across the scaffold volume for parallel plate (Fig. 3-6B), two-probe (Fig. 3-6C), and metal mesh (Fig. 3-6D) electrode configurations. The distribution of the two-probe electrode geometry was the most heterogeneous, with only 26% of the volume centered around the 2000 $V \cdot cm^{-1}$ target value, in the range of 1750-2250 $V \cdot cm^{-1}$, while 87% of the scaffold volume in the metal mesh geometry was in the 1750-2250 $V \cdot cm^{-1}$ range. As a consequence of the near-uniform distribution from the metal mesh electrode configurations, 97% of the scaffold volume was at or above the 1500 $V \cdot cm^{-1}$ threshold needed to kill B16-F10 cells *in vitro* (Fig. 3-3B), compared to only 74% of the scaffold volume for the two-probe electrode geometry. The geometry of the metal mesh could be further optimized in the future to achieve a more uniform distribution using this modeling approach; however, this metal mesh geometry was tested for proof-of-principle demonstration that PCL scaffolds could be modified with built-in electrodes for more uniform IRE treatment than that of conventional approaches. A more uniform IRE treatment could lead for better control of antigen release and presentation for downstream immunotherapy applications.

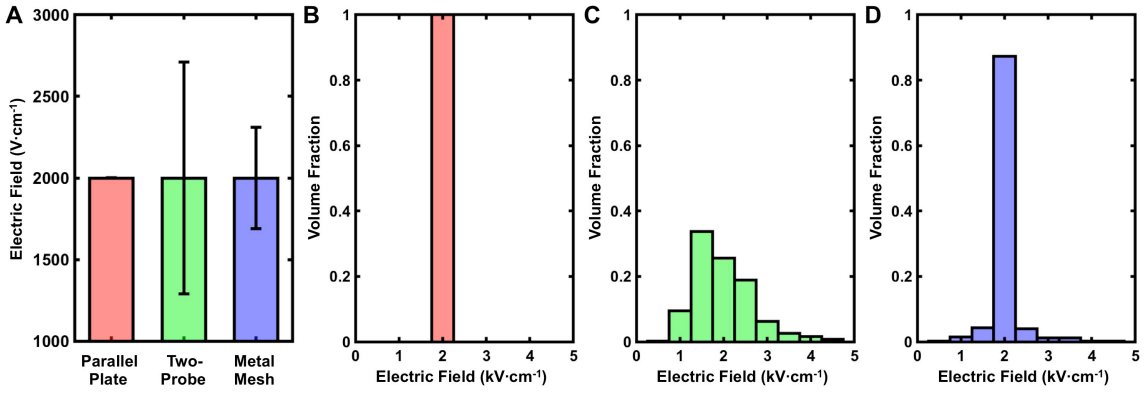

Figure 3-6. Evaluating spatial electric field distribution across different electrode geometries. (A) Average electric field strength across scaffold volume for parallel plate, two-probe, and metal mesh electrode geometries using COMSOL model. Error bars indicate SD. (B-D) Frequency distribution histograms for simulated electric field values throughout the scaffold for parallel plate (B), two-probe (C), and metal mesh (D) electrode geometries.

3.3.4 Fabricating IRE composite scaffolds

In order to fabricate scaffolds with built-in electrodes for a near-uniform IRE treatment, metal meshes made of stainless steel were attached to the top and bottom faces of the scaffold. To aid in connecting metal meshes to electrical pulse generator, a copper loop was attached to each metal mesh. Since neither the alloy of stainless steel nor copper used are biocompatible, the mesh assembly was first coated in a film of PCL, using the same dip coating procedure described in Chapter 2, section 2.3.2. However, the procedure had to be modified because films of PCL were present within the pores of the mesh (Fig. 3-7A, 10 % w/w), which would block cell infiltration. The presence of polymer within the pore may have been caused by PCL coming out of solution before the evaporation of organic solvent was able to destabilize the wetting of the pores. It was hypothesized that this effect could be limited by decreasing the concentration of PCL in the coating solution to allow dewetting of the organic solvent within the pores prior to PCL precipitation. As the concentration of PCL in the coating solution decreased from 10 to 2.5 %w/w, the

number of blocked pores also decreased (Fig. 3-7A). As no blocked pores were seen at 2.5 %w/w PCL in dichloromethane (Fig. 3-7A), this solution was used as the coating solution for the meshes. Scanning electron microscopy images of cross sectional slices (Fig. 3-7B) demonstrated a film thickness of 2.40 ± 0.96 µm (Fig. 3-7C). As mentioned previously in Chapter 2, section 2.3.2, a PCL coating of 300 nm to 1 µm has been shown to be sufficient to ensure biocompatibility of metal objects [93]. Despite the variability in measured film thickness, the thinnest film measurement was above this threshold for biocompatibility (Fig. 3-7C). Coated meshes were placed on either side of a pressed PCL/salt disk and then gas foamed to fuse the polymer from the mesh and the scaffold together. The composite scaffold was then leached in water to remove the salt crystals (Fig. 3-7D, E).

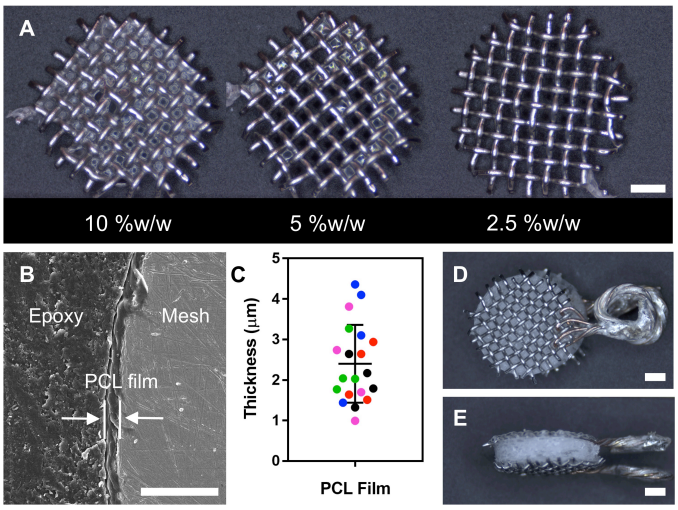

Figure 3-7. Characterization of PCL-coated mesh. (A) Optical image of scaffolds after dip coating in 10 %w/w (left), 5 %w/w (center), or 2.5 %w/w (right) PCL in dichloromethane. Scale bar indicates 1 mm. (B) Scanning electron micrograph of cross section of coated metal mesh, with section of PCL film outlined by white parallel lines between arrows. Scale bar indicates 10 µm. (C) Measurement of PCL film thickness from electron micrographs. Each color represents an independent wire mesh (n = 5), and each dot represents the average of 3 measurements of different areas in one image. 4 separate locations were imaged per mesh. Film thickness is also shown as mean ± SD. (D, E) Optical images of composite PCL-IRE scaffolds from the top (D) and side (E). Scale bar indicates 1 mm.

To investigate biocompatibility of composite PCL-IRE scaffolds, PCL scaffolds with attached metal meshes were implanted subcutaneous in C57BL/6 mice. After 3-4 weeks, scaffolds were harvested and biocompatibility was analyzed through histology. H&E sections of regular PCL (Fig. 3-8A) and PCL-IRE (Fig. 3-8B) scaffolds show no noticeable signs of cytotoxicity from the addition of metal meshes. These results show that the modified PCL-IRE scaffolds are as biocompatible as regular PCL scaffolds.

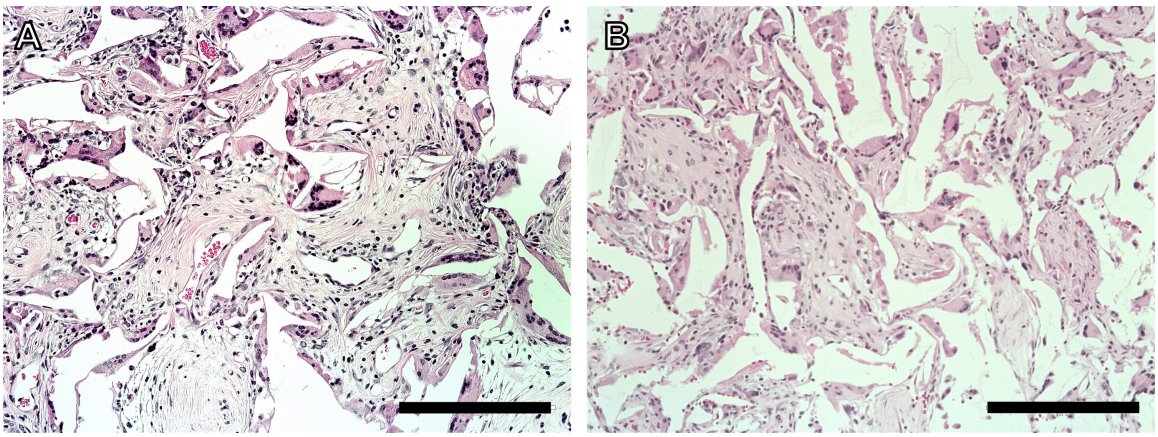

Figure 3-8. Histological analysis of implanted PCL-IRE scaffolds. Tissue-laden PCL scaffolds with (PCL-IRE) and without (PCL) metal mesh electrodes were harvested 3-4 weeks post-implantation. (A, B) H&E stained sections of PCL (A) and PLC-IRE (B) scaffolds. Scale bar indicates 200 μm.

3.3.5 Use of PCL-IRE composite scaffolds to kill melanoma cells in vitro

To validate the ability of the composite scaffolds to kill melanoma cells under the same parameters as with the parallel plate configuration, B16-BL6 melanoma cells were suspended in Matrigel and loaded into the composite scaffolds. The two meshes were then connected to the electrical pulse generator and treated under the same voltage potential that generated a homogeneous 2000 $V \cdot cm^{-1}$ electric field strength under the parallel plate geometry. The resulting cellular viability is shown in Fig. 3-9. As seen previously with the parallel plate geometry, there was no statistical difference between

treated composite scaffolds and acellular composite scaffold controls. These findings show that fabricated PCL-IRE composite scaffolds can effectively kill melanoma cancer cells within the scaffold *in vitro*.

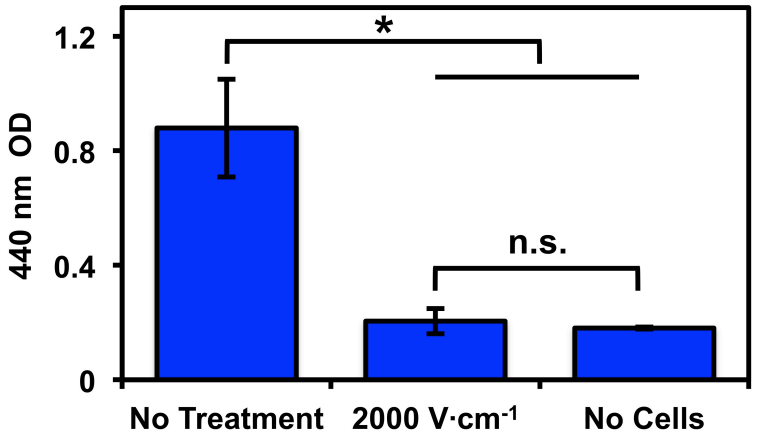

Figure 3-9. *In vitro* B16 viability following treatment in PCL-IRE composite scaffold. Viability assay (WST-1) of PCL-IRE scaffolds containing B16 cells, without and with treatment at 2000 $V \cdot cm^{-1}$, or Matrigel only control. (*) $P < 0.001$ compared to untreated samples. Viability data is mean ± SD, $n \geq 4$.

3.3.6 Application of IRE to tissue-laden composite PCL-IRE scaffolds in vivo

To test the feasibility of utilizing PCL-IRE scaffolds to treat infiltrating cells *in vivo*, PCL-IRE scaffolds were implanted in the subcutaneous space in C57BL/6 mice. After 3-4 weeks to allow for host cell infiltration, a skin incision was made to expose the copper loops that are attached to metal meshes of the composite scaffolds. These copper loops were used to facilitate connection of PCL-IRE scaffolds to the electrical pulse generator. The same conditions used previously to treat melanoma cells *in vitro*, both with parallel plate and metal mesh geometries, were used to treat implanted, tissue-laden composite PCL-IRE scaffolds. Post-treatment viability of cells within scaffolds demonstrated that cells within 1 of the 4 treated scaffolds were completely killed (Fig. 3-10). The remaining

treated scaffolds resulted in either partial decrease in cell viability in comparison to no treatment controls or no decrease in viability. Further optimization is needed to understand why some scaffolds were ineffectively treated, but it could have occurred from endogenous tissue remaining on copper loops, thus inhibiting proper electrical contact to the instrument, and/or electrical current pathways through tissue adjacent to the scaffold reducing the voltage potential across the metal meshes. Nonetheless, PCL-IRE scaffolds with embedded metal mesh electrodes can be utilized to kill infiltrating cells from host through IRE *in vivo*.

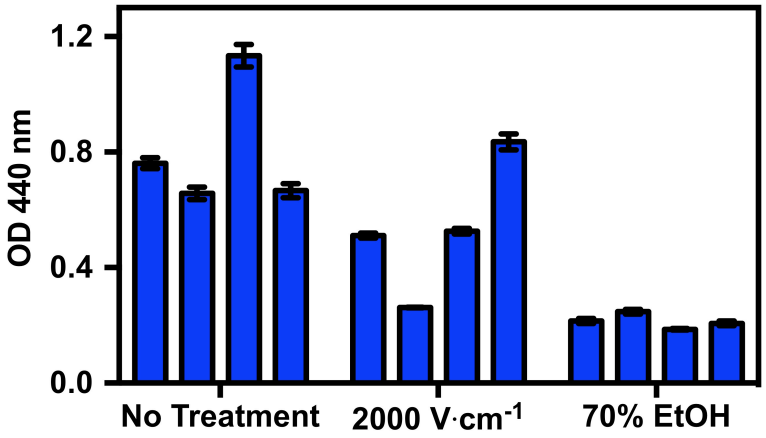

Figure 3-10. IRE treatment of implanted PCL-IRE scaffolds *in vivo*. Viability assay (WST-1) of untreated PCL-IRE scaffolds, treated PCL-IRE scaffolds, and control scaffolds in which cells were killed with 70% ethanol. Each bar represents an individual scaffold. Viability data for each individual scaffold is shown as mean ± SD of three technical replicates.

3.4 Conclusions

In summary, PCL scaffolds can be modified with metal mesh electrodes to generate electric fields that are more homogeneous than those generated using the traditional two-probe geometry. *In vitro* studies determined that PCL-IRE scaffolds could kill embedded melanoma cells as effectively as parallel plate electrodes under the same applied voltage,

number of pulses, pulse duration, and frequency. Additionally, composite PCL-IRE scaffolds could be utilized for IRE treatment of infiltrating host cells *in vivo*, but further optimization is necessary to increase robustness of the treatment. Future studies will apply this technology to target disseminated melanoma cells for the potential release of melanoma-specific antigens for generation of a downstream cancer-specific immune response.

Chapter 4: Utilizing liposomes for inducible release upon irreversible electroporation

4.1 Introduction

In Chapter 3, PCL scaffolds were modified with metal meshes to create a semi-uniform electric field towards the goal of using irreversible electroporation (IRE) to ablate recruited cancer cells in such a manner that the tumor antigens released upon cell lysis could be utilized to induce an anti-cancer immune response. Although a systemic anti-tumor immune response has been shown through the use of IRE alone [108], the associated immune activation from energy-based ablation is typically too weak for a robust response [104]. The use of adjuvants to stimulate the immune system in conjunction with focal therapy has been shown to improve anti-tumor immunity. Adjuvants such as intratumor injection of dendritic cells to aid in T cell activation [104], intraperitoneal injection of immune checkpoint inhibitors [81], and peritumoral injection of danger signals such as unmethylated CpG oligodeoxynucleotides (CpG-ODN) [123], which are typically found in bacteria, have previously been shown to assist in triggering an innate immune response [124].

Adjuvants might be especially necessary when targeting disseminated cancer cells in the scaffold because of the significantly smaller amount of antigen release in comparison to the release when treating a solid tumor. Although the scaffolds may be modified to attract more cancer cells [39], the increase may not be sufficient to incite a robust response. Modifying the scaffold to release immunostimulants upon application of focal therapy could modulate the local environment and boost the immune response to target

disseminated cancer cells. The incorporation of the adjuvants CpG-ODN and pro-inflammatory cytokine granulocyte-macrophage colony-stimulating factor (GM-CSF) along with B16 tumor lysate into biodegradable polymer scaffolds implanted subcutaneously has been shown to repress primary tumor growth in immunocompetent mice [82]. This method, however, uses tumor lysate harvested from a solid tumor to introduce cancer-specific antigens to the scaffold, which may not be possible for cases involving non-resectable tumors or disseminated cancer cells. Additionally, the release from this system is correlated with the degradation of the polymer in the body [125]; with inducible release, the release of adjuvants can be controlled by a physical cue, such as pH [126], infrared light [127], heat [128], or an electric field [129]. Thus in theory, release of immunostimulants could be timed with IRE treatment of disseminated cancer cells at the scaffold to generate a stronger immune response. This chapter will focus on incorporating of inducible release mechanisms in the polymer scaffold upon IRE treatment.

4.2 Materials and methods

Scaffold fabrication

To fabricate polymer scaffolds, PCL microspheres were first prepared as previously described [39]. Briefly, for PCL microspheres, a 6% (w/w) solution of PCL (DURECT; inherent viscosity = 0.65-0.85 $dL \cdot g^{-1}$) in dichloromethane was emulsified in a 10% (w/w) poly(vinyl alcohol) solution and homogenized at 10,000 rpm for 1 minute. Microspheres were lyophilized for 48 hours and then mixed with sieved sodium chloride particles (250-425 μm) in a 1:30 (w/w) ratio. Microsphere/sodium chloride mixtures were pressed to 3,300 lbs. (15 kN) for 45 seconds in a 5 mm steel die (Specac). Pressed disks were heated

at 60 ºC for 5 minutes on each side and then foamed at 800 psig for ~24 hours, after which the gas was released at 17.5 CFH. Salt particles were removed by immersing disks in water for 90 minutes on a rocking platform. Polymer scaffolds were sterilized by soaking in 70% ethanol, followed by rinsing with sterile water and drying on a sterile gauze pad. Scaffolds were then stored at -80 ºC until further use.

Aminolysis of polymer scaffolds

The aminolysis reaction with PCL scaffolds was adapted from Nisbet et al. [130]. PCL scaffolds were placed in a 0.05 M ethylenediamine (MilliporeSigma) in isopropyl alcohol (MilliporeSigma) and incubated at ambient pressure at either room temperature for 10 minutes or at 37 ºC for 24 hours. Scaffolds were then rinsed three times with water, with a five-minute soak between each rinse followed by a final 1 hour soak prior to use.

Primary amine characterization

Primary amine functionalization of PCL scaffolds was characterized by fluorescence labeling using fluorescamine (MilliporeSigma). PCL scaffolds were placed in a 10 mM fluorescamine solution in acetone. Immediately after, an equal volume of borate buffer, pH 9, was added to the fluorescamine solution. After 10 minutes, scaffolds were rinsed three times with water, with a five-minute soak between each rinse. Scaffolds were imaged using an EVOS FL Auto Microscope (Thermo Fisher Scientific) equipped with 357 nm/447 nm excitation/emission wavelength light filter.

Liposome formation

Liposomes were prepared by the hydration of lipid thin-films followed by extrusion. Briefly, either 1,2-dipalmitoyl-sn-glycero-3-phosphocholine (DPPC) or 1-palmitoyl-2-oleoyl-glycero-3-phosphocholine (POPC) were combined with 0.1 mol% biotin-labeled phospholipid, 1,2-dipalmitoyl-sn-glycero-3-phosphoethanolamine-N-(biotinyl), in chloroform to form a 13.3 mM total lipid solution. All lipids were purchased from Avanti Polar Lipids, Inc. 4 μmol (300 μL) total lipid solution was placed in a 10 mL round bottom flask and heated to 50 ºC and dried using a rotatory evaporator (LabTech Srl) at 60 rpm under vacuum for 5 minutes to form a thin lipid film. The film was then hydrated with 500 μL of 90 mM carboxyfluorescein (MilliporeSigma) in 1 M Tris buffer, pH 8, with 300 mM NaCl for 1 hour at 50 ºC with periodic gentle agitation. Hydrated lipids were then extruded through 100 nm, 1 μm, or 10 μm polycarbonate membrane (Whatman) 27 times using a manual extruder (Avanti Polar Lipids Inc.) at 50 ºC or room temperature for DPPC or POPC liposomes, respectively. Liposomes were separated from unencapsulated solution using a PD MiniTrap G-25 Sephadex column (GE Healthcare) using 300 mM NaCl in 1 M Tris buffer, pH 8, solution prior to use. Liposome size was characterized by dynamic light scattering using a Nanotrac Flex particle size analyzer (Microtrac).

IRE treatment and dye release

130 μL of prepared liposome solutions were placed in an electroporation cuvette (Fisher Scientific) with aluminum plate electrodes spaced 2 mm apart. The two electrodes were then connected to a BTX ECM 830 electrical pulse generator (Harvard Apparatus) in

order to induce a homogeneous electric field throughout the liposome solution. The electric field was determined by the dividing the applied voltage by the distance between electrodes. Liposomes were subjected to either 500, 1500, or 2000 $V \cdot cm^{-1}$, in 99 square pulses with 100 μs pulse duration at a frequency of 1 Hz. Release of encapsulated carboxyfluorescein following electroporation was determined from the fluorescence intensity of the solution. 100 μL of treated liposome solution was placed in a well of a black, round-bottom, 96-well plate and fluorescence intensity (490 nm/520 nm excitation/emission wavelengths) was quantified with a microplate reader (BioTek Instruments Inc.). For positive controls representing total release, liposomes were mixed in equal volume with 2% Triton X-100 (MilliporeSigma) to disrupt liposome assembly for complete release. Percent Release (%), was calculated using untreated negative controls and positive controls by the following formula:

$$Percent\ Release\ (\%) = \frac{F_S - F_-}{2*F_+ - F_-} \times 100 \quad (4\text{-}1)$$

where F_S, F_-, and F_+, are the fluorescent intensities of treated sample, negative control, and positive control, respectively.

4.3 Results and discussion

4.3.1 Chemical modification of polymer scaffolds for protein conjugation

Although similar microporous polymer scaffolds have previously been modified for controlled release of chemokines *in vivo* by incorporating chemokines in polymer microparticles through encapsulation or coating [42, 131], release rates depend on degradation of the polymer and are not inducible. As the goal of this work was to maximize the impact of adjuvant release by coupling it to the focal ablation, we sought to

incorporate the adjuvants in particles could release their cargo upon IRE. Fig. 4-1 demonstrates the strategy for introducing drug-loaded particles onto the surface of polymer scaffolds. In the first step, the polymer surface will be modified with primary amines to facilitate attachment of streptavidin through 1-ethyl-3-(3-dimethylaminopropyl)carbodiimide hydrochloride (EDC), a heterobifunctional crosslinker. Then, drug-loaded particles surface-labeled with biotin will be incubated with streptavidin-polymer scaffolds. This will result in particles being bound to polymer scaffolds due to the strong non-covalent binding between streptavidin and biotin [132].

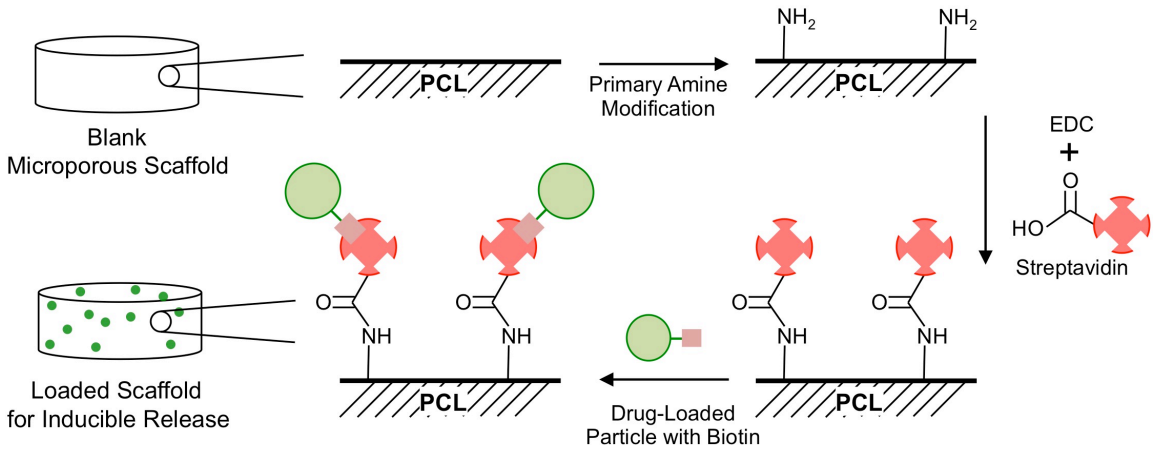

Figure 4-1. Schematic for attaching drug-loaded particles onto microporous polymer scaffolds. PCL scaffolds will be chemically modified with primary amines. EDC will be used to catalyze the covalent bond between the carboxyls on streptavidin and primary amines on modified PCL scaffolds. The strong streptavidin-biotin interaction will then facilitate binding of drug-loaded particles (green sphere) labeled with biotin (red square) to PCL scaffolds for inducible release.

Heterobifunctional linkers have been used to conjugate proteins, such as brain-derived neutrophobic factor, to PCL scaffolds [133]. These heterobifunctional crosslinkers catalyze a covalent bond between two different functional groups that are naturally found in biological samples, such as primary amines, carboxylic acids, and sulfhydryl groups.

Commonly used heterobifunctional crosslinkers facilitate the conjugation between sulfhydryl-to-amine or carboxyl-to-sulfhydryl moieties to attach proteins to other target proteins or surfaces. Since the polymer backbone of PCL does not contain these active functional groups for the attachment of biological molecules [134], chemical modification of the polymer surface will be required prior to utilizing heterobifunctional linkers to attach streptavidin to the surface. Streptavidin is a protein that is composed of four identical polypeptide units that can each bind to one biotin molecule. The amino acid composition of this polypeptide lacks the cysteine required for conjugation involving sulfhydryl chemistry, but does contain 13 amino acids with carboxylic acid functional groups [135]. Thus, a widely used carboxyl-to-amine heterobifunctional linker, EDC, could be used to couple streptavidin to a surface containing primary amines to form stable amide bonds [136]. Introduction of amine groups to the surface of PCL scaffolds can be achieved through an aminolysis reaction. This reaction has been used in the textile industry to modify synthetic polyesters, such as poly(ethylene terephthalate), to improve properties such as wettability [137] and dyeability [138]. By utilizing small chain alkanes with multiple primary amine functional groups, such as ethylenediamine, aminolysis of biodegradable polyesters, such as PLG [134] and PCL [130], results in cleaved polymer chains with terminal primary amines (Fig. 4-2).

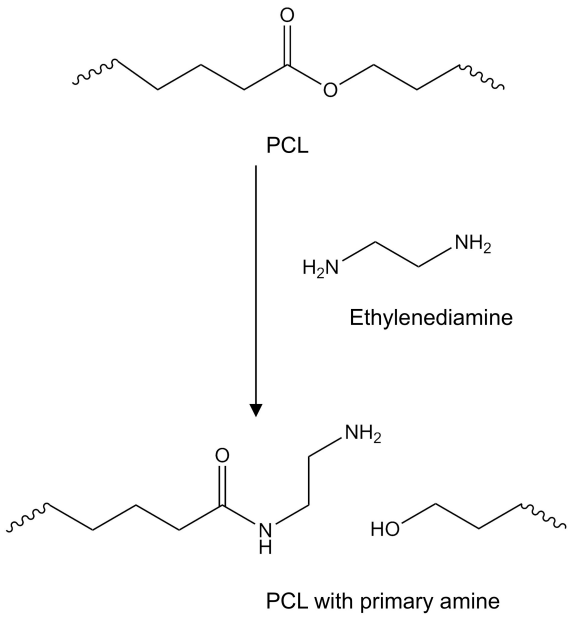

Figure 4-2. Aminolysis method to introduce primary amines to biodegradable polyesters. Ethylenediamine can be used to break the backbone of polyesters, such as PCL, to introduce primary amines, which may be utilized to attach proteins to polymer scaffolds.

To optimize reaction conditions for introducing primary amines on the surface of PCL scaffolds, three different incubations with 0.05 M ethylenediamine were tested: 10 minutes at room temperature, 24 hours at room temperature, and 24 hours at 37 ºC. To evaluate the yield of amines on the polymer surface following the reaction, the scaffolds were incubated with fluorescamine, which fluoresces upon reaction with a primary amine [139]. The fluorescence images of PCL scaffolds following aminolysis and fluorescamine labeling can be seen in Fig. 4-3A-D. PCL scaffolds treated without ethylenediamine (Fig. 4-3A) served as a background control, and no noticeable difference in fluorescence intensity can be seen between controls and PCL scaffolds undergoing a 10-minute reaction time at room temperature (Fig. 4-3B). With longer reaction conditions, 24 hours, a noticeable increase in signal intensity is observed, with the greater intensity observed at elevated temperatures (Fig. 4-3D) in comparison to room temperature (Fig. 4-3C). These

observations were quantified by analyzing the fluorescence signal intensity from the images taken of each scaffold (Fig. 4-3E). Signal intensities were normalized to results from scaffold samples treated without ethylenediamine (Fig. 4-3A). Both 24-hour reaction conditions at room temperature and 37 ºC demonstrated significantly greater fluorescence signal intensity over background, with 24-hour reaction at 37 ºC yielding the greatest signal. This confirmation that primary amines can be incorporated onto the surface of PCL scaffolds indicates that streptavidin could be linked to these modified scaffolds using a carboxyl-to-amine heterobifunctional crosslinker, such as EDC, upon which drug-loaded particles with surface-labeled biotin could be conjugated to the PCL scaffolds through the strong molecular affinity between streptavidin and biotin.

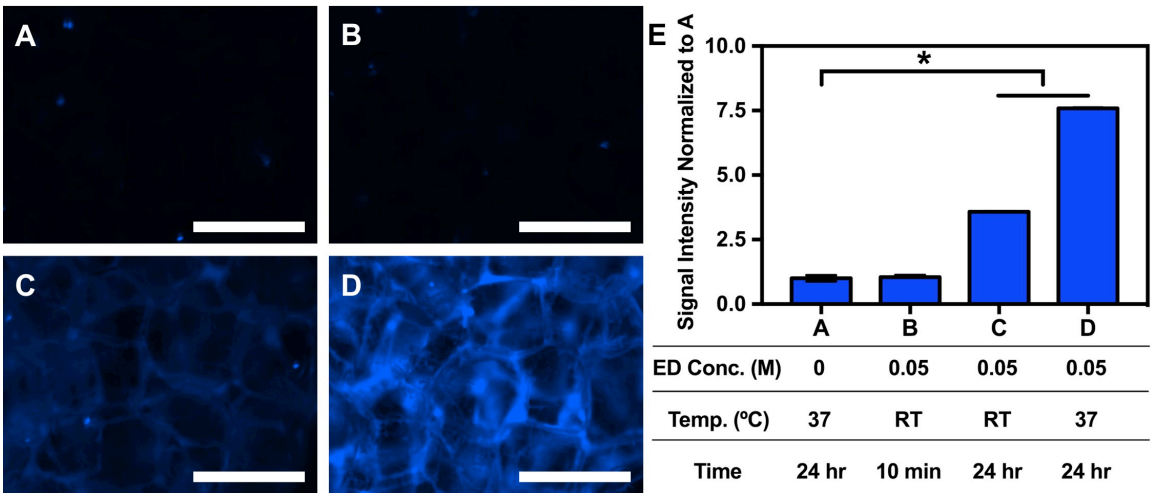

Figure 4-3. Evaluation of surface primary amines on PCL scaffolds through fluorescamine treatment. (A-D) Fluorescence imaging of microporous PCL scaffolds after no ethylenediamine (ED) reaction (A) or 0.05 M ethylenediamine in isopropyl alcohol at room temperature (RT) for 10 minutes (B) or 24 hours (C), or at 37 ºC for 24 hours (D). All scaffolds were treated with fluorescamine to fluorescently label primary amines. Scale bar indicates 500 µm. (E) Average signal intensity taken from scaffold samples normalized to scaffolds treated without ethylenediamine. Intensity values were averaged over the three individual scaffold samples per reaction condition. Average intensity per scaffold was quantified from four separate images taken for each scaffold. (*) $P < 0.001$ compared to scaffolds treated without ethylenediamine. Normalized signal intensity data is mean ± SD, n = 3.

4.3.2 Drug-loadable carriers for IRE-inducible release

Several forms of drug carriers have been formulated for inducible release. Local release of a payload for some systems can be triggered by small molecules. In one system, vascular endothelial growth factor (VEGF) was encapsulated in a polyacrylamide hydrogel, which contained non-covalent cross-links from a homodimeric binding protein, FK binding protein 12. Upon exposure to a competitive inhibitor, FK506, dissociation of the binding proteins expanded the hydrogel structure, causing release of encapsulated VEGF [140]. Another system encapsulated transgenic cell lines in a cellulose capsule. These transgenic cell lines were engineered to sense for a specific antibiotic, doxycycline or erythromycin, which would then induce expression of therapeutic proteins and the enzyme cellulase to break down the capsule, thereby releasing these therapeutics [141].

Inducible release caused by energy-based applications, such as heat and electroporation, has also been utilized. A common drug carrier for these applications is liposomes. Liposomes are self-assembled, spherical vesicles formed by a membrane bilayer commonly composed of phospholipids. Early uses of liposomes in the 1970s were for drug delivery, due to their ability to entrap both aqueous drugs in the interior and hydrophobic drugs within the lipid membrane [142]. Since then, the field of liposomes has progressed to clinical relevance with fifteen FDA-approved liposomal drug formulations for a wide variety of applications such as fungal infections, influenza, and even for treatment of metastatic breast and pancreatic cancer [143].

Release of encapsulated contents through heat from specific liposome formulations has also been extensively studied [144]. Above a critical temperature, the membrane of these thermo-sensitive liposomes becomes significantly more permeable, causing release of encapsulated drugs [128]. Thermo-sensitive liposomes loaded with chemotherapeutic drugs, such as doxorubicin, designed with a target release temperature above normal body temperature of 40-42 ºC, are being implemented in combination with focal hyperthermia. This combination therapy can increase the efficacy of treatment by destroying a larger portion of the tumor than focal hyperthermia alone by treating tumor cells at the periphery of thermal ablation through local release of chemotherapeutic drugs [145]. One such formulation, ThermoDox, is currently in phase III clinical trials for treatment of non-resectable liver cancer in combination with focal hyperthermia [146].

IRE can also trigger release from drug-loaded liposomes. In liposomes and cells, the lipid bilayer is electrically insulating, and high electric fields can cause membrane deformation, resulting in pores [71, 129, 147, 148]. These pores cause a significant increase in permeability, allowing encapsulated molecules to diffuse out. This phenomenon has been utilized in conjunction with IRE *in vivo* to treat human liver cancer, Hep3B, in mice. Intratumoral injection of liposomes loaded with the tumor suppressor NVP-BEZ235 [149] prior to IRE increased treatment volume and decreased cancer cell growth in comparison to IRE treatment alone [150]. Due to their applications as an effective drug carrier and their inducible release capability under IRE, liposomes will be investigated for inducible release with polymer scaffolds.

For attachment to scaffolds through streptavidin-biotin interaction, liposomal formulations containing biotin were prepared by a commonly used procedure [151-153]. A mixture of phospholipids with and without a biotin headgroup is dissolved in a polar organic solvent, such as chloroform, that reduces both hydrophobic and hydrophilic interactions (Fig. 4-4A). The chloroform is then evaporated off to produce a lipid thin film (Fig. 4-4B). Addition of an aqueous buffer causes the film to hydrate and swell and leads to the formation of liposomes with biotin incorporated in the membrane (Fig. 4-4C) [152, 154]. Extrusion through a nanoporous membrane is then applied to achieve a more uniform size distribution (Fig. 4-4D) [155].

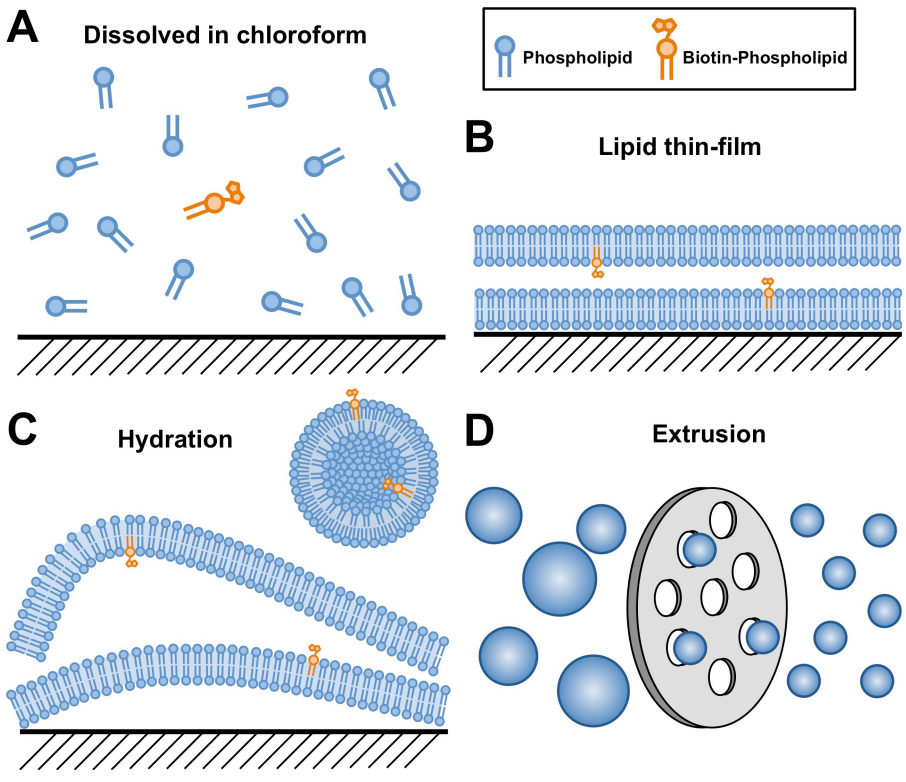

Figure 4-4. Schematic of biotinylated liposome preparation. (A) Mixture of phospholipids with and without biotin in a polar organic solvent. (B) Production of lipid thin-film following evaporation of organic solvent. (C) Liposome formation from hydration of lipid films. (D) Extrusion of liposomes to control size distribution.

To quantify release following IRE treatment, an established release assay using carboxyfluorescein was implemented [127, 156-158]. Carboxyfluorescein is a fluorescent molecule that at high concentrations, ≥ 90 mM, becomes self-quenched, losing 97-98% fluorescence [156]. This self-quenching property can be used to quantify the amount of release from the liposomes, as the encapsulated carboxyfluorescein is at a sufficiently high concentration to become self-quenched, but the carboxyfluorescein released from liposomes following IRE treatment will become diluted in the surrounding medium, and fluorescence intensity can be correlated to the amount released. Two separate liposome characteristics, formulation and size, were investigated for their effect on release upon IRE. Two formulations were chosen such that the lipid bilayer would be in different phases at body temperature, a gel state and a liquid crystalline state. In the gel state, the phospholipid hydrocarbon chains are oriented in a straight fashion, perpendicular to the plane of the bilayer, resulting in a more dense and rigid membrane. Conversely in the liquid crystalline state, there is enhanced mobility of phospholipid hydrocarbons, causing more fluidity in the membrane [159]. The gel and liquid crystalline state occur below and above the phase transition temperature (T_C), respectively [159, 160]. To evaluate each of these states, liposomes were prepared from either DPPC or POPC, which have a T_C of 41 ºC [161] and –2 ºC [162], respectively. Due to the stresses that electric fields cause on the lipid membrane, we hypothesized that lipid bilayers in the liquid crystalline state would be more prone to deformation, resulting in greater release.

Size may also contribute to release, as theoretical models show that the voltage potential across a lipid bilayer of a liposome in an electric field is proportional to the diameter of

the liposome [163]. Thus, under a constant electric field the potential to introduce permanent pores into the lipid bilayer becomes diminished with decreasing liposome size. Liposomes of different sizes were prepared using polycarbonate membranes of 0.1, 1, or 10 μm pore size during the extrusion process. Figure 4-5 shows the measured size distribution from DPPC and POPC liposomes using dynamic light scattering (DLS). POPC and DPPC liposomes prepared with 100 nm membranes resulted in a population of particles with a single peak and a mean size of 140 ± 40 nm and 130 ± 40 nm, respectively. Measurements following extrusion through 1 and 10 μm membranes demonstrated much broader distributions of liposome particles with multiple peaks present. For 1 μm samples, the mean size was 2.3 ± 1.3 μm for POPC liposomes and 1.8 ± 0.9 μm for DPPC liposomes, while 10 μm samples had a mean size of 2.8 ± 1.3 μm and 3.0 ± 1.6 μm for POPC and DPPC liposomes, respectively. This broader distribution with larger membrane pore size has been observed in the literature [164], but could be improved by further refinement of the procedure or downstream fractionation with size exclusion chromatography. While there was a trend of increasing liposome size with increasing membrane pore size in Fig 4-5, the characterization of liposomes following extrusion through 10 μm membranes yielded particles much smaller than expected. Size distribution with DLS is determined by the fluctuations in scattered light intensity coming from the diffusion of particles in solution [165]. With larger particles, sedimentation due to gravity is more likely and can lead to inaccurate size characterization by DLS. Alternative strategies to measure liposome strategies that do not depend on diffusion, such as static light scattering and/or optical particle sizing will need to be explored.

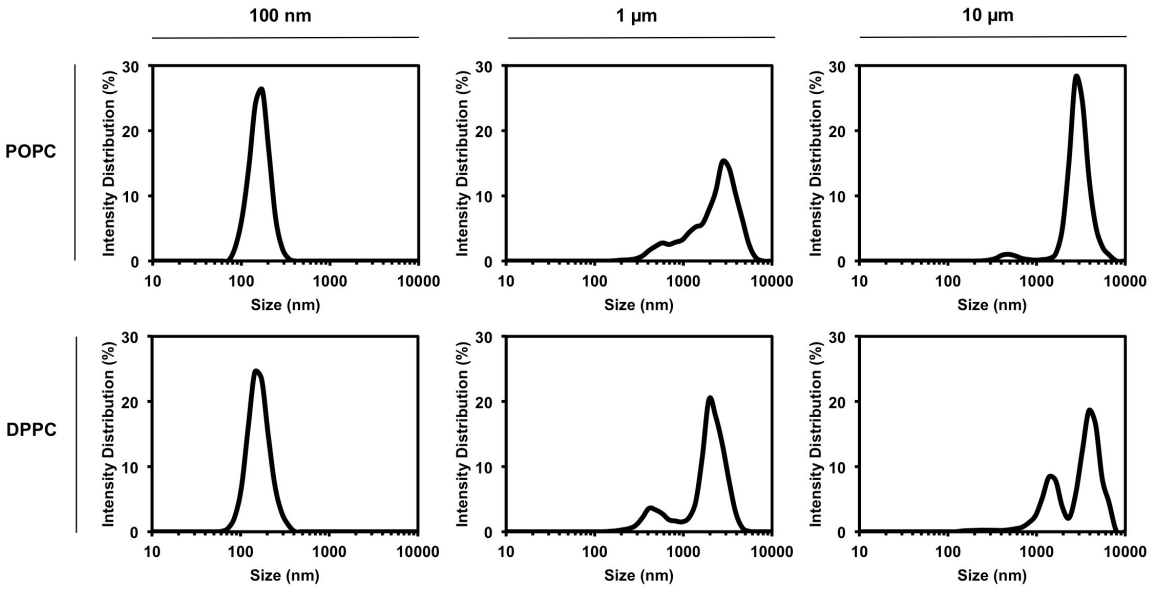

Figure 4-5. Liposome size distribution. Signal intensity size distribution measured by DLS of POPC (top) and DPPC (bottom) liposomes. Liposomes were extruded through either a 100 nm (left), 1 µm (center), or 10 µm (right) polycarbonate filter.

Release following electroporation from 90 mM carboxyfluorescein-loaded DPPC and POPC liposomes of various sizes was then evaluated *in vitro*. Liposome solutions were placed in an electrocuvette and connected to an electrical pulse generator to provide a homogeneous electric field throughout the solution during electroporation. Percent release following electroporation (Fig. 4-6) was quantified by the difference in release from untreated controls and liposome samples treated with detergent for complete carboxyfluorescein release through membrane disruption. DPPC liposomes showed a general trend of greater release with increases in electric field strength and membrane pore size, with the greatest percent release of 22 ± 6% achieved at 2000 $V \cdot cm^{-1}$ from DPPC liposomes prepared from membranes with a 10 µm pore size. These trends agree with theoretical predictions that the voltage potential across the membrane is directly proportionally with liposome size and applied electric field strength [163]. The increase

in transmembrane voltage potential can then result in membrane instability and pore formation, leading to carboxyfluorescein release. Due to the importance of liposome size, better characterization of the size distribution of DPPC liposomes following extrusion through 10 µm membranes could provide a better understanding of the size threshold needed for release. Purification of this population could lead to an increase in total release from IRE.

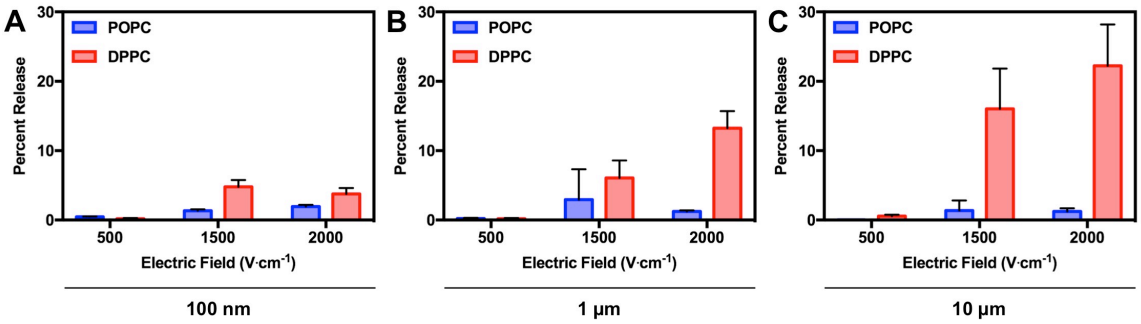

Figure 4-6. Inducible release from liposomes following electroporation. (A-C) Percent release of carboxyfluorescein from POPC (blue) and DPPC (red) liposomes following electroporation with 99 pulses at 100 µm pulse duration at 1 Hz at either 500, 1500, or 2000 V·cm^{-1} on 100 nm (A), 1 µm (B), and 10 µm (C) liposome preparations. 100% total release was determined from detergent-mediated liposome disassembly and untreated samples were used as 0% release controls. Percent release is mean ± SD, n = 3.

POPC liposomes, however, demonstrated less than 5% release, independent of applied condition or preparation. It was hypothesized that the POPC lipid bilayer would be more susceptible to pore formation due to the more fluid bilayer in comparison to the more rigid DPPC bilayer at room temperature. The difference in electrical properties, however, between the two transition states rather than the mechanical properties may have had the more important effect on carboxyfluorescein release. A study on DPPC lipid bilayers showed that the transmembrane voltage potential threshold for membrane instability increases by about 70% when the bilayer transitions from a gel state to a liquid crystalline

state [166]. This may be partly due to the observed increase in the membrane capacitance [166], which theoretical models predict that will decrease the voltage potential across the lipid bilayer [167]. Thus, the liquid crystalline state in membrane of POPC liposomes may have the reduced the transmembrane potential enough to reduce pore formation, even at elevated electric fields and liposome size.

A study by Yi et al. investigated percent release of carboxyfluorescein from 200 nm liposomes in which the bilayer is in a liquid crystalline state at room temperature following electroporation [157]. They observed similar low amounts of release, ≤ 10%, with a weak dependence on electric field strength. Although better size characterization is needed to confirm that the POPC liposomes extruded from 10 μm membranes are larger than the samples prepared from 1 μm liposomes, the observed release of carboxyfluorescein from electroporation in this study may provide better insight into how size, electric field strength, and the thermodynamic state of the lipid bilayer affect total release. While many studies have shown that electroporation may be used to induce pores in liposomes for drug release, few have quantified the amount of content released, which may affect efficacy.

4.4 Conclusions

The purpose of this study was to evaluate systems for IRE-induced molecule release that can be coupled to polymer scaffolds. Due to the lack of functional chemical groups in PCL for conjugation of biomolecules, PCL scaffolds were modified through an aminolysis reaction to introduce primary amines to the surface. Through this change,

covalent linkage of streptavidin could be utilized in the future to couple biotin labeled drug carriers to the scaffold due to the strong affinity between streptavidin and biotin. Biotinylated liposomes were prepared as drug carriers due to their common use in drug delivery and potential for inducible release through electroporation. Liposomes comprised of either DPPC and POPC were prepared using membranes with varying pore size to achieve liposomes of different sizes as characterized by DLS. Percent release following electroporation at varying electric field strengths was quantified through a carboxyfluorescein release assay. Release from DPPC liposomes increased with liposome size and electric field strength while POPC liposomes showed minimal release independent of condition. The largest observed percent release of 22 ± 6% came from DPPC liposomes, which to our knowledge, is higher than what has been reported in the literature. Through this study, a greater understanding of how liposomal release through electroporation may be achieved by varying size, composition, and electric field strength as well as how these drug carriers may be integrated with polymer scaffolds capable of recruiting cancer cells was developed.

Chapter 5: Integration of tumor cell-capturing polymer scaffolds into mouse models of melanoma

5.1 Introduction

Recruitment of breast cancer cells to PCL scaffolds is mediated by the local metastatic immune environment [39]. Since the immune system plays a role in metastasis of many cancers, these scaffolds could potentially be used to recruit other types of tumor cells, such as melanoma cells. Similar to observations in breast cancer patients [168, 169], elevated levels of myeloid derived suppressor cells in the peripheral blood of melanoma patients are correlated with advanced disease [170, 171]. Interestingly, these myeloid derived suppressor cells also facilitate recruitment to both metastatic organs and polymer scaffolds in breast cancer [39]. The high cytotoxic T lymphocyte infiltration in the melanoma tumor microenvironment led to the discovery of tumor-specific cytotoxic T cells and their associated melanoma-specific antigens, such as MART-1 [172, 173], gp100 [174], and TRP-2 [118]. While these antigens are well-characterized, the vast majority of cancers lack well-defined tumor-antigens and often specific antigens vary from patient to patient [175]. As a consequence, melanoma is a prime model for monitoring an immune response [176] and can be used as a proof of principle model to evaluate optimal treatment conditions that lead to effective anti-tumor immunity, which may translate to cancers with undefined antigens.

Recruitment of disseminated melanoma cells has previously been performed with other implantable devices [30, 38], and the recruitment of tumor cells has been shown to correlate with increased overall survival [38], which was also observed for studies using

PCL scaffolds to recruit disseminated breast cancer cells [41]. Thus, PCL scaffolds incorporated into mouse models of melanoma could be used as a platform to track immune response following focal ablation of disseminating tumor cells. Accordingly, Chapter 5 will investigate experimental and spontaneous metastasis, as described in Section 1.3, and direct seeding approaches to introduce melanoma cells to PCL scaffolds.

5.2 Materials and methods

Scaffold fabrication

To fabricate polymer scaffolds, PCL and PLG microspheres were first prepared as previously described [39, 41]. Briefly, for PCL microspheres, a 6% (w/w) solution of PCL (DURECT; inherent viscosity = 0.65-0.85 $dL \cdot g^{-1}$) in dichloromethane was emulsified in a 10% (w/w) poly(vinyl alcohol) solution and homogenized at 10,000 rpm for 1 minute. For PLG microspheres, a 6% (w/w) solution of 75:25 PLG (DURECT; inherent viscosity = 0.55-0.75 $dL \cdot g^{-1}$) in dichloromethane was emulsified in a 1% (w/w) poly(vinyl alcohol) solution and homogenized at 7,000 rpm for 30 seconds. Microspheres were lyophilized for 48 hours and then mixed with sieved sodium chloride particles (250-425 μm) in a 1:30 (w/w) ratio. Microsphere/sodium chloride mixtures were pressed to 3,300 lbs. for 45 seconds in a 5 mm steel die (Specac). PCL pressed disks were heated at 60 ºC for 5 minutes on each side and both types of polymer scaffolds were then foamed at 800 psig for ~24 hours, after which the gas was released at 17.5 CFH. Salt particles were removed by immersing disks in water for 90 minutes on a rocking platform. Polymer scaffolds were sterilized by soaking in 70% ethanol, followed by rinsing with sterile

water and drying on a sterile gauze pad. Scaffolds were then stored at -80 ºC until further use.

Scaffold implantation and tumor inoculation

Animal studies were performed in accordance with institutional guidelines and protocols approved by the University of Minnesota Institutional Animal Care and Use Committee (IACUC). Female C57BL/6 mice were purchased from The Jackson Laboratory, and mice were 7-15 weeks of age at the time of surgery. Two scaffolds were implanted into the subcutaneous space of the upper dorsal region per mouse. For intraperitoneal injection of B16-F10-TFP cells, two days after scaffold implantation, 5E6 B16-F10-TFP cells in 200 μL of PBS were injected into the intraperitoneal cavity, and scaffolds were harvested at 2 and 42 days following inoculation. For intravenous injection of B16-TFP cells, three weeks after scaffold implantation, 5E5 B16-F10-TFP cells in 200 μL of PBS were injected through the tail vein, and scaffolds were harvested at 10, 14, and 20 days following inoculation. For the orthotopic spontaneous metastasis model, 4-6 weeks after scaffold implantation, 5E4 B16-BL6 cells were injected intradermally into either the right flank or the dorsal side of the left ear in 50 μL and 15 μL of PBS, respectively. Primary tumors were excised when they reached ~5 mm x ~5 mm size, which occurred after 11-15 days for flank inoculation and 15-29 days for ear inoculation. Scaffolds were resected 4-5 weeks post-tumor inoculation for both groups. For tumor-free controls, mice received inoculations of PBS without cancer cells.

Flow cytometry

Mice were euthanized and scaffolds were retrieved, minced with microscissors in a 0.38 $mg \cdot mL^{-1}$ solution of Liberase TL (Roche Applied Science) in Hank's balanced salt solution (ThermoFisher Scientific) and placed at 37 °C for 20 min. Liberase was neutralized with 0.125 M EDTA (ThermoFisher Scientific), and cells were isolated by passing the digested tissue through a 70 mm filter (BD Biosciences) and rinsing with FACS buffer, PBS containing 0.5% bovine serum albumin (MilliporeSigma) and 2 mM EDTA. For analysis of TFP-positive B16-F10 tumor cells, samples were resuspended in FACS buffer and analyzed using an LSR II flow cytometer (Becton Dickinson Immunocytometry Systems).

qRT-PCR analysis

To evaluate the lower detection limit for *TRP-2* in B16-F10 cells *in vitro*, B16-F10 (ATCC CRL-6475) and 4T1 (ATCC CRL-2539) cells were mixed together at various ratios, while keeping the total cell population at one million cells. Cells were then placed in RLT buffer (Qiagen) with 1% β-mercaptoethanol (MilliporeSigma) and homogenized using QIAshredder columns (Qiagen), following the manufacturer's instructions. Tumors, lungs, and scaffolds harvested for qRT-PCR analysis were immediately snap frozen in liquid nitrogen and stored at -80 ºC. For homogenization of tissues, samples were placed in RLT buffer with 1% β-mercaptoethanol and homogenized at 10,000 rpm for 20 seconds on ice. To minimize the risk of cross-contamination between samples, after homogenization of each sample, the homogenizer was washed with 3 rounds of Type 1 water, 2 rounds of 70% ethanol, and 2 rounds of 100% ethanol, followed by a

wash with ELIMINase (ThermoFisher Scientific) and then 4 rounds of Type 1 water washes before running the next sample. For all samples, total RNA extraction was then performed using the RNeasy Mini Kit (Qiagen) following the manufacturer's instructions. cDNA synthesis was performed with 1 μg of total RNA for each sample using the Omniscript RT Kit (Qiagen). RT-PCR reactions were performed with 0.5 μL of cDNA, GoTaq Green Master Mix (Promega), and the gene-specific forward primer (250 nM) and reverse primer (250 nM), and reactions were run for 30 cycles and separated using a 2% agarose gel at 100 V for 30 minutes. qRT-PCR reactions were performed with 1 μL of cDNA, iTaq Universal SYBR Green Supermix (BioRad), and the gene-specific forward primer (250 nM) and reverse primer (250 nM). qRT-PCR analysis was performed using a CFX Connect Real-Time PCR Detection System (BioRad). Primers for *GAPDH* [90] and *TRP-2* [97] were obtained from the literature and are summarized in Table 5-1. For each sample, relative expression of *TRP-2* to reference gene *GAPDH*, $Ct_{TRP\text{-}2} - Ct_{GAPDH}$, was obtained before fold change calculations were performed.

Table 5-1. Primer sequences used for qRT-PCR analysis.

Gene	**Forward (5'-3')**	**Reverse (5'-3')**
GAPDH	CAATGTGTCCGTCGTGGA	GATGCCTGCTTCACCACC
TRP-2	TTAGGTCCAGGACGCCCC	CTGTGCCACGTGACAAAGGC

Seeding scaffolds with melanoma cells

For direct seeding of melanoma cells, luciferase-expressing B16-F10 cells (B16-F10-Luc) melanoma cancer cells were suspended in 5 $mg \cdot mL^{-1}$ Matrigel (Corning) at 20E6 cells per mL. To load cell solution within the hydrophobic pores of the polymer scaffolds, PCL scaffolds were submerged in 70% ethanol and then two rounds of culture media.

Scaffolds were then partially dried on gauze pads for 5 minutes each side and 20 μL of B16-F10-Luc suspension in Matrigel was then loaded into each scaffold followed by a 5 minute incubation at 37 ºC prior to subcutaneous implantation.

Tissue sectioning and histological analysis

For histological analysis, Matrigel only and B16-F10-Luc loaded scaffolds were removed whole from the subcutaneous space 11 days post-implantation. Tissues were fixed in 10% buffered formalin, embedded in paraffin, and sectioned at 4 μm using an HM 315 microtome (Microm). Slides were stained with hematoxylin and eosin (H&E) for histological analysis. Slides were imaged using an EVOS FL Auto Microscope (Thermo Fisher Scientific).

Bioluminescence imaging

Ten minutes before imaging, mice were injected in the intraperitoneal cavity with 15 $mg \cdot ml^{-1}$ of D-luciferin (Gold Biotechnology) in PBS at 75 $mg \cdot kg^{-1}$ body mass. For whole-animal imaging, mice were anesthetized with inhaled isoflurane and *in vivo* luciferase expression was evaluated using the IVIS 100 Spectrum imaging system (Caliper Life Sciences).

Statistical analysis

Data are presented as the mean ± standard deviation (SD) or box and whisker plot when stated, and *p*-values were determined using an unpaired Student's *t*-test.

5.3 Results and discussion

5.3.1 Evaluation of PCL scaffolds in B16-F10 experimental metastasis model

Recruitment of B16-F10 melanoma to engineered materials in experimental metastasis models has been previously demonstrated [30, 38]. In one study, B16-F10 cells were introduced into circulation through an intraperitoneal injection, which results in metastasis to the liver, kidney, peritoneum, and spleen [177]. A solution of polymer microparticles was injected into the dorsal subcutaneous space, and after 1 to 3 days, B16-F10 cells were injected into the intraperitoneal cavity of C57BL/6 mice [38]. Recruitment of melanoma cells to the polymer microparticles was observed one day after tumor cell injection, and recruitment was associated with the local acute inflammatory response present at the microparticle injection site one to three days following implantation. To evaluate if PCL scaffolds could recruit B16-F10 cells under similar conditions, PCL scaffolds were implanted in the dorsal, subcutaneous space of mice, and after two days, teal fluorescent protein (TFP)-expressing B16-F10 cells (B16-F10-TFP) were inoculated into the intraperitoneal cavity. B16-F10-TFP cells were utilized because recruitment could be quantified via flow cytometry (Fig. 5-1B) in comparison to unlabeled B16-F10 cells (Fig. 5-1A). As shown in Fig. 5-1B, a significant portion of the cells have lost expression of TFP during routing culture, indicating that analysis of the number of TFP-positive cells within the scaffolds will likely lead to an undercounting of the actual number of melanoma cells.

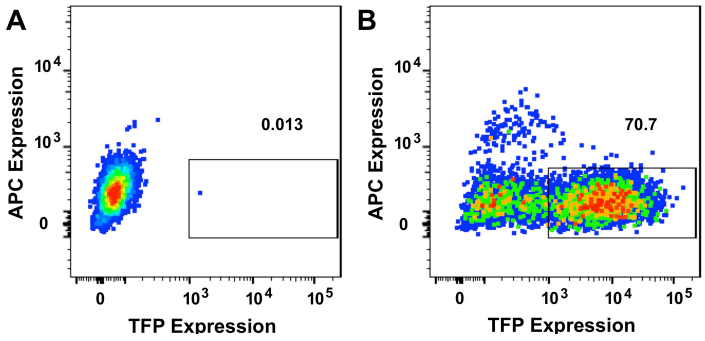

Figure 5-1. Fluorescence signature of TFP-labeled B16-F10 cells. (A, B) Representative flow cytometry data of cultured B16-F10 (A) and B16-F10-TFP (B) cells. Box indicates TFP-positive cells, with percentage of total cells that are TFP-positive indicated above the box. As the TFP-labeled cells should not show fluorescence in the APC channel, APC expression is plotted against TFP expression to exclude false positives or auto-fluorescent cells.

Scaffolds from mice that received only saline injections (Fig. 5-2B) were used as a baseline to compare to mice with B16-F10-TFP inoculations (Fig. 5-2A). Following a short (2 days) and long (42 days) melanoma exposure, scaffolds were harvested to evaluate recruitment of B16 cells (Fig. 5-2C). Aside from one outlier (Day 2), there was no evidence of recruitment of B16-F10-TFP cells to PCL scaffolds in this model. Although there was observable metastasis to the draining lymph node, no visible metastasis outside the peritoneum, such as the lung, was recorded (data not shown), as also seen by Fu et al. following IP inoculation of B16-F10 cells [177]. Given the lack of metastasis outside the peritoneal cavity and the inability to detect tumor cells in the scaffold, an alternative experimental metastasis model employing tail vein inoculation was evaluated for metastasis to PCL scaffolds, as this route of injection results in lung metastasis [177].

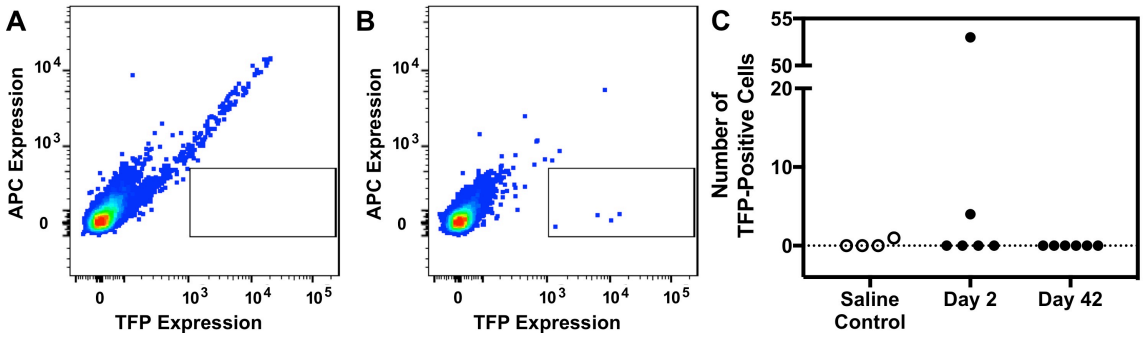

Figure 5-2. Flow cytometry to quantify number of B16-F10-TFP cells recruited to implanted PCL scaffolds. (A, B) Flow cytometry analysis of cells isolated from PCL scaffold two days after intraperitoneal injection of saline (A) or B16-F10-TFP cells (B). Box indicates TFP-positive cells. (C) Number of TFP-positive cells from PCL scaffolds after 2 and 42 days post intraperitoneal injection of B16-F10-TFP cells. Each data point represents an individual scaffold.

In order to study recruitment of cells to scaffold without confounding effects of the transient dynamics of the acute inflammatory response following implantation of the scaffold, we sought to perform the tail vein injection of tumor cells after the onset of the chronic inflammation stage within the scaffold. Previous work has shown that immune cell population within the scaffold stabilizes after ~30 days post-implantation [41]. Thus, B16-F10-TFP cells were injected intravenously through the tail vein four weeks after scaffold implantation to allow for both onset of the chronic immune microenvironment as well as sufficient vascularization. Scaffolds were harvested at 10, 14, and 20 days post-inoculation, and the number of recruited B16-F10-TFP cells was evaluated with flow cytometry (Fig. 5-3). At Day 20, recruitment of B16-F10-TFP cells to PCL scaffolds was seen in multiple samples and visible macrometastases in the lung were observed (data not shown). Although the measured number of recruited cells is likely an underrepresentation because of TFP-negative cells present in B16-F10-TFP population, the number of cells recruited is likely too small for a robust immune response following focal therapy treatment. In addition, as this method is typically performed as a lung colonization assay,

the majority of injected cells are localized to the lungs, complicating efforts to attract more circulating cells to the scaffold. Intravenous injection downstream of the lungs, such as through the left ventricle of the heart, could be implemented in the future to reduce lung colonization. Seib et al. utilized an intracardiac injection to demonstrate metastasis of B16-F10 cells to a bone-mimicking silk scaffold [30], which could be investigated with PCL scaffolds.

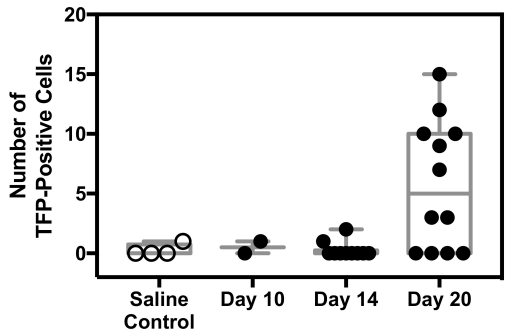

Figure 5-3. Recruitment of B16-F10-TFP cells to PCL scaffolds following intravenous injection. Box and whisker plot of number of TFP-positive cells isolated from PCL scaffolds 10, 14, and 20 days after intravenous injection of B16-F10-TFP cells.

The use of flow cytometry, however, may be underrepresenting the number of recruited cells, independent of TFP expression heterogeneity. Extraction of single cells from scaffolds for flow cytometry involves many wash and rinse steps, leading to significant loss of material, which impacts the ability to quantify rare cells. Moreover, the loss of TFP protein expression in culture as observed in Fig. 5-1B could be compounded by additional signal loss *in vivo* [178], further diminishing the ability to obtain an accurate count of the number of tumor cells recruited to the scaffold. Lastly, the use of an experimental metastasis model may be limiting the recruitment of disseminated cancer cells to PCL scaffolds, as recruitment to these scaffolds has been associated with local

immune cell population changes caused by the primary tumor, and there is no primary tumor in experimental metastasis models. Thus, we explored spontaneous metastasis models of melanoma to assess recruitment of metastatic melanoma cells to the scaffold in mice that had primary tumors.

5.3.2 Spontaneous metastasis model for recruitment of B16 cells to PCL scaffolds

In order to evaluate the presence of unlabeled B16-F10 melanoma cells in PCL scaffolds, a qRT-PCR assay previously used to quantify metastasis of melanoma cells to the lung was utilized [97]. This assay quantifies metastasis by comparing the expression of melanoma-specific genes, such as *TRP-2*, in samples from mice with and without inoculation of melanoma cells. Due to the lower amount of tumor cells that might be present at the scaffold, as opposed to a solid tumor, the first step was to evaluate the lower detection limit for melanoma cells in a cell suspension using this assay. Accordingly, expression of *TRP-2* in cell suspensions consisting of decreasing numbers of B16-F10 melanoma cells was analyzed using this qRT-PCR assay. To keep the total number of cells constant, 4T1 breast cancer cells were added to maintain the population number at 1 million cells. 4T1 cells were chosen because they are negative for *TRP-2* expression (Fig. 5-4A). The qRT-PCR data is plotted as fold change in *TRP-2* expression normalized to samples containing only 4T1 cells, with glyceraldehyde 3-phosphate dehydrogenase (*GAPDH*) serving as a reference gene. The results show an increase in *TRP-2* expression as the number of B16-F10 cells increases, and significant *TRP-2* expression compared to a population containing only 4T1 cells could be detected with as low as 10,000 B16-F10 cells, or 1% of total cell population (Fig. 5-4B).

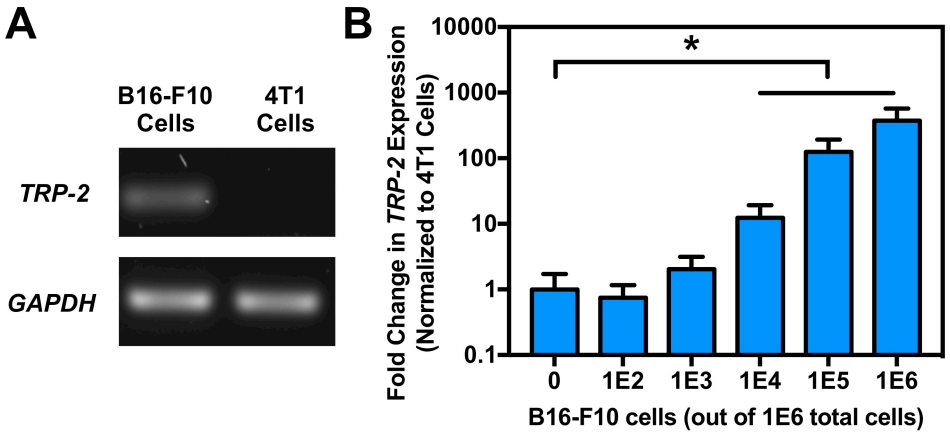

Figure 5-4. qRT-PCR assay to identify the presence of B16-F10 cells. (A) RT-PCR of B16-F10 melanoma and 4T1 breast cancer cells for melanoma-specific antigen *TRP-2*. *GAPDH* was used a housekeeping gene. (B) Fold change in *TRP-2* expression in samples of 1E6 total cells containing various ratios of B16-F10 and 4T1 cells. Fold change is normalized to 4T1 controls (zero B16-F10 cells). (*) $P < 0.05$ compared to 4T1 control samples. qRT-PCR data is mean ± SD, n = 4.

To validate that the qRT-PCR assay could detect unlabeled melanoma cells that have metastasized from the primary tumor *in vivo*, the B16-BL6 cell line was used, as it is a more metastatic variant derived from the B16-F10 cell line, and B16-F10 cells do not metastasize effectively in spontaneous tumor models [27]. B16-BL6 cells were inoculated through an intradermal injection on the right flank of C57BL/6 mice To prolong exposure to metastasizing tumor cells, the primary tumors were resected 11-15 days later, leaving behind only disseminated melanoma cells in the mouse, as if the primary tumor is not resected the study must be terminated much sooner due to the size of the tumor. After at least four weeks following tumor resection, lungs were harvested and inspected for any visible melanoma nodules originating from the primary tumor. Lungs with and without visible macrometastasis (VM+ and VM– lungs, respectively) were analyzed for *TRP-2* expression using the qRT-PCR assay (Fig. 5-5B). An example of a VM+ lung is shown in Fig. 5-5A). As expected, VM+ lungs had significantly greater

TRP-2 expression in comparison to naive lungs, but more importantly, Fig. 5-5 shows that the same is true for VM– lungs. These results demonstrate the capability of this qRT-PCR assay to detect disseminated melanoma cells regardless of whether metastases are visually evident. The qRT-PCR assay has only been previously applied to detect metastasis from a tail vein injection model [97], in which the number of circulating tumor cells would be much higher than that of a more physiologically relevant orthotopic spontaneous cancer model. This analysis highlights the use of qRT-PCR as an effective assay for sensitive detection of disseminated cells from an orthotopic primary tumor.

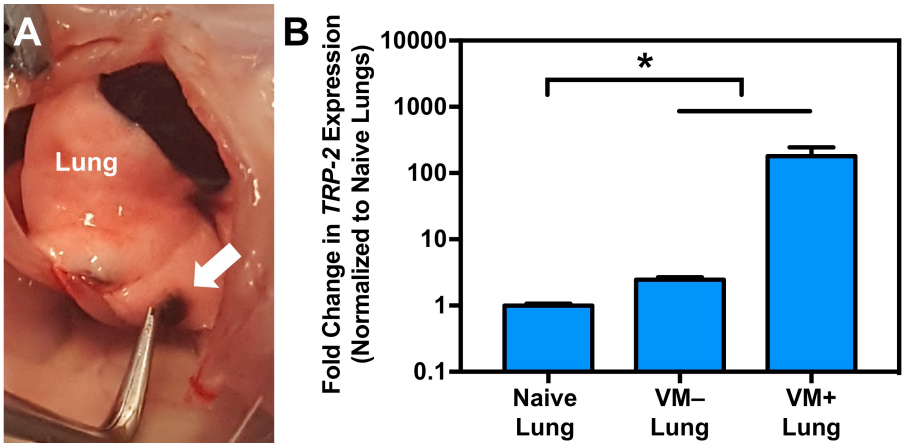

Figure 5-5. Detection of melanoma-specific gene expression in lungs from spontaneous metastasis model using qRT-PCR. (A) Picture of mouse lung with a visible macrometastasis nodule indicated by white arrow. (B) Fold change in *TRP-2* expression in lungs with, VM+, or without, VM–, visible macrometastases following intradermal inoculation of B16-BL6 cells in right flank. Fold change is normalized to naive lung controls (*) $P < 0.05$ compared to naive lungs. qRT-PCR data is mean ± SD, n = 2 for naive lung and n =4 for VM– and VM+ lungs.

The qRT-PCR assay was then applied for detection of melanoma cells that may have metastasized to PCL scaffolds. PCL scaffolds were implanted into the dorsal, subcutaneous space, and after at least four weeks, B16-BL6 cells were inoculated through an intradermal injection. Two independent injection sites, the flank and ear, were used

since the site of injection could impact routes of metastasis. Equal numbers of B16-BL6 cells were inoculated at each location, and primary tumors were resected once they reached ~5 mm by ~5 mm in size, which occurred at 11-15 and 15-29 days post-inoculation in the flank and ear, respectively. Apart from the differences in tumor growth, there was also variation in visible metastasis to the lungs and draining lymph nodes between the two orthotopic sites (Fig. 5-6A). Greater frequency of lung metastasis was seen in the flank model (32%) over the ear model (23%), but interestingly 31% of mice exhibited draining lymph node metastasis in the ear model, which was not observed in the flank model. PCL scaffolds were then harvested and analyzed for metastasis using the qRT-PCR assay (Fig. 5-6B). Fig. 5-6B shows that there is significantly greater *TRP*-2 expression in PCL scaffolds from flank B16-BL6 orthotopic inoculations relative to PCL scaffolds harvested from tumor-free mice, providing evidence that melanoma cancer cells metastasized to the scaffold. Alternative assays, such as histological analysis, would be needed to confirm these findings, but these results would be the first to demonstrate recruitment of melanoma cells to an engineered site from an orthotopic primary tumor.

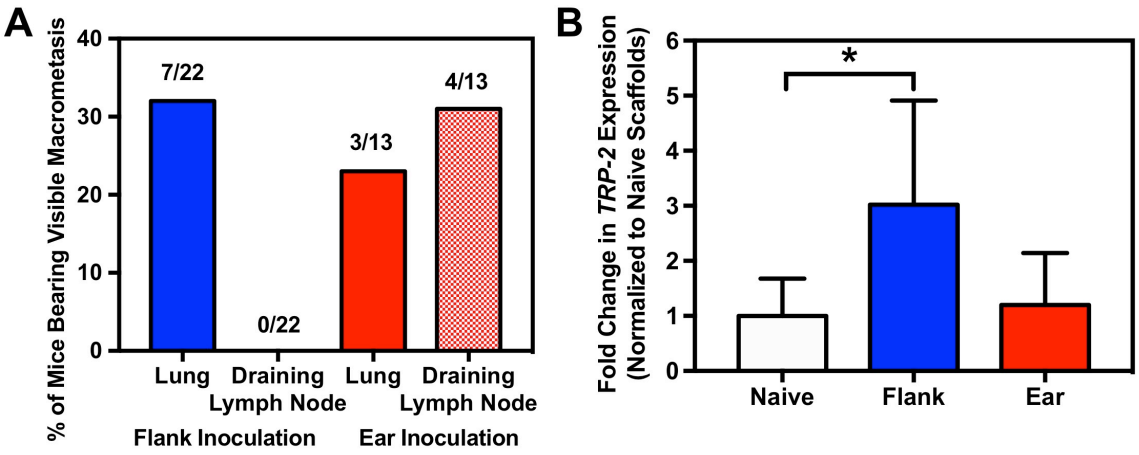

Figure 5-6. Evaluation of melanoma cell recruitment in a spontaneous orthotopic metastasis models. (A) Frequency of visible metastasis in the lungs and draining lymph nodes in mice following intradermal inoculation of B16-BL6 cells in right flank (blue) or left ear (red). (B) Fold change in *TRP-2* expression in scaffolds from mice following intradermal inoculation of B16-BL6 cells in right flank (blue) or left ear (red). Fold change is normalized to scaffolds from mice receiving saline inoculations as controls. (*) $P < 0.05$ compared to saline inoculation controls. qRT-PCR data is mean ± SD, n = 5 for naive scaffolds, n =13 for flank inoculations, and n = 14 for ear inoculations.

The differences in metastatic profile and recruitment of melanoma cells to the scaffold from flank and ear inoculations may provide insight into whether blood vessels or lymphatics are the primary route of metastasis to the scaffold, which remains unknown even in the context of breast cancer. The correlation between recruitment to the scaffold and increased visible lung metastasis from flank inoculations may imply that melanoma cells metastasize to the scaffold primarily through blood vessels. This is in agreement with the absence of melanoma recruitment to the scaffold from ear inoculations that resulted in draining lymph node metastasis, suggesting that lymphatics may not be the primary route of metastasis to the scaffold. Additionally, recruitment of melanoma cells to PCL scaffolds (Fig. 5-3) alongside lung metastasis was observed under tail vein injections. Furthermore, no visible lung metastasis and poor metastasis to PCL scaffold (Fig. 5-2C) was seen under intraperitoneal injections, but draining lymph node metastasis

was visibly detected. Altogether, studies that resulted in greater visible lung metastasis over draining lymph node metastasis also led to an increased frequency in recruitment of melanoma cells to PCL scaffolds. This may indicate that blood vessels are the primary route of metastasis to PCL scaffolds, but further studies will be needed to confirm these findings.

5.3.3 Direct seeding of B16-F10 cells in polymer scaffolds prior to implantation

Given the challenges in recruiting large numbers of melanoma cells to the scaffold, direct seeding of B16-F10 tumor cells in the scaffolds was explored as an alternative to enable proof-of-principle studies of combined focal ablation and immunomodulation of the scaffold site. PCL scaffolds were utilized for the studies described thus far due to their slower degradation rates in the body [179], which renders them appropriate for use in long-term studies. For shorter-term direct seeding studies, PLG scaffolds were also evaluated to determine which type of polymeric scaffold was more conducive to supporting tumor cell survival and growth. 4E5 luciferase-expressing B16-F10 melanoma cells (B16-F10-Luc) were suspended in Matrigel and loaded into either PCL or PLG scaffolds and implanted into the dorsal subcutaneous space in immunocompetent C57BL/6 mice. B16-F10-Luc cells were used for this study to enable whole-animal bioluminescence imaging to track tumor cell growth in the scaffold site throughout the study. After 11 days, scaffolds were harvested and analyzed by histology for the presence of B16-F10-Luc melanoma cells within the polymer scaffolds. H&E-stained sections of a primary tumor generated following an intradermal injection of B16-F10-Luc cells in the right flank shows the cellular morphology and staining profile of B16-F10-Luc cells *in*

vivo (Fig. 5-7), which exhibit typical malignant features, such as variability in size and shape of cytoplasm and nucleus, increased ratio of nucleus to cytoplasm, and prominent nucleoli [180]. After 11 days, Matrigel-loaded PCL scaffolds (Fig. 5-8A) show enhanced host cell infiltration in comparison to Matrigel-loaded PLG scaffolds (Fig 5-8B), which is consistent with previous observations [41]. However, when B16-F10-Luc cells are loaded into the scaffolds along with the Matrigel, the PLG scaffolds (Fig. 5-8D) demonstrate a greater presence of B16-F10-Luc cells than the PCL scaffolds (Fig. 5-8C) after 11 days.

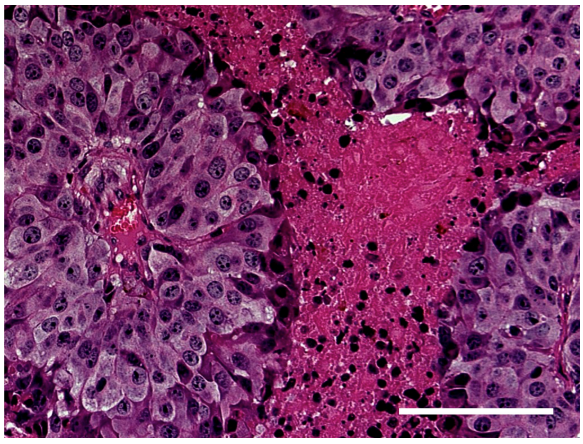

Figure 5-7. H&E staining of B16-F10-Luc primary tumor. Histological section of a B16-F10-Luc primary tumor stained with H&E to demonstrate typical tumor cell morphology and staining profile. Light pink areas denote areas of tumor necrosis, characteristic of growing tumors. Scale bar indicates 100 μm.

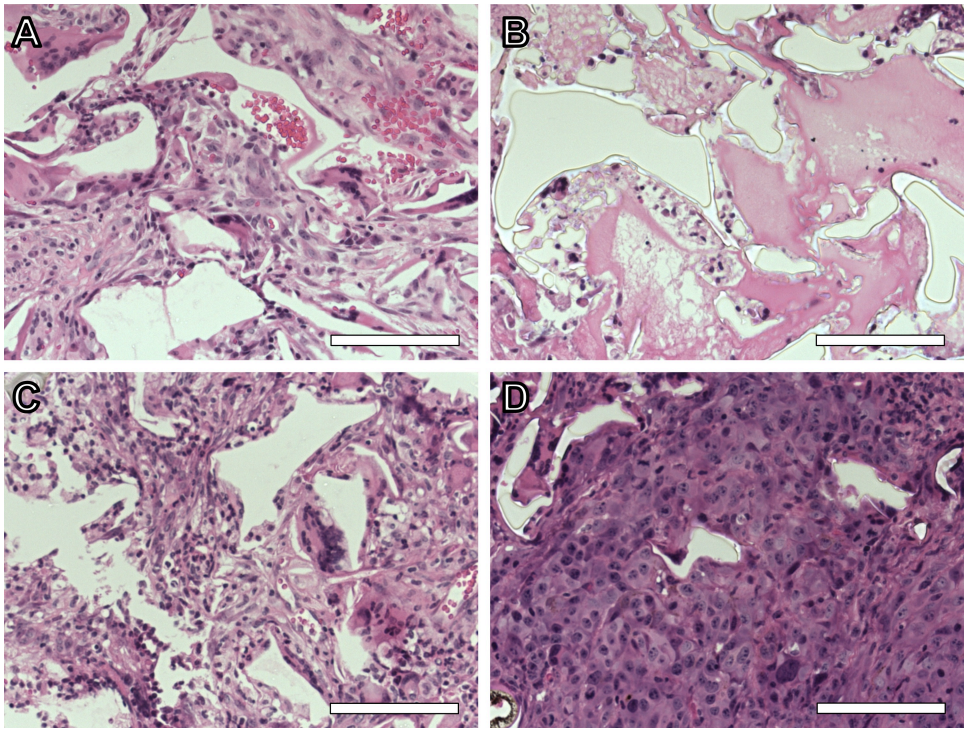

Figure 5-8. Matrigel-only and B16-F10-Luc melanoma cell loaded polymer scaffolds post implantation *in vivo*. (A-D) H&E stained sections of (A, B) Matrigel-only loaded PCL (A) and PLG (B) scaffolds and (C, D) B16-LUC loaded PCL (C) and PLG (D) scaffolds harvested after 11 days post-implantation in the dorsal, subcutaneous space in C57BL/6 mice. Scale bar indicates 50 μm.

Bioluminescence imaging was also used to track growth of B16-F10-Luc cells in real time. This imaging technique works by sensitive detection of light emitted by luciferase-mediated oxidation of luciferin, a molecular substrate [181]. The detection level for imaging can be as deep as several centimeters, so growth of luciferase expressing B16-F10-Luc cells within the scaffold can be measured *in vivo*. Greater signal intensity from implanted PCL (Fig. 5-9A) and PLG scaffolds (Fig. 5-9B) loaded with B16-F10-Luc cells is evident after seven days post-implantation in comparison to Matrigel-only controls. Images show that the B16-F10-Luc growth is localized within the scaffold region for both PCL and PLG scaffolds. Signal intensity was tracked over time (Fig. 5-

9C) and as reflected by the histological results, more growth of B16-F10-Luc cells was observed in PLG scaffolds compared to PCL scaffolds.

The contrast in cell infiltration and B16-F10-Luc presence might be explained by the differences in chemical composition of the two scaffolds. PCL and PLG are polyesters that degrade by hydrolysis, and differences in their degradation rate are dependent on their hydrophilicity. PCL is more hydrophobic than PLG, resulting in PLG degrading about 4-6x faster than PCL [179]. The byproducts of degradation are acidic molecules that can lower the pH of the local microenvironment, with the degradation products of PLG, lactic acid (pKa 3.08) and glycolic acid (pKa 3.83), being stronger acids than that of PCL, caproic acid (pKa 4.84) [182]. The combination of faster degradation and stronger acidic byproducts in PLG over PCL may have lead to toxic conditions for healthy cell infiltration in PLG scaffolds as seen in Fig. 5-8A-B. These results correlate with previous studies [41] and also by Sung et al. following subcutaneous implantation of PCL or PLG scaffolds [183]. An acidic microenvironment, however, may not necessarily be an inhibitor for B16-F10-Luc growth, as tumor microenvironments are commonly acidic [184]. Greater growth of B16-F10-Luc cells in PLG scaffolds may also be attributed to the more hydrophilic surfaces, which is favorable for cellular adhesion [185]. Hydrophilicity may affect cellular attachment by affecting how extracellular matrix proteins, such as fibronectin, adsorb to the polymer surface, which plays an important role in cellular attachment to solid substrates [186].

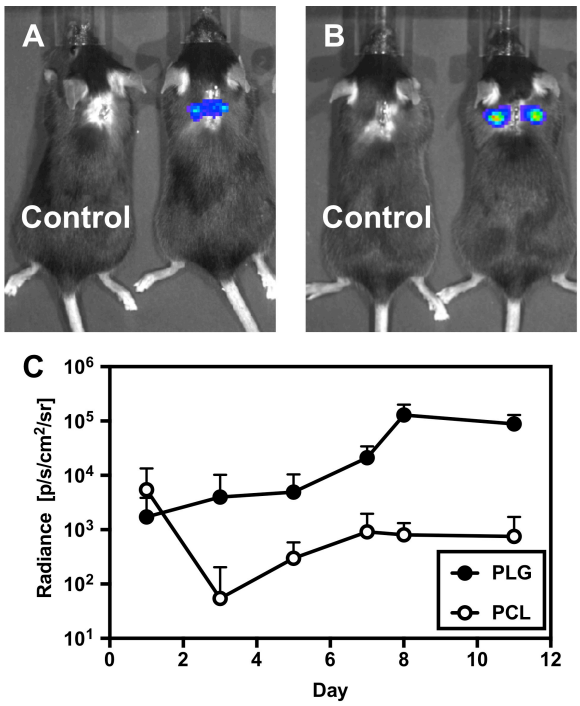

Figure 5-9. Tracking growth of B16-F10-Luc cells in polymer scaffolds *in vivo*. (A, B) Bioluminescence imaging of mice at day 7 post subcutaneous implantation of PCL (A) and PLG (B) scaffolds loaded with either Matrigel-only control (left) or luciferase-expressing B16-F10 cells (right). (C) Radiance intensity from B16-F10-Luc loaded scaffolds over time. Radiance data is mean ± SD, n ≥ 6.

These results show that both PLG and PCL scaffolds could be used to locally maintain B16-F10-Luc melanoma cells *in vivo* following direct seeding, with PLG scaffold promoting better growth than PCL scaffolds. Previous reports have shown that other cancer cell recruiting scaffolds have been used to support cancer cells upon direct seeding *in vivo*, such as PC-3 prostate cancer cells in bone-mimicking, silk scaffolds [30]. This method of direct seeding of melanoma cells, however, does not reflect any stages in the metastatic process, and a spontaneous metastasis model would better represent metastasis of melanoma cells to the polymer scaffold. Nevertheless, directly seeding scaffolds with B16-F10 melanoma cells could be useful as a proof of principle to release tumor antigens from the scaffold following focal therapy and track the resulting immune response.

5.4 Conclusions

Melanoma's well-characterized antigens, such as TRP-2, make this cancer an ideal model to understand how anti-tumor immunity could be achieved following focal ablation of disseminating cells. In this chapter, microporous polymer scaffolds previously shown to recruit metastatic breast cancer cells [39] were evaluated for the ability to recruit melanoma cells, ultimately to track an immune response following focal therapy in future studies. Flow cytometric analysis of cells isolated from polymer scaffolds showed recruitment of fluorescently labeled B16-F10-TFP cells after 20 days following intravenous inoculation. Additionally, the recruitment of metastatic cells in a more clinically relevant orthotopic spontaneous metastasis model was evaluated using unlabeled B16-BL6 cells, a more metastatic variant of the B16-F10 line. A qRT-PCR assay previously used to quantify metastasis to the lung [97] was applied to polymer scaffolds to detect unlabeled melanoma cells both *in vitro* and from *ex vivo* samples. Analyzing relative gene expression of melanoma-specific *TRP-2* through qRT-PCR provided evidence of recruitment to PCL scaffolds following intradermal inoculation in the flank. Aside from using metastatic models to isolate melanoma cells *in vivo*, PLG scaffolds supported growth of melanoma cells *in vivo* after being loaded directly into the scaffolds prior to subcutaneous implantation. This study demonstrates the ability of polymer scaffolds to be used as a system to recruit or support growth of metastatic melanoma cells, which in the future may be used to track an immune response following focal therapy.

Chapter 6: Conclusions and future directions

6.1 General conclusions

The aim of this project was to improve the therapeutic potential of microporous polymer scaffolds capable of recruiting metastatic breast cancer cells *in vivo*. Initial work focused on introducing focal therapy ablation, such as focal hyperthermia, to target metastatic cells that may be recruited to the polymer scaffold. This was first accomplished by modifying PCL scaffold to include an aluminum disk in the center for non-invasive induction heating through an alternating magnetic field. Heat generation could be controlled by the size of the disk, magnetic field strength, and type of metal. After subcutaneous implantation, these PCL-Al composite scaffolds were biocompatible and integrated properly with the host tissue, while maintaining the capacity to recruit murine breast cancer cells. *In vivo* induction heating of implanted PCL-Al scaffolds resulted in effective killing of host cells within the scaffold.

The release of tumor specific antigens from the scaffold due to the ablation of tumor cells could potentially be utilized to induce an immune response to kill remaining cancer cells systemically. Thus, the combination of immunotherapy following focal ablation of disseminated cancers could further improve the beneficial effects of the polymer scaffold. Using well-characterized melanoma-specific antigens of the B16 cancer model to track *in vitro* T cell activation, collaborative work with the Shimizu and Bischof groups demonstrated that tumor lysates generated from IRE generated the greatest T cell activation compared to heat and cryogenic ablation. As a consequence, application of IRE within polymer scaffolds was studied. PCL scaffolds were modified to include metal

mesh electrodes (termed PCL-IRE scaffolds) to provide a more uniform electric field distribution than traditional two-probe geometry. B16 cells loaded into these PCL-IRE scaffolds were killed upon *in vitro* IRE treatment, demonstrating their efficacy for facilitating IRE application against melanoma cells. Composite PCL-IRE scaffolds integrated properly with tissue post-implantation and were capable of complete ablation of infiltrating cells within the scaffold *in vivo*.

Electroporation of the scaffold could in theory also be utilized to induce release of immunoadjuvants from drug-loaded carriers attached to the scaffold in order to enhance the local immune response to the tumor antigens released upon ablation. To this end, PCL scaffolds were chemically modified with primary amines to facilitate streptavidin conjugation, enabling binding of biotin-labeled liposomes to the scaffold. *In vitro* release studies of liposomes in suspension following IRE treatment demonstrated that release could be tuned by electric field strength and liposome formulation and size.

Finally, polymer scaffolds were evaluated for recruitment of melanoma cells *in vivo*, using both experimental and spontaneous metastasis models. In experimental metastasis models using the B16-F10 cell line, recruitment of tumor cells to the scaffold was seen upon tail vein injection of tumor cells but not intraperitoneal injection. A more metastatic variant, B16-BL6, was used to study metastasis from an orthotopic injection at either the lower flank or the ear. Using a qRT-PCR assay to quantify metastasis to implanted scaffolds, recruitment of melanoma cells was observed under flank inoculations. An increased presence of draining lymph node metastasis in intraperitoneal injections and ear

inoculations in contrast to more observable metastasis to the lungs from tail vein injections and flank inoculations may indicate that route of metastasis to the scaffold is predominantly through blood vessels as opposed to lymphatics. While the scaffolds are capable of recruiting metastasizing melanoma cells, should proof-of-principle studies of combined focal ablation and local immunomodulation of the scaffold site require larger numbers of tumor cells present at the site, B16 cells may be directly seeded into polymer scaffolds and maintain viability after 10 days post subcutaneous implantation. This project has shown that polymer scaffolds may be modified for focal therapy applications and are capable of recruiting metastatic melanoma cells, while providing many opportunities for further investigation.

6.2 Future directions

6.2.1 Sublethal hyperthermia for inducible release within PCL-IRE scaffolds

In Chapter 4, IRE inducible release from polymer scaffolds using liposomes was explored. Although some release was observed from liposomes under IRE, the effectiveness may be a limited by diminishing effects of electroporation on vesicles of smaller size [163]. However, the use of heat has been successfully utilized to induce release within certain liposomal formulations [128]. These thermosensitive liposomes could be designed to release their cargo in the range of 40-42 ºC, which above body temperature but below a therapeutic threshold to kill cells [128]. As described in Chapter 3, *in vitro* T cell activation studies have shown that melanoma cell lysates produced by IRE caused the greatest T cell activation in comparison to heat and cryogenic ablation. While heat may not be the optimal method for cell lysis to release tumor antigen, the

application of lower levels of heating to release immune adjuvants from thermosensitive liposomes prior to or after IRE treatment could enhance downstream immune activation. Immune adjuvants such as anti-CD40 antibody [187], unmethylated CpG oligodeoxynucleotides [188], and OK-432 [189] could be investigated as they have all been previously used in conjunction with focal therapy to improve outcomes *in vivo*.

As shown in Chapter 2, a conducting material, such as an aluminum disk, could be used a heat source under an alternating magnetic field. The stainless steel metal mesh electrodes incorporated into PCL-IRE scaffolds for generation of a semi-uniform electric field in Chapter 3 could also serve a source of heat under electromagnetic induction. Although the temperature rise can be controlled by the applied magnetic field strength and frequency for a fixed electrode geometry and size, the difficulty in monitoring temperature levels to be sufficient for liposome release but below the threshold for cell damage may be impractical. Alternatively, the use of magnetic metals with a Curie temperature at 42 ºC could self-regulate heating rate without temperature monitoring [190]. While non-magnetic metals, such as aluminum, generate heat through eddy currents under electromagnetic induction, magnetic metals generate additional heat from the internal friction between magnetic domains during the rapid reversals in magnetization [191]. Above the Curie temperature, magnetic materials become nonmagnetic causing heat generation to drop significantly [190]. Magnetic metals such as manganese arsenide, MnAs, have a desired Curie temperature of 42 ºC [192], which could serve to provide heating to temperatures appropriate for liposome release but insufficient for cellular damage.

The use of a non-uniformly distributed heat source, however, results in temperature gradients throughout the scaffold. These temperature gradients may cause regions of low temperatures insufficient for liposome release. The use of a more dispersed heat source could also be explored to generate a more homogeneous temperature distribution, ensuring liposome release throughout the entire scaffold. This could be accomplished by encapsulating magnetic nanoparticles into PCL microparticles prior to fabricating scaffold by using a double emulsion technique previously used to encapsulate macromolecules such as DNA [193], proteins [194], and viruses [195]. Under an alternating magnetic field, magnetic nanoparticles generate heat by the dynamically changing internal magnetic moments and by the particle oscillations in the suspended medium [196]. Most common forms of magnetic nanoparticles for induced heating are composed of iron oxides magnetite, Fe_3O_4, and maghemite, γ-Fe_2O_3, which have been applied in the clinic to treat glioblastoma multiforme through an intratumoral injection [197]. These iron oxide nanoparticles have also been embedded in PCL scaffolds for homogeneous heat generation [85, 86]. Although these iron oxide nanoparticles were useful for focal hyperthermia, the Curie temperature of magnetite, 580 ºC [198], and maghemite, 600 ºC [199], would not allow for a controlled temperature rate below therapeutic temperatures. Alternative materials, such as Ba_2FeReO_6 [200] and $Me_{1-x}Zn_xFe_2O_4$ (x= 0.4-0.5; Me = Ni, Cu, Co, Mn) [201] nanoparticles, have been discovered with a Curie temperature of 42 ºC and could be used as self-regulating magnetic nanoparticles for homogeneous liposome release within the scaffold. The use of sublethal hyperthermia for inducible release of immune adjuvants from thermosensitive liposomes,

in combination with IRE therapy, may improve downstream immune action following treatment of disseminated cancer cells.

6.2.2 Investigating primary route of metastasis to PCL scaffolds

PCL scaffolds capable of recruiting 4T1 breast cancer cells [41] were investigated in Chapter 5 for capture of B16-BL6 melanoma cells. In the B16-BL6 model, differences in metastatic profile were observed depending on the orthotopic inoculation site of either the flank or ear. Flank inoculations led to observations of visible lung metastasis with no visible draining lymph node metastasis, while draining lymph node metastasis was more prevalent than lung metastasis under ear inoculations. Recruitment of B16-BL6 cells to the scaffold was observed from the flank inoculations and not the ear, suggesting that recruitment of B16 metastatic cells to the scaffold may be primarily through blood vessels and not through the lymphatics. As the route of metastasis of PCL scaffolds remains an unanswered question, even in the context of breast cancer, these observations in the melanoma model enable further investigations to provide deeper insight into whether the blood or lymph vessels are the primary route of metastasis to PCL scaffolds.

To accomplish this, PCL scaffolds loaded with either angiogenic factors, such as FGF or VEGF-A, or lymphangiogenic factors, such as VEGF-C or VEGF-D, [202] could be used to compare recruitment to regular PCL scaffolds. The local release of these factors could increase the local density of either blood or lymph vessels within the scaffold. Increases in blood [203] and lymph [204] vessel density have been correlated with greater metastasis in human patients. Validation of local increase in blood or lymph vessel

density can be quantified with immunological staining of PAL-E or LYVE-1, respectively [205], in loaded PCL scaffolds post-implantation. Next, 4T1 breast and B16-BL6 melanoma orthotopic tumor models could be utilized to determine differences in recruitment between angiogenic, lymphangiogenic, and regular scaffolds and to see whether the findings are specific to a each type of cancer. This study may provide a greater understanding of the primary route of metastasis to PCL scaffolds and thus may predict how best to utilize the scaffolds clinically.

6.2.3 Downstream immune response following IRE of B16 cells in PLG scaffolds

In Chapter 5, B16-F10 cells were directly seeded onto PLG scaffolds and implanted subcutaneously, as a proof-of-concept of presenting B16-F10 cells in the scaffolds for focal therapy. To study potential downstream immune activation from targeting disseminated cells, changes in endogenous levels and activation of TRP-2 specific T cells before and after IRE could be analyzed by flow cytometry. An increase in TRP-2 specific T cell levels may not be sufficient for anti-melanoma immunity [206]; thus, a secondary challenge of B16-F10 cells will be given to observe differences in tumor growth following the focal therapy. As it is likely that smaller numbers of tumor cells will be present in the scaffold as a result of metastasis, a titration of seeded B16-F10 cells could be utilized to determine how the quantity of tumor cells may affect immune response and to identify conditions that can produce the most robust response at low tumor cell numbers. The use of immune checkpoint blockade inhibitors, such as anti-PD-1 monoclonal antibody, could be implemented to improve intended outcomes.

Bibliography

[1] American Cancer Society, Breast Cancer Facts & Figures 2017-2018, Atlanta: American Cancer Society, 2018.
[2] P. Mehlen, A. Puisieux, Metastasis: a question of life or death, Nature Reviews Cancer 6(6) (2006) 449-458.
[3] American Cancer Society, Cancer Facts & Figures 2017, Atlanta: American Cancer Society, 2017.
[4] S. Karaman, M. Detmar, Mechanisms of lymphatic metastasis, Journal of Clinical Investigation 124(3) (2014) 922-928.
[5] S.P.H. Chiang, R.M. Cabrera, J.E. Segall, Tumor cell intravasation, American Journal of Physiology-Cell Physiology 311(1) (2016) C1-C14.
[6] G. Méhes, A. Witt, E. Kubista, P.F. Ambros, Circulating breast cancer cells are frequently apoptic, American Journal of Pathology 159(1) (2001) 17-20.
[7] S. Meng, D. Tripathy, E.P. Frenkel, S. Shete, E.Z. Naftalis, J.F. Huth, P.D. Beitsch, M. Leitch, S. Hoover, D. Euhus, B. Haley, L. Morrison, T.P. Fleming, D. Herlyn, L.W.M.M. Terstappen, T. Fehm, T.F. Tucker, N. Lane, J. Wang, J.W. Uhr, Circulating tumor cells in patients with breast cancer dormancy, Clinical Cancer Research 10(24) (2004) 8152-8162.
[8] L.W.M.M. Terstappen, C. Rao, S. Gross, V. Kotelnikov, E. Racilla, J. Uhr, A. Weiss, Flowcytometry - principles and feasibility in transfusion medicine. Enumeration of epithelial derived tumor cells in peripheral blood, Vox Sanguinis 74(Suppl. 2) (1998) 269-274.
[9] S. Nagrath, L.V. Sequist, S. Maheswaran, D.W. Bell, D. Irimia, L. Ulkus, M.R. Smith, E.L. Kwak, S. Digumarthy, A. Muzikansky, P. Ryan, U.J. Balis, R.G. Tompkins, D.A. Haber, M. Toner, Isolation of rare circulating tumour cells in cancer patients by microchip technology, Nature 450(7173) (2007) 1235-1239.
[10] R.T. Krivacic, A. Ladanyi, D.N. Curry, H.B. Hsieh, P. Kuhn, D.E. Bergsrud, J.F. Kepros, T. Barbera, M.Y. Ho, L.B. Chen, R.A. Lerner, R.H. Bruce, A rare-cell detector for cancer, Proceedings of the National Academy of Sciences of the United States of America 101(29) (2004) 10501-10504.
[11] S.-K. Kraeft, A. Ladanyi, K. Galiger, A. Herlitz, A.C. Sher, D.E. Bergsrud, G. Even, S. Brunelle, L. Harris, R. Salgia, T. Dahl, J. Kesterson, L.B. Chen, Reliable and sensitive identification of occult tumor cells using the improved rare event imaging system, Clinical Cancer Research 10(9) (2004) 3020-3028.
[12] E. Racila, D. Euhus, A.J. Weiss, C. Rao, J. McConnell, L.W.M.M. Terstappen, J.W. Uhr, Detection and characterization of carcinoma cells in the blood, Proceedings of the National Academy of Sciences of the United States of America 95(8) (1998) 4589-4594.
[13] J. Zhang, K. Chen, Z.H. Fan, Circulating tumor cell isolation and analysis, in: G.S. Makowski (Ed.), Advances in Clinical Chemistry, Elsevier Academic Press Inc., San DIego, CA, 2016, pp. 1-31.
[14] D.F. Hayes, M. Cristofanilli, G.T. Budd, M.J. Ellis, A. Stopeck, M.C. Miller, J. Matera, W.J. Allard, G.V. Doyle, L.W.M.M. Terstappen, Circulating tumor cells at each follow-up time point during therapy of metastatic breast cancer patients predict progression-free and overall survival, Clinical Cancer Research 12(14) (2006) 4218-4224.

[15] Z. Zhou, M. Qutaish, Z. Han, R.M. Schur, Y. Liu, D.L. Wilson, Z.-R. Lu, MRI detection of breast cancer micrometastases with a fibronectin-targeting contrast agent, Nature Communications 6 (2015) 1-11.
[16] M. Banys, A. Hartkopf, N. Krawczyk, T. Kaiser, F. Meier-Stiegen, T. Fehm, H. Neubauer, Dormancy in breast cancer, Breast Cancer: Targets and Therapy 4 (2012) 183-191.
[17] S. Paget, The distribution of secondary growths in cancer of the breast, Cancer and Metastasis Reviews 8(2) (1889) 98-101.
[18] R.N. Kaplan, S. Rafii, D. Lyden, Preparing the "soil": the premetastatic niche, Cancer Research 66(23) (2006) 11089-11093.
[19] S. Hiratsuka, A. Watanabe, H. Aburatani, Y. Maru, Tumour-mediated upregulation of chemoattractants and recruitment of myeloid cells predetermines lung metastasis, Nature Cell Biology 8(12) (2006) 1369-1375.
[20] H.H. Yan, M. Pickup, Y. Pang, A.E. Gorska, Z. Li, A. Chytil, Y. Geng, J.W. Gray, H.L. Moses, L. Yang, Gr-1+CD11b+ myeloid cells tip the balance of immune protection to tumor promotion in the premetastatic lung, Cancer Research 70(15) (2010) 6139-6149.
[21] L. Sompayrac, How the immune system works, 4th ed., John Wiley & Sons, West Sussex, UK, 2012.
[22] C. Khanna, K. Hunter, Modeling metastasis in vivo, Carcinogenesis 26(3) (2005) 513-523.
[23] R. Cailleau, R. Young, M. Olivé, W.J. Reeves Jr., Breast tumor cell lines from pleural effusions, Journal of the National Cancer Institute 53(3) (1974) 661-674.
[24] C.J. Aslakson, F.R. Miller, Selective events in the metastatic process defined by analysis of the sequential dissemination of subpopulations of a mouse mammary tumor, Cancer Research 52(6) (1992) 1399-1405.
[25] G. Francia, W. Cruz-Munoz, S. Man, P. Xu, R.S. Kerbel, Mouse models of advanced spontaneous metastasis for experimental therapeutics, Nature Reviews Cancer 11(2) (2011) 135-141.
[26] I.J. Fidler, Biological behavior of malignant melanoma cells correlated to their survival *in vivo*, Cancer Research 35(1) (1975) 218-224.
[27] G. Poste, J. Doll, I.R. Hart, I.J. Fidler, *In vitro* selection of murine B16 melanoma variant with enhanced tissue-invasive properties, Cancer Research 40(5) (1980) 1636-1644.
[28] C. Kuperwasser, S. Dessain, B.E. Bierbaum, D. Garnet, K. Sperandio, G.P. Gauvin, S.P. Naber, R.A. Weinberg, M. Rosenblatt, A mouse model of human breast cancer metastasis to human bone, Cancer Research 65(14) (2005) 6130-6138.
[29] J.E. Moreau, K. Anderson, M.J. R., T. Nguyen, D.L. Kaplan, M. Rosenblatt, Tissue-engineered bone serves as a target for metastasis of human breast cancer in a mouse model, Cancer Research 67(21) (2007) 10304-10308.
[30] F.P. Seib, J.E. Berry, Y. Shiozawa, R.S. Taichman, D.L. Kaplan, Tissue engineering a surrogate niche for metastatic cancer cells, Biomaterials 51 (2015) 313-319.
[31] F. Bersani, J. Lee, M. Yu, R. Morris, R. Desai, S. Ramaswamy, M. Toner, D.A. Haber, B. Parekkadan, Bioengineered implantable scaffolds as a tool to study stromal-derived factors in metastatic cancer models, Cancer Research 74(24) (2014) 7229-7238.
[32] L. Thibaudeau, A.V. Taubenberger, B.M. Holzapfel, V.M. Quent, T. Fuehrmann, P. Hesami, T.D. Brown, P.D. Dalton, C.A. Power, B.G. Hollier, D.W. Hutmacher, A tissue-

engineered humanized xenograft model of human breast cancer metastasis to bone, Disease Models & Mechanisms 7(2) (2014) 299-309.
[33] B.M. Holzapfel, F. Wagner, D. Loessner, N.P. Holzapfel, L. Thibaudeau, R. Crawford, M.-T. Ling, J.A. Clements, P.J. Russell, D.W. Hutmacher, Species-specific homing mechanisms of human prostate cancer metastasis in tissue engineered bone, Biomaterials 35 (2014) 4108-4115.
[34] R. Fernández-Periáñez, I. Molina-Privado, F. Rojo, I. Guijarro-Muñoz, V. Alonso-Camino, S. Zazo, M. Compte, A.M. Álvarez-Méndez, L. Sanz, L. Álvarez-Vallina, Basement membrane-rich organoids with functional human blood vessels are permissive niches for human breast cancer metastasis, PLOS ONE 8(8) (2013) 1-14.
[35] E. Lengyel, Ovarian cancer development and metastasis, American Journal of Pathology 177(3) (2010) 1053-1064.
[36] A. de la Fuente, L. Alonso-Alconada, C. Costa, J. Cueva, T. Garcia-Caballero, R. Lopez-Lopez, M. Abal, M-Trap: exosome-based capture of tumor cells as a new technology in peritoneal metastasis, JNCI: Journal of the National Cancer Institute 107(9) (2015) 1-10.
[37] H. Lu, W. Ouyang, C. Huang, Inflammation, a key event in cancer development, Molecular Cancer Research 4(4) (2006) 221-233.
[38] C.-Y. Ko, L. Wu, A.M. Nair, Y.-T. Tsai, V.K. Lin, L. Tang, The use of chemokine-releasing tissue engineering scaffolds in a model of inflammatory response-mediated melanoma cancer metastasis, Biomaterials 33(3) (2012) 876-885.
[39] S.M. Azarin, R.M. Gower, B.A. Aguado, M.E. Sullivan, A.G. Goodman, E.J. Jiang, S.S. Rao, Y. Ren, S.L. Tucker, V. Backman, J.S. Jeruss, L.D. Shea, *In vivo* capture and label-free detection of early metastatic cells, Nature Communications 6 (2015) 1-9.
[40] T. Yoneda, P.J. Williams, T. Hiraga, M. Niewolna, R. Nishimura, A bone-seeking clone exhibits different biological properties from the MDA-MB-231 parental human breast cancer cells and a brain-seeking clone in vivo and in vitro, J. Bone Miner. Res. 16(8) (2001) 1486-1495.
[41] S.S. Rao, G.G. Bushnell, S.M. Azarin, G. Spicer, B.A. Aguado, J.R. Stoehr, E.J. Jiang, V. Backman, L.D. Shea, J.S. Jeruss, Enhanced survival with implantable scaffold that capture metastatic breast cancer cells *in vivo*, Cancer Research 76(18) (2016) 5209-5218.
[42] B.A. Aguado, J.J. Wu, S.M. Azarin, D. Nanavati, S.S. Rao, G.G. Bushnell, C.B. Medicherla, L.D. Shea, Secretome identification of immune cell factors mediating metastatic cell homing, Scientific Reports 5 (2015) 1-13.
[43] W.B. Fang, I. Jokar, A. Zou, D. Lambert, P. Dendukuri, N. Cheng, CCL2/CCR2 chemokine signaling coordinates survival and motility of breast cancer cells through Smad3 protein- and p42/44 mitogen-activated protein kinase (MAPK)-dependent mechanisms, Journal of Biological Chemistry 287(43) (2012) 36593-36608.
[44] N. Erez, L.M. Coussens, Leukocytes as paracrine regulators of metastasis and determinants of organ-specific colonization, International Journal of Cancer 128(11) (2011) 2536-2544.
[45] B.-Z. Qian, J. Li, H. Zhang, T. Kitamura, J. Zhang, L.R. Campion, E.A. Kaiser, L.A. Snyder, J.W. Pollard, CCL2 recruits inflammatory monocytes to facilitate breast-tumour metastasis, Nature 475(7355) (2011) 222-225.

[46] B.-Z. Qian, Y. Deng, J.H. Im, R.J. Muschel, Y. Zou, J. Li, R.A. Lang, J.W. Pollard, A distinct macrophage population mediates metastatic breast cancer cell extravasation, establishment and growth, PLOS ONE 4(8) (2009) 1-16.
[47] J. Sceneay, M.T. Chow, A. Chen, H.M. Halse, C.S.F. Wong, D.M. Andrews, E.K. Sloan, B.S. Parker, D.D. Bowtell, M.J. Smyth, A. Möller, Primary tumor hypoxia recruits CD11b+/Ly6Cmed/Ly6G+ immune suppressor cells and compromises NK cell cytotoxicity in the premetastatic niche, Cancer Research 72(16) (2012) 3906-3911.
[48] E.Y. Lin, A.V. Nguyen, R.G. Russell, J.W. Pollard, Colony-stimulating factor 1 promotes progression of mammry tumors to malignancy, Journal of Experimental Medicine 193(6) (2001) 727-739.
[49] H. Peinado, S. Lavotshkin, D. Lyden, The secreted factors responsible for pre-metastatic niche formation: old sayings and new thoughts, Seminars in Cancer Biology 21(2) (2011) 139-146.
[50] J.T. Erler, K.L. Bennewith, T.R. Cox, G. Lang, D. Bird, A. Koong, Q.-T. Le, A.J. Giaccia, Hypoxia-induced lysyl oxidase is a critical mediator of bone marrow cell recruitment to form the premetastatic niche, Cancer Cell 15(1) (2009) 35-44.
[51] M.-Y. Kim, T. Oskarsson, S. Acharyya, D.X. Nguyen, X.H.-F. Zhang, L. Norton, J. Massagué, Tumor self-seeding by circulating cancer cells, Cell 139(7) (2009) 1315-1326.
[52] G. Gundem, P. Van Loo, B. Kremeyer, L.B. Alexandrov, J.M.C. Tubio, E. Papaemmanuil, D.S. Brewer, H.M.L.K. Kallio, G. Högnäs, M. Annala, K. Kivinummi, V. Goody, C. Latimer, S. O'Meara, K.J. Dawson, W. Isaacs, M.R. Emmert-Buck, M. Nykter, C. Foster, Z. Kote-Jarai, D. Easton, H.C. Whitaker, I.P.U. Group, D.E. Neal, C.S. Cooper, R.A. Eeles, T. Visakorpi, P.J. Campbell, U. McDermott, D.C. Wedge, G.S. Bova, The evolutionary history of lethal metastatic prostate cancer, Nature 520(7547) (2015) 353-357.
[53] L.K. Fung, W.M. Saltzmann, Polymeric implants for cancer chemotherapy, Advanced Drug Delivery Reviews 26(2-3) (1997) 209-230.
[54] M.M. Gottesman, Mechanisms of cancer drug resistance, Annual Review of Medicine 53 (2002) 615-627.
[55] K.F. Chu, D.E. Dupuy, Thermal ablation of tumours: biological mechanisms and advances in therapy, Nature Reviews Cancer 14(3) (2014) 199-208.
[56] J.R. Caso, M. Tsivian, V. Mouraviev, T.J. Polascik, Predicting biopsy-proven prostate cancer recurrence following cryosurgery, Urologic Oncology: Seminars and Original Investigations 30(4) (2012) 391-395.
[57] B. Al-Sakere, F. André, C. Bernat, E. Connault, P. Opolon, R.V. Davalos, B. Rubinsky, L.M. Mir, Tumor ablation with irreversible electroporation, PLOS ONE 2(11) (2007) 1-8.
[58] J. van der Zee, Heating the patient: a promising approach?, Annals of Oncology 13(8) (2002) 1173-1184.
[59] D.I. Rosenthal, F.J. Hornicek, M.W. Wolfe, L.C. Jennings, M.C. Gebhardt, H.J. Mankin, Percutaneous radiofrequency coagulation of osteoid osteoma compared with operative treatment, Journal of Bone and Joint Surgery 80(6) (1998) 815-821.
[60] S. McDermott, D.A. Gervais, Radiofrequency ablation of liver tumors, Seminars in Interventional Radiology 30(1) (2013) 49-55.
[61] B.J. Wood, J.R. Ramkaransingh, T. Fojo, M.M. Walther, S.K. Libutti, Percutaneous tumor ablation with radiofrequency, Cancer 94(2) (2002) 443-451.

[62] S.A. Sapareto, L.E. Hopwood, W.C. Dewey, M.R. Raju, J.W. Gray, Effects of hyperthermia on survival and progression of chinese hamster ovary cells, Cancer Research 38(2) (1978) 393-400.
[63] K.C. Kregel, Heat shock proteins: modifying factors in physiological stress responses and acquired thermotolerance, Journal of Applied Physiology 92(5) (2001) 2177-2186.
[64] X. He, J.C. Bischof, Quantification of temperature and injury response in thermal therapy and cryosurgery, Critical Reviews in Biomedical Engineering 31(5&6) (2003) 355-421.
[65] C.J. Diederich, Thermal ablation and high-temperature thermal therapy: overview of technology and clinical implementation, International Journal of Hyperthermia 21(8) (2005) 745-753.
[66] M. Johannsen, B. Thiesen, P. Wust, A. Jordan, Magnetic nanoparticle hyperthermia for prostate cancer, International Journal of Hyperthermia 26(8) (2010) 790-795.
[67] M.L. Etheridge, J.C. Bischof, Optimizing Magnetic Nanoparticle Based Thermal Therapies Within the Physical Limits of Heating, Annals of Biomedical Engineering 41(1) (2013) 78-88.
[68] M.S. Sabel, Cryo-immunology: a review of the literature and proposed mechanisms for stimulatory versus suppressive immune responses, Cryobiology 58(1) (2009) 1-11.
[69] S. Tatlı, M. Acar, K. Tuncalı, P.R. Morrison, S. Silverman, Percutaneous cryoablation techniques and clinical applications, Diagnostic and Interventional Radiology 16(1) (2010) 90-95.
[70] M.L. Yarmush, A. Golberg, G. Serša, T. Kotnik, D. Miklavčič, Electroporation-based technologies for medicine: principles, applications, and challenges, Annual Review of Biomedical Engineering 16 (2014) 295-320.
[71] R.V. Davalos, L.M. Mir, B. Rubinsky, Tissue ablation with irreversible electroporation, Annals of Biomedical Engineering 33(2) (2005) 223-231.
[72] E. Neumann, M. Schaefer-Ridder, Y. Wang, P.H. Hofschneider, Gene transfer into mouse lyoma cells by electroporation in high electric fields, EMBO Journal 1(7) (1982) 841-845.
[73] S. Campelo, M. Valerio, H. Ahmed, Y. Hu, S.L. Arena, R.E. Neal II, M. Emberton, C.B. Arena, An evaluation of irreversible electroporation thresholds in human prostate cancer and potential correlations to physiological measurements, APL Bioengineering 1 (2017) 1-10.
[74] D.M. Pardoll, The blockade of immune checkpoints in cancer immunotherapy, Nature Reviews Cancer 12(4) (2012) 252-264.
[75] G. Fyfe, R.I. Fisher, S.A. Rosenberg, M. Sznol, D.R. Parkinson, A.C. Louie, Results of Treatment of 255 Patients with Metastatic Renal-Cell Carcinoma Who Received High-Dose Recombinant Interleukin-2 Therapy, Journal of Clinical Oncology 13(3) (1995) 688-696.
[76] A. Alva, G.A. Daniels, M.K.K. Wong, H.L. Kaufman, M.A. Morse, D.F. McDermott, J.I. Clark, S.S. Agarwala, G. Miletello, T.F. Logan, R.J. Hauke, B. Curti, J.M. Kirkwood, R. Gonzalez, A. Amin, M. Fishman, N. Agarwal, J.N. Lowder, H. Hua, S. Aung, J.P. Dutcher, Contemporary experience with high‐dose interleukin‐2 therapy

and impact on survival in patients with metastatic melanoma and metastatic renal cell carcinoma, Cancer Immunology Immunotherapy 65(12) (2016) 1533-1544.
[77] H. Nagai, M. Muto, Optimal management of immune‐related adverse events resulting from treatment with immune checkpoint inhibitors: a review and update, International Journal of Clinical Oncology 23(3) (2018) 410-420.
[78] V. Jindal, E. Arora, S. Gupta, Challenges and prospects of chimeric antigen receptor T cell therapy in solid tumors, Medical Oncology 35(6) (2018) 1-9.
[79] B.D. Shields, F. Mahmoud, E.M. Taylor, S.D. Byrum, D. Sengupta, B. Koss, S. Ransom, K. Cline, S.G. Mackintosh, R.D. Edmondson, S. Shalin, A.J. Tackett, Indicators of responsiveness to immune checkpoint inhibitors, Scientific Reports 7(807) (2017) 1-12.
[80] Z.J. Roberts, M. Better, A. Bot, M.R. Roberts, A. Ribas, Axicabtagene ciloleucel, a first-in-class CAR T cell therapy for aggressive NHL, Leukemia & Lymphoma (2017) 1-12.
[81] M.H.M.G.M. den Brok, R.P.M. Sutmuller, S. Nierkens, E.J. Bennink, C. Frielink, L.W.J. Toonen, O.C. Boerman, C.G. Figdor, T.J.M. Ruers, G.J. Adema, Efficient loading of dendritic cells following cryo and radiofrequency ablation in combination with immune modulation induces anti-tumour immunity, British Journal of Cancer 95(7) (2006) 896-905.
[82] O.A. Ali, D. Emerich, G. Dranoff, D.J. Mooney, In Situ Regulation of DC Subsets and T Cells Mediates Tumor Regression in Mice, Science Translational Medicine 1(8) (2009) 1-10.
[83] H. Ma, J. Luo, Z. Sun, L. Xia, M. Shi, M. Liu, J. Chang, C. Wu, 3D printing of biomaterials with mussel-inspired nanostructures for tumor therapy and tissue regeneration, Biomaterials 111 (2016) 138-148.
[84] J. Zhang, J. Li, N. Kawazoe, G. Chen, Composite scaffolds of gelatin and gold nanoparticles with tunable size and shape for photothermal cancer therapy, Journal of Materials Chemistry B 5(2) (2017) 245-253.
[85] A. Gloria, T. Russo, U. D'Amora, S. Zeppetelli, T.L. D'Alessandro, M. Sandri, M. Bañobre-López, Y. Piñeiro-Redondo, M. Uhlarz, A. Tampieri, J. Rivas, T. Herrmannsdörfer, V.A. Dediu, L. Ambrosio, R.D. Santis, Magnetic Poly(ε-caprolactone)/Iron-Doped Hydroxyapatite Nanocomposite Substrates for Advanced Bone Tissue Engineering, Journal of the Royal Society Interface 10(80) (2013).
[86] J. Zhang, S. Zhao, M. Zhu, Y. Zhu, Y. Zhang, Z. Liu, C. Zhang, 3D-printed magnetic Fe3O4/MBG/PCL composite scaffolds with multifunctionality of bone regeneration, local anticancer drug delivery and hyperthermia, Journal of Materials Chemistry B 2(43) (2014) 7583-7595.
[87] P.R. Stauffer, T.C. Cetas, R.C. Jones, Magnetic induction heating of ferromagnetic implants for inducing localized hyperthermia in deep-seated tumors, IEEE Transactions on Biomedical Engineering 31(2) (1984) 235-251.
[88] J. Jiang, R. Goel, S. Schmechel, G. Vercellotti, C.L. Forster, J.C. Bischof, Pre-conditioning cryosurgery: Cellular and molecular mechanisms and dynamics of TNF-α enhanced cryotherapy in an *in vivo* prostate cancer model system, Cryobiology 61(3) (2010) 280-288.

[89] S. Thomsen, Non-thermal effects in thermal treatment applications of non-ionizing irradiation, in: T.P. Ryan (Ed.) Conference on Treatment of Tissue: Energy Delivery and Assessment III, Proceedings of SPIE, San Jose, CA, 2005, pp. 1-14.
[90] L. Li, Z. Zeng, Z. Qi, X. Wang, X. Gao, H. Wei, R. Sun, Z. Tian, Scientific Reports 5 (2015) 1-11.
[91] O.F. Bertrand, R. Sipehia, R. Mongrain, J. Rodés, J.-C. Tardif, L. Bilodeau, G. Côté, M.G. Bourassa, Biocompatibility aspects of new stent technology, Journal of the American College of Cardiology 32(3) (1998) 562-571.
[92] P. Mandracci, F. Mussano, P. Rivolo, S. Carossa, Surface treatments and functional coatings for biocompatibility improvement and bacterial adhesion reduction in dental implantology Coatings 6(1) (2016) 1-22.
[93] L. Xu, A. Yamamoto, Characteristics and cytocompatibility of biodegradable polymer film on magnesium by spin coating, Colloids and Surfaces B: Biointerfaces 93 (2012) 67-74.
[94] J. Lahann, D. Klee, H. Thelen, H. Biernert, D. Vorwerk, H. Höcker, Improvement of Haemocompatibility of Metallic Stents by Polymer Coating, Journal of Materials Science: Materials in Medicine 10(7) (1999) 443-448.
[95] I.K. De Scheerder, K.L. Wilczek, E.V. Verbeken, J. Vandorpe, P.N. Lan, E. Schacht, J. Piessens, H. De Geest, Biocompatibility of biodegradable and nonbiodegradable polymer-coated stents implanted in porcine peripheral arteries, CardioVascular and Interventional Radiology 18(4) (1995) 227-232.
[96] S.H. Lee, I. Szinai, K. Carpenter, R. Katsarava, G. Jokhadze, C.-C. Chu, Y. Huang, E.V. Verbeken, O. Bramwell, I.K. De Scheerder, M.K. Hong, In-vivo biocompatibility evaluation of stents coated with a new biodegradable elastomeric and functional polymer, Coronary Artery Disease 13(4) (2002) 237-241.
[97] M.R. Sorensen, S.R. Pedersen, A. Lindkvist, J.P. Christensen, A.R. Thomsen, Quantification of B16 melanoma cells in lungs using triplex Q-PCR - a new approach to evaluate melanoma cell metastasis and tumor control, PLOS ONE 9(1) (2014) 1-9.
[98] M.B. Asparuhova, C. Secondini, C. Rüegg, R. Chiquet-Ehrishmann, Mechanism of irradiation-induced mammary cancer metastasis: a role for SAP-dependent Mkl1 signaling, Molecular Oncology 9(8) (2015) 1510-1527.
[99] P.L. Pereira, Actual role of radiofrequency ablation of liver metastases, European Radiology 17(8) (2007) 2062-2070.
[100] M. Ahmed, C.L. Brace, F.T. Lee, S.N. Goldberg, Principle of and advances in percutaneous ablation, Radiology 258(2) (2011) 351-369.
[101] E. Paulet, C. Aubé, P. Pessaux, J. Lebigot, E. Lhermitte, F. Oberti, A. Ponthieux, P. Calès, C. Ridereau-Zins, P.L. Pereira, Factors limiting complete tumor ablation by radiofrequency ablation, CardioVascular and Interventional Radiology 31(1) (2008) 107-115.
[102] J.G. Liu, F.L. Chen, C.L. Ge, M.Y. Gong, H.B. Zuo, J.R. Zhang, Cryosurgery for treatment of subcutaneously xenotransplanted tumors in rats and its effect on cellular immunity, Technology in Cancer Research and Treatment 10(4) (2011) 339-346.
[103] R. Waitz, S.B. Solomon, E.N. Petre, A.E. Trumble, M. Fassò, L. Norton, J.P. Allison, Potent induction of tumor immunity by combining tumor cryoablation with anti–CTLA-4 therapy, Cancer Research 72(2) (2012) 430-439.

[104] A. Machlenkin, O. Goldberger, B. Tirosh, A. Paz, I. Volovitz, E. Bar-Haim, S.-H. Lee, E. Vadai, E. Tzehoval, L. Eisenbach, Combined dendritic cell cryotherapy of tumor induces systemic antimetastatic immunity, Clinical Cancer Research 11(13) (2005) 4955-4961.
[105] M.H.M.G.M. den Brok, R.P.M. Sutmuller, R. van der Voort, E.J. Bennink, C.G. Figdor, T.J.M. Ruers, G.J. Adema, *In situ* ablation creates an antigen source for the generation of antitumor immunity, Cancer Research 64(11) (2004) 4024-4029.
[106] A. Zerbini, M. Pilli, A. Penna, G. Pelosi, C. Schianchi, A. Molinari, S. Schivazappa, C. Zibera, F.F. Fagnoni, C. Ferrari, G. Missale, Radiofrequency thermal ablation of hepatocellular carcinoma liver nodules can Activate and enhance tumor-specific T-cell responses, Cancer Research 66(2) (2006) 1139-1146.
[107] A. Mukhopadhaya, J. Mendecki, X. Dong, L. Liu, S. Kalnicki, M. Garg, A. Alfieri, C. Guha, Localized hyperthermia combined with intratumoral dendritic cells induces systemic antitumor immunity, Cancer Research 67(16) (2007) 7798-7806.
[108] R.E. Neal II, J.H. Rossmeisl Jr., J.L. Robertson, C.B. Arena, E.M. Davis, R.N. Singh, J. Stallings, R.V. Davalos, Improved local and systemic anti-tumor efficacy for irreversible electroporation in immunocompetent versus immunodeficient mice, PLOS ONE 2013(8) (2013) 5.
[109] Q. Shao, S. O'Flanagan, T. Lam, P. Roy, F. Pelaez, B. Burbach, S.M. Azarin, Y. Shimizu, J.C. Bischof, Engineering T cell response to cancer antigens by choice of focal therapeutic conditions, In Revision.
[110] M.M. Shenoi, I. Iltis, J. Choi, N.A. Koonce, G.J. Metzger, R.J. Griffin, J.C. Bischof, Nanoparticle delivered vascular disrupting agents (VDAs): use of TNF-alpha conjugated gold nanoparticles for multimodal cancer therapy, Molecular Pharmaceutics 10(5) (2013) 1683-1694.
[111] M.L. Etheridge, J. Choi, S. Ramadhyani, J.C. Bischof, Methods for characterizing convective cryoprobe heat transfer in ultrasound gel phantoms, Journal of Biomechanical Engineering 135 (2013) 1-10.
[112] Q. Shao, L. Feng, C. Chung, K. Elahi-Gedwillo, P.P. Provenzano, B. Forsyth, J.C. Bischof, Physical and chemical enhancement of and adaptive resistance to irreversible electroporation of pancreatic cancer, Annals of Biomedical Engineering 46(1) (2018) 25-36.
[113] C. Jiang, Q. Shao, J.C. Bischof, Pulse timing during irreversible electroporation achieves enhanced destruction in a hindlimb model of cancer, Annals of Biomedical Engineering 43(4) (2015) 887-895.
[114] Z. Osman, M.I. Mohd Ghazali, L. Othman, K.B. Md Isa, AC ionic conductivity and DC polarization method of lithium ion transport in PMMA–LiBF4 gel polymer electrolytes, Results in Physics 2 (2012) 1-4.
[115] G. Tan, R. Xu, Z. Xing, Y. Yuan, J. Lu, J. Wen, C. Liu, L. Ma, C. Zhan, Q. Liu, T. Wu, Z. Jian, R. Shahbazian-Yassar, Y. Ren, D.J. Miller, L.A. Curtiss, X. Ji, K. Amine, Burning lithium in CS2 for high-performing compact Li2S–graphene nanocapsules for Li–S batteries, Nature Energy 2(7) (2017) 1-10.
[116] Y. Gavrieli, Y. Sherman, S.A. Ben-Sasson, Identification of programmed cell death *in situ* via specific labeling nuclear DNA fragmentation, Journal of Cell Biology 119(3) (1992) 493-501.

[117] D. Kanduc, A. Mittelman, R. Serpico, E. Sinigaglia, A.A. Sinha, C. Natale, R. Santacroce, M.G. Di Corcia, A. Lucchese, L. Dini, P. Pani, S. Santacroce, S. Simone, R. Bucci, E. Farber, Cell death: apoptosis versus necrosis (review), International Journal of Oncology 21(1) (2002) 165-170.
[118] R.-F. Wang, E. Appella, Y. Kawakami, X. Kang, S.A. Rosenberg, Identification of TRP-2 as a human tumor antigen recognized by cytotoxic T lymphocytes, Journal of Experimental Medicine 184(6) (1996) 2207-2216.
[119] T. Fujino, Y. Yokoyama, Y.H. Mori, Augmentation of laminar forced-convective heat transfer by the application of a transverse electric field, Journal of Heat Transfer 111(1-4) (1989) 345-351.
[120] C. Jiang, R.V. Davalos, J.C. Bischof, A review of basic to clinical studies of irreversible electroporation therapy, IEEE Transactions on Biomedical Engineering 62(1) (2015) 4-20.
[121] Z. Qin, J. Jiang, G. Long, B. Lindgren, J.C. Bischof, Irreversible electroporation: an *in vivo* study with dorsal skin fold chamber, Annals of Biomedical Engineering 41(3) (2013) 619-629.
[122] T.J.C. Faes, H.A. van der Meij, J.C. de Munck, R.M. Heethaar, The electric resistivity of human tissues (100 Hz–10 MHz): a meta-analysis of review studies, Physiological Measurement 20(4) (1999) R1-R10.
[123] M.H.M.G.M. den Brok, R.P.M. Sutmuller, S. Nierkens, E.J. Bennink, L.W.J. Toonen, C.G. Figdor, T.J.M. Ruers, G.J. Adema, Synergy between *in situ* cryoablation and TLR9 stimulation results in a highly effective *in vivo* dendritic cell vaccine, Cancer Research 66(14) (2006) 7285-7292.
[124] D.M. Klinman, Immunotherapeutic uses of CpG oligodeoxynucleotides, Nature Reviews Immunology 4(4) (2004) 248-257.
[125] W.B. Liechty, D.R. Kryscio, B.V. Slaughter, N.A. Peppas, Polymers for Drug Delivery Systems, Annual Review of Chemical and Biomolecular Engineering, Annual Reviews, Palo Alto, 2010, pp. 149-173.
[126] C. Déjugnat, G.B. Sukhorukov, pH-responsive properties of hollow polyelectrolyte microcapsules templated on various cores, Langmuir 20(17) (2004) 7265-7269.
[127] N. Forbes, J.E. Shin, M. Ogunyankin, J.A. Zasadzinski, Inside-outside self-assembly of light-activated fast-release liposomes, Physical Chemistry Chemical Physics 17(24) (2015) 15569-15578.
[128] M.B. Yatvin, J.N. Weinstein, W.H. Dennis, R. Blumenthal, Design of liposomes for enhanced local release of drugs by heyperthermia, Science 202(4374) (1978) 1290-1293.
[129] W. Harbich, W. Helfrich, Alignment and opening of giant lecithin vesicles by electric fields, Journal of Physical Sciences 34(9) (1979) 1063-1065.
[130] D.R. Nisbet, L.M.Y. Yu, T. Zahir, J.S. Forsythe, M.S. Shoichet, Characterization of neural stem cells on electrospun poly(ε-caprolactone) submicron scaffolds: evaluating their potential in neural tissue engineering, Journal of Biomaterials Science, Polymer Edition 19(5) (2008) 623-634.
[131] K.A. Hlavaty, R.F. Gibly, X. Zhang, C.B. Rives, J.G. Graham, W.L. Lowe Jr., X. Luo, L.D. Shea, Enhancing Human Islet Transplantation by Localized Release of Trophic Factors From PLG Scaffolds, American Journals of Transplantation 14 (2014) 1523-1532.

[132] P.C. Weber, D.H. Ohlendrof, J.J. Wendoloski, F.R. Salemme, Structural origins of high-affinity biotin binding to streptavidin, Science 243(4887) (1989) 85-88.
[133] M.K. Horne, D.R. Nisbet, J.S. Forsythe, C.L. Parish, Three-dimensional nanofibrous scaffolds incorporating immobilized BDNF promote proliferation and differentiation of cortical neural stem cells, Stem Cells and Development 19(6) (2010) 843-852.
[134] T.I. Croll, A.J. O'Connor, G.W. Stevens, J.J. Cooper-White, Controllable surface modification of poly(lactic-*co*-glycolic acid) (PLGA) by hydrolysis or aminolysis I: physical, chemical, and theoretical aspects, Biomacromolecules 5(2) (2004) 463-473.
[135] C.E. Argaraña, I.D. Kuntz, S. Birken, R. Axel, C.R. Cantor, Molecular cloning and nucleotide sequence of the streptavidin gene, Nucleic Acids Research 14(4) (1986) 1871-1882.
[136] D. Sehgal, I.K. Vijay, A method for the high efficiency of water-soluble carbodiimide-mediated amidation, Analytical Biochemistry 218(1) (1994) 87-91.
[137] M.H. Kish, S. Borhani, Degradation cracking of poly(ethylene terephthalate) filaments by methylamine and *N*-propylamine, Journal of Applied Polymer Science 78(11) (2000) 1923-1931.
[138] Z. Wei, Z. Gu, A study of one-bath alkali-amine hydrolysis and silk-fibroin finishing of polyester microfiber, Journal of Applied Polymer Science 81(6) (2001) 1467-1473.
[139] S. Udenfriend, S. Stein, P. Böhlen, W. Dairman, W. Leimbruber, M. Weigele, Fluorescamine: a reagent for assay of amino acids, peptides, proteins, and primary amines in the picomole range, Science 178(4063) (1972) 871-872.
[140] M.M. Kämpf, E.H. Christen, M. Ehrbar, M. Daoud-El Baba, G. Charpin-El Hamri, M. Fussenegger, W. Weber, A gene therapy technology-based biomaterial for the trigger-inducible release of biopharmaceuticals in mice, Advanced Functional Materials 20(15) (2010) 2534-2538.
[141] D.A. Fluri, C. Kemmer, M. Daoud-El Baba, M. Fussenegger, A novel system for trigger-controlled drug release from polymer capsules, Journal of Controlled Release 131(3) (2008) 211-219.
[142] T.M. Allen, P.R. Cullis, Liposomal drug delivery systems: from concept to clinical applications, Advanced Drug Delivery Reviews 65(1) (2012) 36-48.
[143] U. Bulbake, S. Doppalapudi, N. Kommineni, W. Khan, Liposomal formulations in clinical use: an updated review, Pharmaceutics 9(12) (2017) 1-33.
[144] B. Kneidl, M. Peller, G. Winter, L.H. Lindner, M. Hossann, Thermosensitive liposomal drug delivery systems: state of the art review, International Journal of Nanomedicine 9 (2014) 4387-4398.
[145] C.D. Landon, J.Y. Park, D. Needham, M.W. Dewhirst, Nanoscale drug delivery and hyperthermia: the materials design and preclinical and clinical testing of low temperature-sensitive liposomes used in combination with mild hyperthermia in the treatment of local cancer, Open Nanomedicine Journal 3 (2011) 38-64.
[146] Study of ThermoDox With Standardized Radiofrequency Ablation (RFA) for Treatment of Hepatocellular Carcinoma (HCC), https://ClinicalTrials.gov/show/NCT02112656.
[147] M. Kummrow, W. Helfrich, Deformation of giant lipid vesicles by electric fields, Physical Review A 44(12) (1991) 8356-8360.

[148] J.C. Weaver, Electroporation - a General Phenomenon for Manipulating Cells and Tissues, J. Cell. Biochem. 51(4) (1993) 426-435.
[149] J.E. Kurtz, I. Ray-Coquard, PI3 Kinase Inhibitors in the Clinic: An Update, Anticancer Research 32(7) (2012) 2463-2470.
[150] L. Tian, Y. Qiao, P. Lee, L. Wang, A. Chang, S. Ravi, T.A. Rogers, L.F. Lu, B. Singhana, J. Zhao, M.P. Melancon, Antitumor efficacy of liposome-encapsulated NVP-BEZ 235 in combination with irreversible electroporation, Drug Deliv. 25(1) (2018) 668-678.
[151] H.W. Zhang, Thin-Film Hydration Followed by Extrusion Method for Liposome Preparation, Liposomes: Methods and Protocols, 2nd Edition, Humana Press Inc, Totowa, 2017, pp. 17-22.
[152] T.F. Zhu, I. Budin, J.W. Szostak, Preparation of Fatty Acid or Phospholipid Vesicles by Thin-film Rehydration, Laboratory Methods in Enzymology: Cell, Lipid and Carbohydrate, Elsevier Academic Press Inc, San Diego, 2013, pp. 267-274.
[153] T. Wink, S.J. van Zuilen, A. Bult, W.P. van Bennekom, Liposome-mediated enhancement of the sensitiviy in immunoassays of proteins and peptides in surface plasmon resonance spectrometry, Analytical Chemistry 70(5) (1998) 827-832.
[154] R.M. Levine, T.R. Pearce, M. Adil, E. Kokkoli, Preparation and characterization of liposome-encapsulated plasmid
DNA for gene delivery, Langmuir 29(29) (2013) 9208-9215.
[155] M.J. Hope, M.B. Bally, G. Webb, P.R. Cullis, Production of Large Unilamellar Vesicles by a Rapid Extrusion Procedure - Characterization of Size Distribution, Trapped Volume and Ability to Maintain a Membrane-Potential, Biochimica Et Biophysica Acta 812(1) (1985) 55-65.
[156] R.F. Chen, J.R. Knutson, Mechanism of Fluorescence Concentration Quenching of Carboxyfluorescein in Liposomes - Energy-Transfer to Nonfluorescent Dimers, Analytical Biochemistry 172(1) (1988) 61-77.
[157] J. Yi, A.J. Barrow, N. Yu, B.E. O'Neill, Efficient electroporation of liposomes doped with pore stabilizing nisin, J. Liposome Res. 23(3) (2013) 197-202.
[158] N. Forbes, A. Pallaoro, N.O. Reich, J.A. Zasadzinski, Rapid, Reversible Release from Thermosensitive Liposomes Triggered by Near-Infra-Red Light, Particle & Particle Systems Characterization 31 (2014) 1158-1167.
[159] M.O. Eze, Phase-Transitions in Phospholipid-Bilayers - Lateral Phase Separations Play Vital Roles in Biomembranes, Biochem. Educ. 19(4) (1991) 204-208.
[160] B. Alberts, A. Johnson, J. Lewis, M. Raff, K. Roberts, P. Walter, The Lipid Bilayer, Molecular Biology of the Cell, Garland Science, New York, 2002.
[161] B.R. Lentz, Y. Barenholz, T.E. Thompson, Fluorescence Depolarization Studies of Phase-Transitions and Fluidity in Phospholipid Bilayers. 1. Single Component Phosphatidylcholine Liposomes, Biochemistry 15(20) (1976) 4521-4528.
[162] P.J. Davis, B.D. Fleming, K.P. Coolbear, K.M.W. Keough, Gel to Liquid-Crystalline Transition-Temperatures of Water Dispersions of 2 Pairs of Positional Isomers of Unsaturated Mixed-Acid Phosphatidylcholines, Biochemistry 20(12) (1981) 3633-3636.
[163] P.F. Salipante, P.M. Vlahovska, Vesicle deformation in DC electric pulses, Soft Matter 10(19) (2014) 3386-3393.

[164] F. Olson, C.A. Hunt, F.C. Szoka, W.J. Vail, D. Papahadjopoulos, Preparation of Liposomes of Defined Size Distribution by Extrusion through Polycarbonate Membranes, Biochimica et Biophysica Acta 557(1) (1979) 9-23.
[165] V. Filipe, A. Hawe, W. Jiskoot, Critical Evaluation of Nanoparticle Tracking Analysis (NTA) by NanoSight for the Measurement of Nanoparticles and Protein Aggregates, Pharmaceutical Research 27(5) (2010) 796-810.
[166] A. Velikonja, P. Kramar, D. Miklavčič, A.M. Lebar, Specific electrical capacitance and voltage breakdown as a function of temperature for different planar lipid bilayers, Bioelectrochemistry 112 (2016) 132-137.
[167] J.K. Lim, H. Zhou, R.D. Tilton, Liposome rupture and contents release over coplanar microelectrode arrays, J. Colloid Interface Sci. 332(1) (2009) 113-121.
[168] C.M. Diaz-Montero, M.L. Salem, M.I. Nishimura, E.G. Garrett-Mayer, D.J. Cole, A.J. Montero, Increased circulating myeloid-derived suppressor cells correlate with clinical cancer stage, metastatic tumor burden, and doxorubicin–cyclophosphamide chemotherapy, Cancer Immunology Immunotherapy 58(1) (2009) 49-59.
[169] K. Gonda, M. Shibata, T. Ohtake, Y. Matsumoto, K. Tachibana, N. Abe, H. Ohto, K. Sakurai, S. Takenoshita, Myeloid-derived suppressor cells are increased and correlated with type 2 immune responses, malnutrition, inflammation, and poor prognosis in patients with breast cancer, Oncology Letters 14(2) (2017) 1766-1774.
[170] P. Filipazzi, R. Valenti, V. Huber, L. Pilla, P. Canese, M. Iero, C. Castelli, L. Mariani, G. Parmiani, L. Rivoltini, Identification of a new subset of myeloid suppressor cells in peripheral blood of melanoma patients with modulation by a granulocyte-macrophage colony-stimulation factor–based antitumor vaccine, Journal of Clinical Oncology 25(18) (2007) 2546-2553.
[171] I. Poschke, D. Mougiakakos, J. Hansson, G.V. Masucci, R. Kiessling, Immature immunosuppressive CD14+HLA-DR−/low cells in melanoma patients are Stat3hi and overexpress CD80, CD83, and DC-Sign, Cancer Research 70(11) (2010) 4335-4345.
[172] Y. Kawakami, S. Eliyahu, C.H. Delgado, P.F. Robbins, L. Rivoltini, S.L. Topalian, T. Miki, S.A. Rosenberg, Cloning of the gene coding for a shared human melanoma antigen recognized by autologous T cells infiltrating into tumor, Proceedings of the National Academy of Sciences of the United States of America 91(9) (1994) 3515-3519.
[173] P.G. Coulie, V. Brichard, A. Van Pel, T. Wölferl, J. Schneider, C. Traversari, S. Mattei, E. De Plaen, C. Lurquin, J.-P. Szikora, J.-C. Renauld, T. Boon, A new gene coding for a differentiation antigen recognized by autologous cytolytic T lymphocytes on HLA-A2 melanomas Journal of Experimental Medicine 180(1) (1994) 35-42.
[174] Y. Kawakami, S. Eliyahu, C.H. Delgado, P.F. Robbins, K. Sakaguchi, E. Appella, J.R. Yannelli, G.J. Adema, T. Miki, S.A. Rosenberg, Identification of a human melanoma antigen recognized by tumor-infiltrating lymphocytes associated with *in vivo* tumor rejection, Proceedings of the National Academy of Sciences of the United States of America 91(14) (1994) 6458-6462.
[175] F.K. Stevenson, J. Rice, D.L. Zhu, Tumor vaccines, Advances in Immunology 82 (2004) 49-103.
[176] J.A. Wargo, S.M. Reddy, A. Reuben, P. Sharma, Monitoring immune responses in the tumor microenvironment, Current Opinion in Immunology 41 (2016) 23-31.

[177] Q. Fu, A. Satterlee, Y. Wang, Y. Wang, D. Wang, J. Tang, Z. He, F. Liu, Novel murine tumour models depend on strain and route of inoculation, International Journal of Experimental Pathology 97(4) (2016) 351-356.
[178] V.P. Baklaushev, A. Kilpeläinen, S. Petkov, M.A. Abakumov, N.F. Grinenko, G.M. Yusubalieva, A.A. Latanova, I.L. Gubskiy, F.G. Zabozlaev, E.S. Starodubova, T.O. Abakumova, M.G. Isaguliants, V.P. Chekhonin, Luciferase expression allows bioluminescence imaging but imposes limitations on the orthotopic mouse (4T1) model of breast cancer, Scientific Reports 7 (2017).
[179] L.S. Nair, C.T. Laurencin, Biodegradable polymers as biomaterials, Progress in Polymer Science 32(8-9) (2007) 762-798.
[180] A.I. Baba, C. Câtoi, Comparitive oncology, The Publishing House of the Romanian Academy, Bucharest, Romania, 2007.
[181] R.T. Sadikot, T.S. Blackwell, Bioluminescence imaging, Proceedings of the American Thoracic Society 2(6) (2005) 537-540.
[182] D.Y. Wong, S.J. Hollister, P.H. Krebsbach, C. Nosrat, Poly(epsilon-caprolactone) and poly (L-lactic-co-glycolic acid) degradable polymer sponges attenuate astrocyte response and lesion growth in acute traumatic brain injury, Tissue Eng. 13(10) (2007) 2515-2523.
[183] H.J. Sung, C. Meredith, C. Johnson, Z.S. Galis, The effect of scaffold degradation rate on three-dimensional cell growth and angiogenesis, Biomaterials 25(26) (2004) 5735-5742.
[184] Y. Kato, S. Ozawa, C. Miyamoto, Y. Maehata, A. Suzuki, T. Maeda, Y. Baba, Acidic extracellular microenvironment and cancer, Cancer Cell Int. 13 (2013).
[185] G. Khang, S.J. Lee, J.H. Lee, Y.S. Kim, H.B. Lee, Interaction of fibroblast cells on poly(lactide-co-glycolide) surface with wettability chemogradient, Bio-Medical Materials and Engineering 9(3) (1999) 179-187.
[186] E. Ruoslahti, Fibronectin and its receptors, Annual Review of Biochemistry 57 (1988) 375-413.
[187] M. Moreau, S. Yasmin-Karim, S. Kunjachan, N. Sinha, F. Gremse, R. Kumar, K.F. Chow, W. Ngwa, Priming the Abscopal Effect Using Multifunctional Smart Radiotherapy Biomaterials Loaded with Immunoadjuvants, Front. Oncol. 8 (2018).
[188] M. Chavez, M.T. Silvestrini, E.S. Ingham, B.Z. Fite, L.M. Mahakian, S.M. Tam, A. Ilovitsh, A.M. Monjazeb, W.J. Murphy, N.E. Hubbard, R.R. Davis, C.G. Tepper, A.D. Borowsky, K.W. Ferrara, Distinct immune signatures in directly treated and distant tumors result from TLR adjuvants and focal ablation, Theranostics 8(13) (2018) 3611-3628.
[189] S. Hamamoto, T. Okuma, A. Yamamoto, K. Kageyama, T. Takeshita, Y. Sakai, N. Nishida, T. Matsuoka, Y. Miki, Radiofrequency Ablation and Immunostimulant OK-432: Combination Therapy Enhances Systemic Antitumor Immunity for Treatment of VX2 Lung Tumors in Rabbits, Radiology 267(2) (2013) 405-413.
[190] C. Burton, M. Hill, E. Walker, RF Thermoseed - Thermally Self-Regulating Implant for Production of Brain Lesions, IEEE Transactions on Biomedical Engineering BM18(2) (1971) 104-&.
[191] R. Hergt, S. Dutz, M. Röder, Effects of size distribution on hysteresis losses of magnetic nanoparticles for hyperthermia, J. Phys.-Condes. Matter 20(38) (2008).

[192] F. Ishikawa, K. Koyama, K. Watanabe, T. Asano, H. Wada, First-order phase transition at the Curie temperature in MnAs and MnAs0.9Sb0.1, J. Phys. Soc. Jpn. 75(8) (2006).
[193] S. Ando, D. Putnam, D.W. Pack, R. Langer, PLGA microspheres containing plasmid DNA: preservation of supercoiled DNA via cryopreparation and carbohydrate stabilization, Journal of Pharmaceutical Sciences 88(1) (1999) 126-130.
[194] S. Cohen, T. Yoshioka, M. Lucarelli, L.H. Hwang, R. Langer, Controlled Delivery Systems for Proteins Based on Poly(Lactic/Glycolic Acid) Microspheres, Pharmaceutical Research 8(6) (1991) 713-720.
[195] L.S. Ulanova, G. Isapour, A. Maleki, S. Fanaian, K. Zhu, A. Hoenen, C. Xu, Ø. Evensen, G. Griffiths, B. Nyström, Development of methods for encapsulation of viruses into polymeric nano- and microparticles for aquaculture vaccines, Journal of Applied Polymer Science 131(17) (2014) 1-12.
[196] V.S. Kalambur, B. Han, B.E. Hammer, T.W. Shield, J.C. Bischof, In vitro charaterization of movement, heating and visualization of magnetic nanoparticles for biomedical applications, Nanotechnology 16(1221-1233) (2005).
[197] B. Thiesen, A. Jordan, Clinical applications of magnetic nanoparticles for hyperthermia, International Journal of Hyperthermia 24(6) (2008) 467-474.
[198] E.E. Mazon, A.H. Sámano, J. Villarruel, Z. López, P. Knauth, M.E. Cano, Determining the Curie temperature by using the frequency tracker device of a resonant inverter, Meas. Sci. Technol. 29(7) (2018).
[199] X.M. Liu, J. Shaw, J.Z. Jiang, J. Bloemendal, P. Hesse, T. Rolph, X.G. Mao, Analysis on variety and characteristics of maghemite, Sci. China-Earth Sci. 53(8) (2010) 1153-1162.
[200] W. Prellier, V. Smolyaninova, A. Biswas, C. Galley, R.L. Greene, K. Ramesha, J. Gopalakrishnan, Properties of the ferrimagnetic double perovskites A(2)FeReO(6) (A = Ba and Ca), J. Phys.-Condes. Matter 12(6) (2000) 965-973.
[201] A.T. Apostolov, I.N. Apostolova, J.M. Wesselinowa, Ferrimagnetic nanoparticles for self-controlled magnetic hyperthermia, Eur. Phys. J. B 86(11) (2013).
[202] M. Shibuya, Vascular endothelial growth factor (VEGF) and its receptor (VEGFR) signaling in angiogenesis: a crucial target for anti- and pro-angiogenic therapies, Genes & Cancer 2(12) (2011) 1097-1105.
[203] N. Weidner, J.P. Semple, W.R. Welch, J. Folkman, Tumor Angiogenesis and Metastasis - Correlation in Invasive Breast-Carcinoma, New England Journal of Medicine 324(1) (1991) 1-8.
[204] S.S. Dadras, T. Paul, J. Bertoncini, L.F. Brown, A. Muzikansky, D.G. Jackson, U. Ellwanger, C. Garbe, M.C. Mihm, M. Detmar, Tumor lymphangiogenesis - A novel prognostic indicator for cutaneous melanoma metastasis and survival, American Journal of Pathology 162(6) (2003) 1951-1960.
[205] S. Podgrabinska, P. Braun, P. Velasco, B. Kloos, M.S. Pepper, D.G. Jackson, M. Skobe, Molecular characterization of lymphatic endothelial cells, Proceedings of the National Academy of Sciences of the United States of America 99(25) (2002) 16069-16074.
[206] V. Singh, Q.Y. Ji, L. Feigenbaum, R.M. Leighty, A.A. Hurwitz, Melanoma Progression Despite Infiltration by In Vivo-primed TRP-2-specific T Cells, J. Immunother. 32(2) (2009) 129-139.